Dynamics of Cables in Two Examples: Towing of Underslung Loads and Vertically Traveling Beams

A Thesis Presented in Partial Fulfillment
of the Requirements for the Degree

Doctor of Philosophy

by

Abhinav Ravindra Dehadrai
Roll Number 10205061

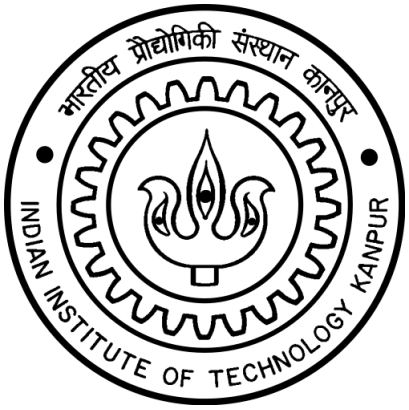

to the

Department of Mechanical Engineering
Indian Institute of Technology Kanpur

August 2018

Certificate

It is certified that the work contained in the thesis titled Dynamics of Cables in Two Examples: Towing of Underslung Loads and Vertically Traveling Beams by Abhinav Ravindra Dehadrai has been carried out under our supervision and that this work has not been submitted elsewhere for a degree.

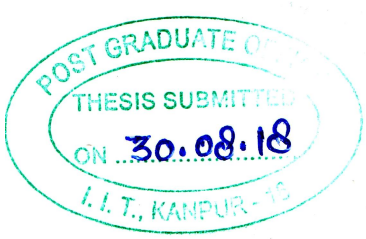

Prof. Ishan Sharma and Prof. Shakti S. Gupta
Mechanics & Applied Mathematics Group
Department of Mechanical Engineering
Indian Institute of Technology Kanpur

30 August 2018

Synopsis

The thesis discusses the dynamics of cables in the following two applications:

(A) The towing of a large, ring-shaped, underslung load attached by a heavy, flexible cable is investigated. For surveying large areas in less time, a large ring-shaped Time Domain Electromagnetic (TDEM) mineral detector is suspended from a helicopter with the help of long cable. For optimal operation the ring-shaped detector should be in the horizontal plane, i.e. normal to gravity. The helicopter's motion and aerodynamic forces affect the motion of the cable and the detector. Further, these forces may misalign the detector or even destabilize it during operating conditions. The dynamics of the cable and detector together as a system is investigated during hovering, forward and maneuvered flight conditions. The cable is modeled as a three-dimensional, geometrically exact (GE) beam, while the ring-shaped detector as a rigid body. Thus, large rotation and deformation of the cable are incorporated. The aerodynamic forces are computed exactly (up to quadrature), using the analytical equation for drag on cylinder in cross-flow from the existing literature, on both the cable and the ring-shaped detector at any instance. Given its much larger mass, the helicopter's motion is assumed to be independent of the cable and the underslung load.

(B) Traveling cables are fundamental driving mechanisms in elevators, conveyor belts, automobile chain-drives, cableways, etc. In these, all or part of the cable is inclined to gravity. During operations the cable tends to oscillate transversely as it travels longitudinally. In this study, the cable is modeled as a linear elastic beam that resists bending moment and shear, and as an inextensible string which supports only tension. The dynamics of horizontally traveling (traveling direction normal to gravity) beams and strings is well studied. We investigate the influence of gravity on the stability of beams and strings which travel vertically, against gravity. It is found that including gravity lowers the critical speed at which a traveling cable becomes unstable. In contrast to the problem A, we restrict attention to small deformations in problem B.

I dedicate this work to my grandparents, parents, teachers and sister

for their endless support and motivation.

Acknowledgements

The work presented in this thesis has reached its present form due to the precious time and energy spent by my thesis advisers and mentors Prof. Ishan Sharma and Prof. Shakti S. Gupta on educating me, along with significant comments and suggestions from Prof. C. Venkatesan, Prof. Anindya Chatterjee, Prof. Abhishek, Prof. Sivasambhu Mahesh, Prof. C. S. Upadhyay, Prof. Pankaj Wahi, Prof. Sovan Lal Das and Prof. Sumit Basu. I also had numerous helpful discussions with my colleagues and friends, namely, Prof. Rakesh Mathpal, Dr. Ravi Dalmeya, Dr. Ashish Bhateja, Dr. Venugopala Swami Punati, Dr. Laxminarsimharao V., Dr. Anshul Faye, Dr. Dhruv Gupta, Dr. Arindam Mahapatra, and [doctors in the making] Vineet Nair, Nidhish Raj, Krishnan Iyer, Deepak Sachan, Prasad Sonar, Shruti Pandey, Dipayan Mukherjee, Nikhil Singh, Shribharath and Vikas Kokonda, along with whom I learned mechanics. I acknowledge all the anonymous reviewers of my works for reading these in great details and suggesting important points to enhance their quality. My stay at IIT Kanpur was made enjoyable and delightful because of several memorable moments spent with my friends Sachendra Singh Baghel, Onkar Mane, Abhayraj Joshi, Mangesh Bawankar, Sreerag Ashok and Sreejith, along with those mentioned above. I would especially recall playing toys and learning Telugu with the cute little 'Ammu', and being invited for delicious home-cooked food by Venu's family, as the happiest times at IIT Kanpur. Apart from them, I received the kindest attention and help from Vivek Shuklaji, Anil Kumar Arya, Rakesh Kanaujia, Shobhit Srivastava, Ram Lakhanji, Satya Prakash Mishra, Brijendra Singh, (Late) Pradeep Kumar, Amit Kumar, and all the staff of Hall-4 during my stay.

Last but not the least, I express my deepest gratitude towards my grandparents, parents, teachers and sister – to whom this work is dedicated, as well as to my sister's family, my dearest uncles, aunts and cousins – who would fill in to share my responsibilities, especially when I couldn't turn up. I could work to the best of my abilities due to their love and encouragement.

Everyone mentioned here, and those I inadvertently forgot to mention, have directly or indirectly contributed to everything the reader finds good about this work, while the shortcomings are purely my own.

Abhinav Ravindra Dehadrai

30 August 2018

Contents

List of Figures

Problem A

Cable Towing Ring-shaped Underslung Load

Notations

The following list describes the notations that will be used in this part of the thesis.

1. Direct notation: all vectors are in lowercase bold letters, e.g. $\boldsymbol{\omega}, \boldsymbol{\kappa}, \boldsymbol{u}, \boldsymbol{x}, \boldsymbol{\varphi}$, etc., while all tensors (second order) are in uppercase bold letters, e.g. $\boldsymbol{R}, \boldsymbol{T}, \boldsymbol{J}, \boldsymbol{\mathcal{J}}, \boldsymbol{\Pi}$, etc.

2. Matrix notation: all column vectors are in lowercase monospaced and sans-serif letters, e.g. $\mathtt{f}, \mathsf{f}, \mathsf{\eta}, \mathsf{\xi}, \mathsf{q}, \mathsf{p}$, etc., while all matrices are in uppercase monospaced and sans-serif letters, e.g. $\mathtt{M}, \mathsf{M}, \mathtt{G}, \mathsf{G}$, etc.

3. Indicial notation: the indices i, j, or k take values $1, 2$ and 3, while Greek indices α or β take values 2 and 3.

4. Other indices/subscripts: e and N correspond to element numbers, while subscripts a and b, respectively, denote the first and second nodes of element e.

5. $\dot{\square} = \dfrac{d\square}{dt}$ Derivative with respect to time t.

6. $\square' = \dfrac{d\square}{ds}$ Derivative with respect to reference arc-length coordinate s or x_1.

7. $\square^*$ Any quantity related to the underslung load, e.g. $\ell^*, \boldsymbol{\omega}^*, \ddot{\boldsymbol{u}}^*, \boldsymbol{M}^*, \mathtt{M}^*, \mathtt{f}^*$, etc.

8. $\square \cdot \square$ Dot Product or Contraction of two vectors, e.g. $\boldsymbol{a} \cdot \boldsymbol{b}$, a tensor and a vector, e.g. $\boldsymbol{T} \cdot \dot{\boldsymbol{\varphi}}$, and of tensors, e.g. $\dot{\boldsymbol{R}} \cdot \boldsymbol{J} \cdot \boldsymbol{R}^{\mathsf{T}}$.

9. $\square \times \square$ Cross Product of two vectors, e.g. $\boldsymbol{a} \times \boldsymbol{b}$.

10. $\square \otimes \square$ Dyadic/Tensor Product of two vectors, e.g. $\boldsymbol{a} \otimes \boldsymbol{b}$, or $\hat{\boldsymbol{e}}_1 \otimes \hat{\boldsymbol{e}}_2$.

11. $|\boldsymbol{\varphi}| = (\boldsymbol{\varphi} \cdot \boldsymbol{\varphi})^{1/2}$ *Euclidean* norm of a vector $\boldsymbol{\varphi}$.

12. $\hat{\boldsymbol{a}} = \dfrac{\boldsymbol{a}}{|\boldsymbol{a}|}$ Unit vector corresponding to a vector $\boldsymbol{a}$.

13. $\widetilde{\boldsymbol{a}} = \mathrm{sk}(\boldsymbol{a})$ Skew-symmetric tensor corresponding to a vector $\boldsymbol{a}$, so that $\widetilde{\boldsymbol{a}} \cdot \boldsymbol{b} = \boldsymbol{a} \times \boldsymbol{b}$, for any vector $\boldsymbol{b}$.

14. $\mathrm{ax}(\widetilde{\boldsymbol{a}}) = \boldsymbol{a}$ Axial vector of skew-symmetric tensor, so that $\widetilde{\boldsymbol{a}} \cdot \boldsymbol{b} = \boldsymbol{a} \times \boldsymbol{b}$, for any vector $\boldsymbol{b}$.

Chapter **1**

Introduction

We investigate the dynamics of a cable that is towing a ring-shaped underslung load beneath a helicopter. Such systems, as shown in Fig. 1.1, find use in large-area mineral surveys. We propose to model the cable as a beam, while including large rotations and large deformations. To this end, we will utilize geometrically exact beam theory (GEBT or GE beam theory). The ring-shaped load will be taken to be a rigid body with appropriate parameters, viz. geometry, mass, and moment of inertia. Aerodynamic drag on the cable will be modeled employing models in available literature, while that on the ring-shaped underslung load will be derived separately.

Figure 1.1: *Photograph of a commercial helicopter towed TDEM (Time Domain Electro-Magnetic) system (courtesy: SkyTEM).*

This part of the thesis covers three major objectives:

1. Finite-element formulation of the three-dimensional multibody dynamics model of the towed underslung load system,

2. Implementations of three-dimensional wind drag on the heavy cable and the rigid ring-shaped underslung load, and

3. Computing the transient response of the cable-underslung load system to different flight conditions and maneuvers of the towing point, while subjected to aerodynamic drag and gravitational forces.

Before describing the multibody system in detail, we take an overview of typical models considered in the existing literature.

1.1 Underslung load systems

Mechanics of cable-underslung load systems have been of major interest ever since the first world war, when McLeod [1918] first studied the deformed equilibrium shapes of heavy towing cables under the influence of wind drag. The underslung load was modeled as a lumped mass subjected to a constant drag force, while the cable was modeled as a planar (2D) inextensible string, which bears only tension, as shown in Fig. 1.2. Thus, the analysis of a cable-underslung load system was essentially the study of the cable alone, wherein the underslung load provided end conditions. This work was further developed by Glauert [1930] by deriving the conditions of stability for massless inextensible strings in the absence of restoring/damping forces. Later Glauert [1934] obtained family of static equilibrium curves of heavy strings towing lumped masses. In Chap. 5, we will compare these curves with those obtained from our cable model (Chap. 2) when subjected to the same aerodynamic loading.

Consideration of inertial and aerodynamic forces of underslung loads gained more attention with Poll & Cromack [1973]'s linear stability analysis of bluff underslung loads, namely a box-shaped and a cylindrical-shaped body (see Fig. 1.3), during steady and straight flight condition. The mass of cable (string) and the rotor's downwash on the underslung load were neglected in the analysis. The cable was attached to the load at a single point, and only longitudinal (in the direction of flight) and lateral (in the direction normal to both the flight and the gravity) oscillations were studied. This work was extended by Feaster et al. [1977] by considering the

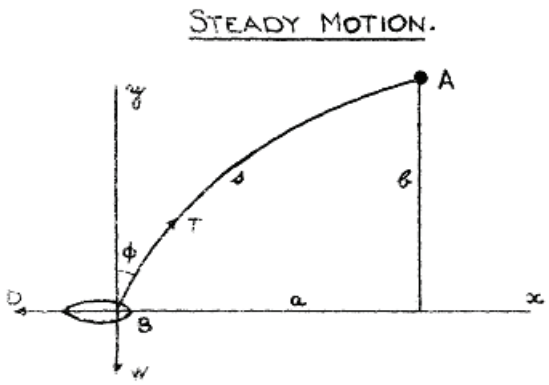

Figure 1.2: *Schematic of Glauert's model of an inextensible string AB towing a lumped mass B of weight W subjected to a constant drag force D. The figure is taken from Glauert [1930]*

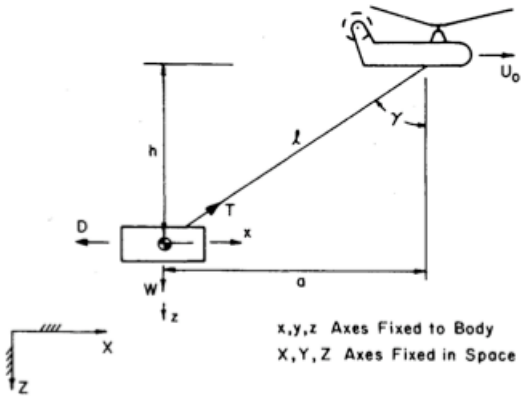

Figure 1.3: *Schematic of Poll and Cromack's helicopter towed box/cylinder-shaped underslung load model. The figure is taken from Poll & Cromack [1973] and Feaster et al. [1977].*

yaw (about the direction of gravity) and pitching moments as well. Motivated by the analogous research on kites, tethered aerostats, aerial refueling hoses, towed sonar equipments, etc., Etkin [1998] generalized the planar heavy cable model by considering aerodynamic forces, inertia, extensibility and internal (viscous) damping. The cable was discretized into finite number of cylinders as shown in Fig. 1.4 and then the lift and drag on each cylinder inclined in the cross-flow was computed following the standard 2D model given in [Hoerner, 1992]. The underslung load was a streamlined cylindrical rigid-body, while the driving vehicle was assumed to be a point moving with a constant speed. They found that attaching tail-fins to the given underslung load marginally stabilized the system during the steady forward flight.

The Newton-Euler equations of motion for helicopters towing various slung loads via massless, rigid or stretchable, links were compiled by Cicolani & Kanning [1992] for the purpose of trajectory control. The links were modeled as constraints to the two-body equations of the helicopter-

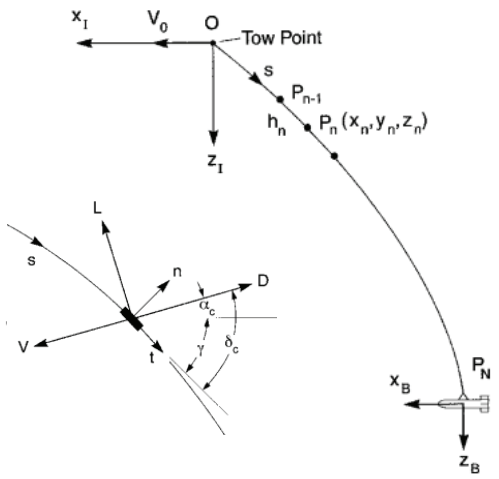

Figure 1.4: *Schematic of Etkin's model of cable towing a streamlined underslung load. The figure is taken from Etkin [1998].*

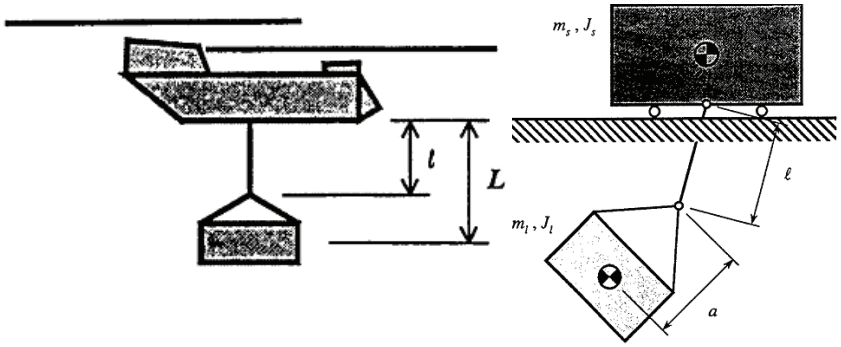

Figure 1.5: *Schematic of Stuckey's model of helicopter towing a box/cylindrical underslung load (left) and pendulum-cart model (right). The figure is taken from Stuckey [2001].*

underslung load system. Additionally, the aerodynamic forces on the links were also neglected. Later, Stuckey [2001] implemented these equations in dynamic simulations of an entire helicopter slung-load system. They compared the modes with those of a simple pendulum suspended under a hovering cart as shown in Fig. 1.5. The link connecting the two bodies was massless and either rigid or stretchable.

Bisgaard et al. [2009] derived the equations of a general two-body helicopter slung-load system shown in Fig. 1.6 subjected to the same constraints as employed by Stuckey [2001], but using the Udwadia & Kalaba [1992]'s approach, which is based on the Gauss's principle of least constraints.

All the works above should be referred to for further references in this field. Thereafter, many works (not cited here for brevity) have followed, more or less, the same models for simulating a large variety of practical problems. For example, many of them have extensively studied different ways of suspending the underslung load to the helicopter, such as multi-point suspension, or different ways one load is suspended simultaneously under multiple helicopters (multi-lift), or

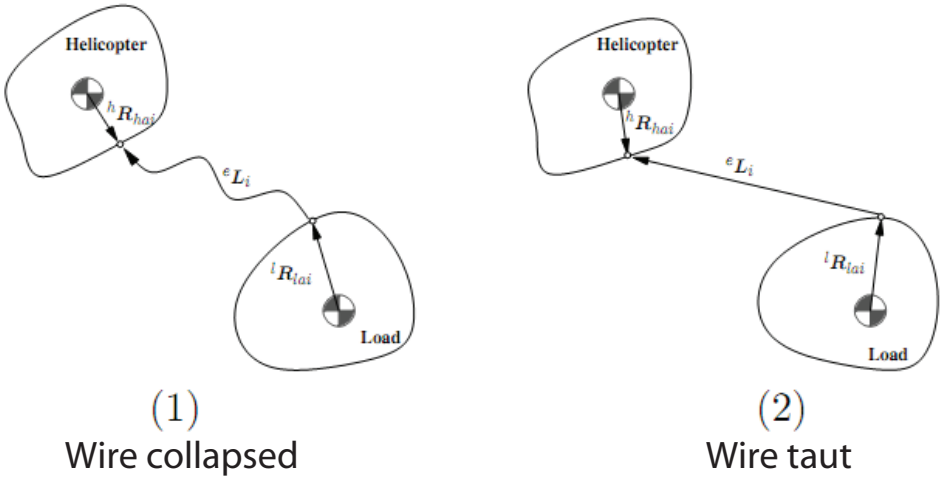

Figure 1.6: *Schematic of Bisgaard's model of a rigid body towing another. The figure is taken from Bisgaard et al. [2009].*

developing trajectory control systems for the helicopter, et cetera. We, however, focus only on the dynamics of underslung loads suspended at a single point via a flexible cable under a helicopter because of our interest in the model for towing of large ring-shaped mineral detectors.

1.2 Towed mineral detectors

Helicopter towed Time-Domain Electromagnetic (TDEM) systems, one such shown in Fig. 1.1, survey large areas rapidly. They are mostly ring- or polygon-shaped instrumented structures which detect the presence of subsurface water or other minerals when oriented parallel to the surface. The size of the instrumented structure is large in comparison to the helicopter under which these are suspended. Due to this the instrumented structure (underslung load) may experience 3D aerodynamic forces, and depending on the magnitude and the net direction of these forces it may undergo complex 3D (spatial) motion. Furthermore, as the flexible cable itself is subjected to 3D aerodynamic forces, the coupled dynamics of the cable and the underslung load may result in large spatial displacements and rotations in both.

Recently, Lahiri et al. [2012] presented a simplified model for this application. To the best of our knowledge, it is still the only available mechanical model despite the existing, but generally inaccessible, commercial TDEM technologies as mentioned in their work. Owing to the complexity of the system to be modeled, the authors analyzed a simple pendulum model suspended by massless link as shown in Fig. 1.7. The objective of their work was to compute the tension in the cable at equilibrium during hover and forward flight.

Developing exact equations of motion for the cable, by considering its resistance to general

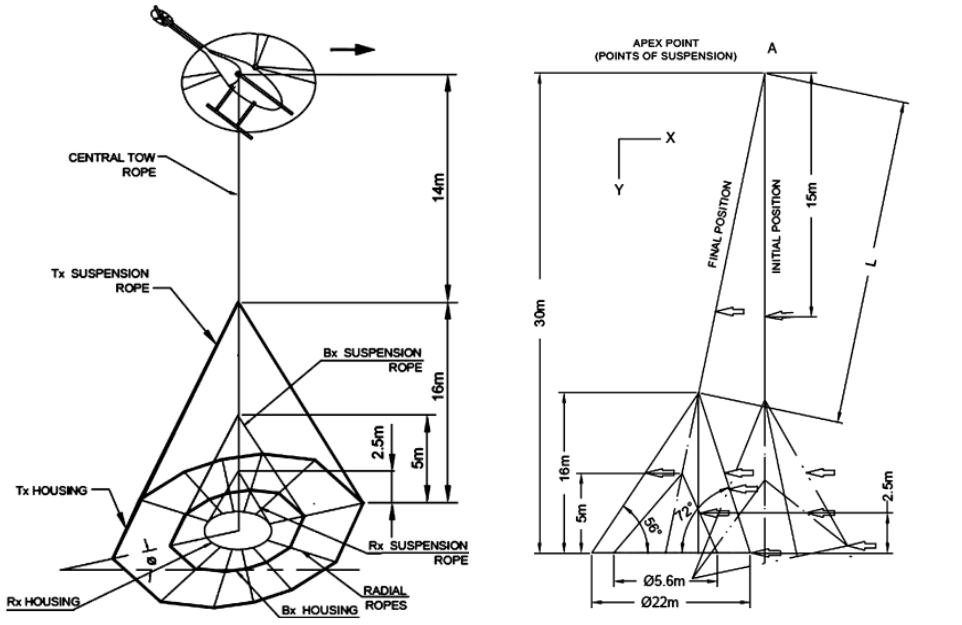

Fig. 1. Schematic diagram of TDEM store.

Fig. 9. Drag forces on different sections of the store and initial tilt in forward flight.

(a) (b)

Figure 1.7: (a) *Schematic of Lahiri's helicopter towed model of TDEM system which is subjected to* (b) *drag during forward flight. These figures are taken from Lahiri et al. [2012].*

bending, twisting and stretching, along with those for the given underslung load, is important for simulating the correct response of the system to complex aerodynamic loads during various flying conditions. Only then, we can determine the proper conditions for stability of the system or the conditions when the instrumented structure will remain oriented within acceptable limits with respect to the ground.

1.3 Present model

To incorporate all the effects mentioned above, this thesis proposes the multibody dynamics model as shown in Fig. 1.8, in which the towing cable is modeled as a geometrically exact (GE) beam while the underslung load is modeled as a rigid body. The cable is hinged (moment-free) to the helicopter, while it is clamped to the massless rods of the underslung load. The torsional stiffness at bottom (clamped) joint is tunable to facilitate calibration of the joint's stiffness to match the actual when experimental data is made available in future. The massless rods of the underslung load are rigidly connected to the ring.

This part of the thesis is structured as follows. The equations for 3D motion of the cable using the GE beam theory [Antman, 2013; Ibrahimbegović, 1995; Simo & Vu-Quoc, 1988] are derived in Chap. 2, followed by the rigid body equations [Greenwood, 1988] of the slung load in Chap. 3.

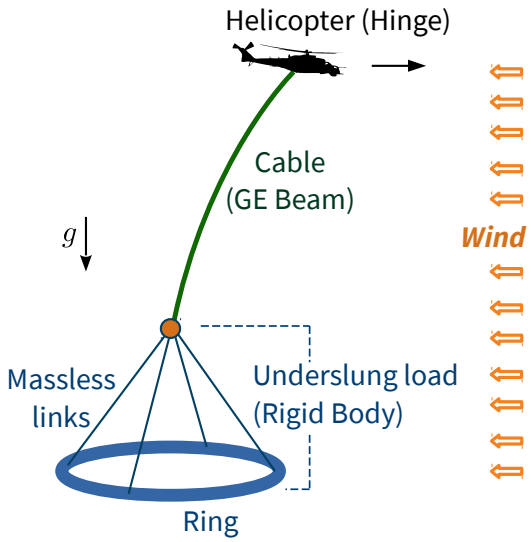

Figure 1.8: *Schematic of the 3D multibody dynamics model of the towed slung load system.*

The helicopter is only a hinge point whose motion is specified.

Aerodynamic forces, including the von Karman effect, on the cable is derived in Sec. 2.6.2 of Chap. 2 based on the available model [Hoerner, 1992; Païdoussis et al., 2010] of a cylinder in cross-flow. Furthermore, in absence of drag models for a ring in medium to high Reynold number flows, we develop a different approach to compute the net aerodynamic forces and moments in Sec. 3.2 of Chap. 3.

The finite element formulation [Bathe, 2006; Ibrahimbegović & Mikdad, 1998] for simulating the dynamics of the coupled cable-slung-load system is discussed in Chap. 4. The results of numerical simulations are presented in Chap. 5, where we begin by validating and comparing GE beam with those given in literature discussed in secs. 1.1 and 1.2. For example, we begin by validating the solutions of the GE beam from various sample problems given by Simo & Vu-Quoc [1986b], then we compare the equilibrium shapes of the GE beam with Glauert [1930]'s towing string that neglects bending stiffness, and later we simulate the response of GE beam towed mineral detector to aerodynamic load during various kinds of maneuvers. Finally, the conclusions are summarized in Chap. 6, along with the scope for future work.

Chapter 2

Mathematical Model of Towing Cable

In this chapter we give a brief introduction to the geometrically exact (GE) beam theory which we have used for modeling the towing cable. The nonlinear elastodynamic equations of GE beam were given by Reissner [1981], and its nonlinear finite element (FE) formulation was developed by several authors, such as Ibrahimbegović [1995]; Simo [1985]; Simo & Vu-Quoc [1986b, 1988] and Betsch & Steinmann [2002], to name a few. More references and discussions can be found in Antman [2013]; Shabana [1997] and Meier et al. [2017]. We begin with the kinematics of the GE beam, followed by the definition of its strain measures, constitutive relation, derivation of the governing equations with its weak form, the aerodynamic force equations, and finally we discuss boundary conditions.

2.1 Geometry and kinematics

The motion of the GE beam (or *beam*, for brevity) is not restricted to any particular plane, and it can be a three-dimensional motion which will be observed in the spatially *fixed* coordinate system $\hat{\boldsymbol{e}}_1$-$\hat{\boldsymbol{e}}_2$-$\hat{\boldsymbol{e}}_3$ centered at O; see Fig. 2.1. In the reference state, the beam of length ℓ is straight, and its centroidal axis is aligned to the $\hat{\boldsymbol{e}}_1$ axis. A material point P_0 in this configuration is defined by the vector $\mathbf{x}$:

$$\mathbf{x} = \mathbf{x}_\mathrm{c} + \mathbf{x}_\mathrm{cp} = s\hat{\boldsymbol{e}}_1 + (\mathrm{x}_2\hat{\boldsymbol{e}}_2 + \mathrm{x}_3\hat{\boldsymbol{e}}_3), \tag{2.1.1}$$

where $s \equiv \mathrm{x}_1$ is the coordinate along the centroidal axis so that $\mathbf{x}_\mathrm{c} = s\hat{\boldsymbol{e}}_1$ locates the center C_0 and $\mathbf{x}_\mathrm{cp} = \mathrm{x}_2\hat{\boldsymbol{e}}_2 + \mathrm{x}_3\hat{\boldsymbol{e}}_3$ finds P_0 relative to C_0 on the cross-section whose plane is defined by the unit vectors $\hat{\boldsymbol{e}}_2$ and $\hat{\boldsymbol{e}}_3$.

An identical coordinate system $\hat{\boldsymbol{e}}_1$-$\hat{\boldsymbol{e}}_2$-$\hat{\boldsymbol{e}}_3$, whose center O' coincides with O at time $t = 0$, remains attached to the beam at time t while the beam is translating on a prescribed trajectory, which is defined by displacement $\boldsymbol{u}_0(t)$, velocity $\dot{\boldsymbol{u}}_0(t)$ and acceleration $\ddot{\boldsymbol{u}}_0(t)$. In the

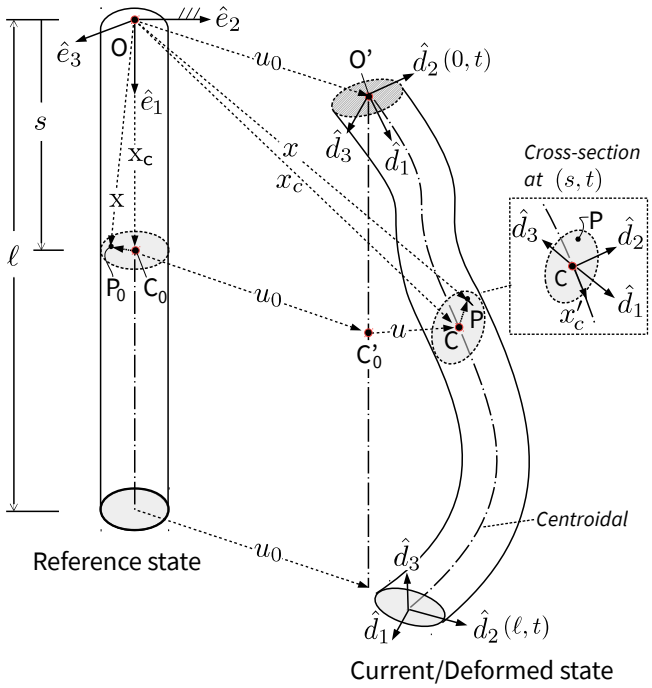

Figure 2.1: *Schematic of the GE beam in reference and current/deformed states is shown.*

current/deformed state at t, the cross-section is defined by the orthonormal basis $\hat{\boldsymbol{d}}_2$-$\hat{\boldsymbol{d}}_3$, called as *directors*, along with the normal $\hat{\boldsymbol{d}}_1 = \hat{\boldsymbol{d}}_2 \times \hat{\boldsymbol{d}}_3$ as shown in Fig. 2.1.

The *special* GE beam theory that we employ assumes that the beam's *cross-sections may only rotate in a rigid manner without deforming*. In other words, a circular cross-section in the reference state remains circular in the current state, as shown in Fig. 2.1, while undergoing a three-dimensional rigid body rotation. Thus, the cross-sectional deformations such as warping or change in shape/size are disregarded, and the transformation/rotation of cross-section is independent of the sectional coordinates x_2 and x_3.

Thus, the coordinate system $\hat{\boldsymbol{d}}_1$-$\hat{\boldsymbol{d}}_2$-$\hat{\boldsymbol{d}}_3$ is attached to the cross-section and rotates with it. The rotation of directors from the reference coordinate system is given by the rotation tensor

$$\boldsymbol{R}(s,t) = \hat{\boldsymbol{d}}_i(s,t) \otimes \hat{\boldsymbol{e}}_i, \tag{2.1.2}$$

where the indices $i = 1, 2$ and 3, while the operator $\otimes$ denotes the tensor/dyadic product. As mentioned above, the rotation tensor $\boldsymbol{R}(s,t)$ is independent of the sectional coordinates x_2 and x_3, while it depends only on the coordinate $s \equiv \mathrm{x}_1$ along the reference centroidal axis and the time t. Therefore, we can now define the directors of cross-section as

$$\hat{\boldsymbol{d}}_i = \boldsymbol{R} \cdot \hat{\boldsymbol{e}}_i. \tag{2.1.3}$$

Note that, the rotation tensor $\boldsymbol{R} = \mathbf{1}$ in the reference configuration (Fig. 2.1) and the directors $\hat{\boldsymbol{d}}_i$ align with the reference coordinate system $\hat{\boldsymbol{e}}_i$.

In the current state shown in Fig. 2.1, the material point P and the center C correspond to points P_0 and C_0, respectively, of the reference state. The position of P is given by

$$\boldsymbol{x} = \boldsymbol{x}_{\mathrm{c}} + \boldsymbol{x}_{\mathrm{cp}}, \tag{2.1.4a}$$

where the position of C on the current centroidal curve

$$\boldsymbol{x}_{\mathrm{c}} = s\hat{\boldsymbol{e}}_1 + \boldsymbol{u}(s,t) + \boldsymbol{u}_0(t), \tag{2.1.4b}$$

where $\boldsymbol{u} + \boldsymbol{u}_0$ is the total displacement of C from C_0 in time t, while $\boldsymbol{x}_{\mathrm{cp}}$ is the position of P with respect to C. Using (2.1.3), $\boldsymbol{x}_{\mathrm{cp}}$ can be obtained as a linear transformation/rotation of the reference position vector $\mathbf{x}_{\mathrm{cp}}$,

$$\boldsymbol{x}_{\mathrm{cp}} = \boldsymbol{R} \cdot \mathbf{x}_{\mathrm{cp}} = \mathrm{x}_2\hat{\boldsymbol{d}}_2(s,t) + \mathrm{x}_3\hat{\boldsymbol{d}}_3(s,t). \tag{2.1.4c}$$

Note that the unit normal $\hat{\boldsymbol{d}}_1$ of the current cross-section may *not* be aligned with the tangent $\boldsymbol{x}_{\mathrm{c}}' = d\boldsymbol{x}_{\mathrm{c}}/ds$, as shown in the inset of Fig. 2.1. The difference in these two vectors defines the stretch in the centroidal line along with the shearing of the plane of the cross-section, and we will discuss this in detail later in Sec. 2.3.

Now, we discuss more about the rotation tensor of a cross-section.

2.1.1 Rotation tensor

The rotation tensor $\boldsymbol{R}(s,t)$ is a three-dimensional orthogonal tensor with unit determinant. It can be parameterized by a set of three independent parameters $\varphi_i(s,t)$,

$$\boldsymbol{R} = \boldsymbol{R}(\boldsymbol{\varphi})\,; \quad \text{we set} \quad \boldsymbol{\varphi} = \varphi_i\hat{\boldsymbol{e}}_i.$$

The choice of parameters φ_i adopted depends upon the application, existence of singularities, computational advantage and physical interpretation of the motion. From Euler's rotation theorem, we know that a general three-dimensional rotation can be expressed in terms of the rotation angle ϑ about the unit vector/direction of rotation $\hat{\boldsymbol{a}}$. Accordingly, the rotation tensor $\boldsymbol{R}$ is represented by Rodrigues' formula:

$$\boldsymbol{R} = \mathbf{1} + \sin\vartheta\,\widetilde{\boldsymbol{a}} + (1 - \cos\vartheta)\,\widetilde{\boldsymbol{a}}^2, \tag{2.1.5}$$

where $\mathbf{1}$ is identity tensor and we denote the skew-symmetric tensor $\widetilde{\boldsymbol{a}} = \mathrm{sk}(\hat{\boldsymbol{a}})$ which is associated to the vector $\hat{\boldsymbol{a}} = a_i\hat{\boldsymbol{e}}_i$. Note that this representation of $\boldsymbol{R}$ has four (not three)

independent parameters, namely ϑ, a_1, a_2 and a_3. However, by defining a vector

$$\boldsymbol{\varphi} = \vartheta\, \hat{\boldsymbol{a}} \quad \text{or} \quad \varphi_i = \vartheta a_i,$$

we can represent (2.1.5) in a modified form or as an *exponential map*, having just three independent parameters,

$$\boldsymbol{R} = \mathbf{1} + \frac{\sin|\boldsymbol{\varphi}|}{|\boldsymbol{\varphi}|}\,\widetilde{\boldsymbol{\varphi}} + \frac{1-\cos|\boldsymbol{\varphi}|}{|\boldsymbol{\varphi}|^2}\,\widetilde{\boldsymbol{\varphi}}^2 = \exp\left(\widetilde{\boldsymbol{\varphi}}\right), \tag{2.1.6}$$

where $\widetilde{\boldsymbol{\varphi}} = \mathrm{sk}\left(\boldsymbol{\varphi}\right)$, and the norm

$$|\boldsymbol{\varphi}| = \left(\varphi_1^2 + \varphi_2^2 + \varphi_3^2\right)^{1/2} = \vartheta.$$

Further discussion on the rotation tensor is available in Appendix 2.b.

Having defined the position and displacement of a material point and the rotation of cross-section, we will now define the total velocity, total acceleration, angular velocity and angular acceleration.

2.1.2 Velocity and acceleration

The velocity of a material point P is obtained by differentiating the position vector (2.1.4a),

$$\dot{\boldsymbol{x}} = \dot{\boldsymbol{x}}_{\mathrm{c}} + \dot{\boldsymbol{x}}_{\mathrm{cp}} = \dot{\boldsymbol{u}}_0(t) + \dot{\boldsymbol{u}}(s,t) + \mathrm{x}_2\dot{\hat{\boldsymbol{d}}}_2(s,t) + \mathrm{x}_3\dot{\hat{\boldsymbol{d}}}_3(s,t), \tag{2.1.7}$$

where we denote $\dot{\square} \equiv d\square/dt$ as the total time derivative, which implies $\dot{\boldsymbol{x}}_{\mathrm{c}} = \dot{\boldsymbol{u}}_0 + \dot{\boldsymbol{u}}$ is the total velocity of the centroid C of the cross-section, while the time-derivative of (2.1.3) is

$$\dot{\hat{\boldsymbol{d}}}_i = \dot{\boldsymbol{R}} \cdot \hat{\boldsymbol{e}}_i = \dot{\boldsymbol{R}} \cdot \boldsymbol{R}^{\mathsf{T}} \cdot \boldsymbol{d}_i \text{ for } i = 1, 2 \text{ and } 3. \tag{2.1.8a}$$

The quantity $\dot{\boldsymbol{R}} \cdot \boldsymbol{R}^{\mathsf{T}}$ is a skew-symmetric[1] tensor, called as the angular velocity of cross-section,

$$\widetilde{\boldsymbol{\omega}} = \dot{\boldsymbol{R}} \cdot \boldsymbol{R}^{\mathsf{T}}. \tag{2.1.8b}$$

The parametric representation of $\widetilde{\boldsymbol{\omega}}$ as a function of $\boldsymbol{\varphi}$ and the extraction of its axial vector $\boldsymbol{\omega} = \mathrm{ax}\left(\dot{\boldsymbol{R}} \cdot \boldsymbol{R}^{\mathsf{T}}\right)$ is appended in Sec. 2.c.

Finally, the total velocity (2.1.7) of point P

$$\dot{\boldsymbol{x}} = \dot{\boldsymbol{u}}_0 + \dot{\boldsymbol{u}} + \widetilde{\boldsymbol{\omega}} \cdot \boldsymbol{x}_{\mathrm{cp}} = \dot{\boldsymbol{u}}_0 + \dot{\boldsymbol{u}} + \boldsymbol{\omega} \times \boldsymbol{x}_{\mathrm{cp}}, \tag{2.1.9}$$

while the acceleration of P is

$$\ddot{\boldsymbol{x}} = \ddot{\boldsymbol{u}}_0 + \ddot{\boldsymbol{u}} + \dot{\widetilde{\boldsymbol{\omega}}} \cdot \boldsymbol{x}_{\mathrm{cp}} + \widetilde{\boldsymbol{\omega}}^2 \cdot \boldsymbol{x}_{\mathrm{cp}} = \ddot{\boldsymbol{u}} + \dot{\boldsymbol{\omega}} \times \boldsymbol{x}_{\mathrm{cp}} + \boldsymbol{\omega} \times (\boldsymbol{\omega} \times \boldsymbol{x}_{\mathrm{cp}}), \tag{2.1.10}$$

[1] *Differentiating the orthogonality equation $\boldsymbol{R} \cdot \boldsymbol{R}^T = \mathbf{1}$, we find that $\dot{\boldsymbol{R}} \cdot \boldsymbol{R}^T = -\boldsymbol{R} \cdot \dot{\boldsymbol{R}}^T$ is skew-symmetric.*

where $\ddot{\boldsymbol{u}}_0 + \ddot{\boldsymbol{u}}$ is the total linear acceleration of the centroid C, and the skew-symmetric tensor $\dot{\tilde{\boldsymbol{\omega}}} = \mathrm{sk}\,(\dot{\boldsymbol{\omega}})$ is the angular acceleration tensor of cross-section.

In the next section, we balance the linear and angular momenta to obtain the governing equations of the beam.

2.2 Differential/strong form of governing equations

The one-dimensional, arc-length based, governing differential equations of GE beam can be derived through reduction from the three-dimensional continuum mechanics theory.

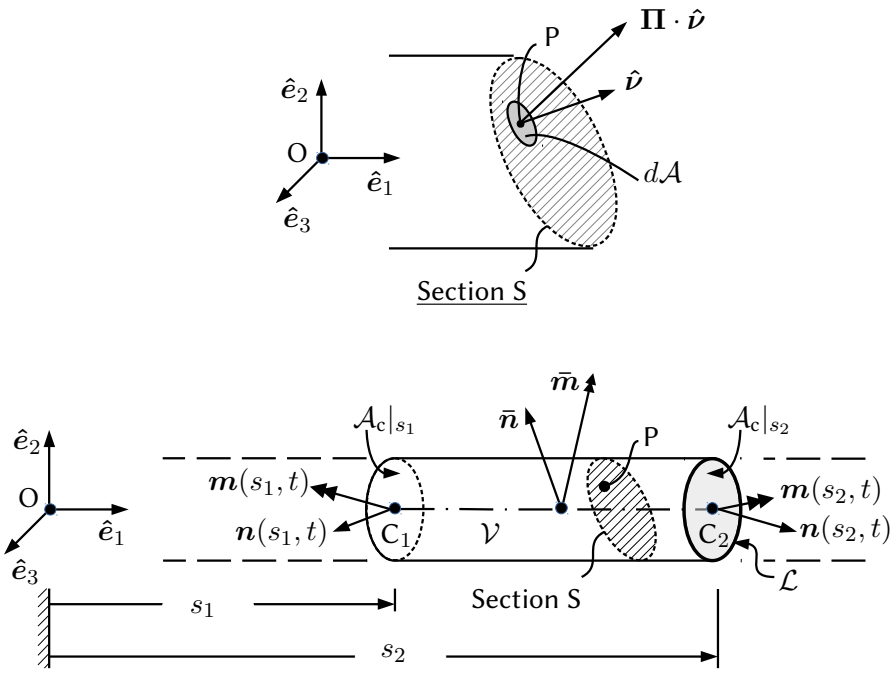

Figure 2.2: *A portion of the beam of length $s_2 - s_1$ occupying a volume $\mathcal{V}$ in its reference configuration is shown. The area of cross-section $\mathcal{A}_\mathrm{c}$ is enclosed by the contour $\mathcal{L}$. An arbitrary section S (hatched) passing through the material point P of the beam is shown. Zoomed-in view of the section S (top) shows the nominal traction $\boldsymbol{\Pi}\cdot\hat{\boldsymbol{\nu}}$ at point P, which is enclosed in a differential area $d\mathcal{A}$ whose unit normal is $\hat{\boldsymbol{\nu}}$. Here, the first Piola-Kirchhoff (nominal) stress tensor $\boldsymbol{\Pi}$ defines the state of stress at P.*

Figure 2.2 shows a part of beam in reference configuration with arc-length $s_2 - s_1$ occupying a volume $\mathcal{V}$. The area of cross-section $\mathcal{A}_\mathrm{c}$ is shown enclosed by the contour $\mathcal{L}$. The total surface area of this part of beam is

$$\mathcal{A} = \mathcal{A}_\mathrm{c}|_{s_1} + \mathcal{A}_\mathrm{c}|_{s_2} + \int_{s_1}^{s_2} \mathcal{L}\, ds.$$

We begin with the governing equations of a three-dimensional elastic continua and then reduce them to a one-dimensional (arc-length) form.

Linear momentum balance: The state of stress at any point P inside volume $\mathcal{V}$ be defined by the first Piola-Kirchhoff stress tensor $\mathbf{\Pi}$. The linear momentum balance across a small differential volume $d\mathcal{V}$ and differential surface area $d\mathcal{A}$, integrated over the entire portion beam, is

$$\iint_{\mathcal{A}} \mathbf{\Pi} \cdot \hat{\boldsymbol{\nu}}\, d\mathcal{A} + \iiint_{\mathcal{V}} \bar{\mathbf{b}}\, d\mathcal{V} = \iiint_{\mathcal{V}} \rho_0 \ddot{\boldsymbol{x}}\, d\mathcal{V}, \tag{2.2.1}$$

where $\bar{\mathbf{b}}$ is body force per unit volume. Using (2.1.4a) and the definition (2.d.1a) of density ρ per unit length, we have

$$\iiint_{\mathcal{V}} \rho_0 \ddot{\boldsymbol{x}}\, d\mathcal{V} = \int_{s_1}^{s_2} \rho \ddot{\boldsymbol{x}}_{\mathrm{c}}\, ds.$$

Also, expanding

$$\iint_{\mathcal{A}} \mathbf{\Pi} \cdot \hat{\boldsymbol{\nu}}\, d\mathcal{A} = \iint_{\mathcal{A}_{\mathrm{c}}} -(\mathbf{\Pi} \cdot \hat{\boldsymbol{e}}_1)|_{s_1}\, d\mathcal{A}_{\mathrm{c}} + \iint_{\mathcal{A}_{\mathrm{c}}} (\mathbf{\Pi} \cdot \hat{\boldsymbol{e}}_1)|_{s_2}\, d\mathcal{A}_{\mathrm{c}} + \int_{s_1}^{s_2} \oint_{\mathcal{L}} \mathbf{\Pi} \cdot (\nu_\alpha \hat{\boldsymbol{e}}_\alpha)\, d\mathcal{L} ds,$$

where $\nu_\alpha \hat{\boldsymbol{e}}_\alpha$ (for $\alpha = 2$ and 3) is the vector field normal to the lateral contour $\mathcal{L}$ of the beam, the closed integral of $\mathbf{\Pi} \cdot (\nu_\alpha \hat{\boldsymbol{e}}_\alpha)$ is the total imposed traction on $\mathcal{L}$, and

$$\iint_{\mathcal{A}_{\mathrm{c}}} -(\mathbf{\Pi} \cdot \hat{\boldsymbol{e}}_1)|_{s_1}\, d\mathcal{A}_{\mathrm{c}} + \iint_{\mathcal{A}_{\mathrm{c}}} (\mathbf{\Pi} \cdot \hat{\boldsymbol{e}}_1)|_{s_2}\, d\mathcal{A}_{\mathrm{c}} = \int_{s_1}^{s_2} \frac{\partial}{\partial s} \iint_{\mathcal{A}_{\mathrm{c}}} \mathbf{\Pi} \cdot \hat{\boldsymbol{e}}_1\, d\mathcal{A}_{\mathrm{c}} ds$$

is the total traction on the cross-sections at $s = s_1$ and s_2.

Further, by defining

$$\bar{\boldsymbol{n}} := \oint_{\mathcal{L}} \mathbf{\Pi} \cdot (\nu_\alpha \hat{\boldsymbol{e}}_\alpha)\, d\mathcal{L} + \iint_{\mathcal{A}_{\mathrm{c}}} \bar{\mathbf{b}}\, d\mathcal{A}_{\mathrm{c}}$$

as the total external load per unit length and

$$\boldsymbol{n}(s,t) := \iint_{\mathcal{A}_{\mathrm{c}}} \mathbf{\Pi} \cdot \hat{\boldsymbol{e}}_1\, d\mathcal{A}_{\mathrm{c}}$$

as the resultant traction per unit length on the cross-section, simplifies (2.2.1) to

$$\int_{s_1}^{s_2} \left(\boldsymbol{n}' + \bar{\boldsymbol{n}} - \rho \ddot{\boldsymbol{x}}_{\mathrm{c}}\right) ds = 0.$$

Because s_1 and s_2 are arbitrary, by the principle of localization

$$\boldsymbol{n}' + \bar{\boldsymbol{n}} - \rho\left(\ddot{\boldsymbol{u}}_0 + \ddot{\boldsymbol{u}}\right) = 0, \tag{2.2.2}$$

where $\ddot{\boldsymbol{x}}_{\mathrm{c}} = \ddot{\boldsymbol{u}}_0 + \ddot{\boldsymbol{u}}$ follows from differentiation of (2.1.4b) with respect to time.

Angular momentum balance about the origin O is given by

$$\iint_{\mathcal{A}} \boldsymbol{x} \times \boldsymbol{\Pi} \cdot \hat{\boldsymbol{\nu}}\, d\mathcal{A} + \iiint_{\mathcal{V}} \boldsymbol{x} \times \bar{\mathbf{b}}\, d\mathcal{V} = \frac{d}{dt} \iiint_{\mathcal{V}} \rho_0 \boldsymbol{x} \times \dot{\boldsymbol{x}}\, d\mathcal{V}. \tag{2.2.3}$$

Using (2.1.4a) and (2.1.9) the right hand term in (2.2.3) becomes

$$\begin{aligned}
\frac{d}{dt} \iiint_{\mathcal{V}} \rho_0 \boldsymbol{x} \times \dot{\boldsymbol{x}}\, d\mathcal{V} &= \frac{d}{dt} \iiint_{\mathcal{V}} \rho_0 (\boldsymbol{x}_{\mathrm{c}} + \boldsymbol{x}_{\mathrm{cp}}) \times (\dot{\boldsymbol{x}}_{\mathrm{c}} + \boldsymbol{\omega} \times \boldsymbol{x}_{\mathrm{cp}})\, d\mathcal{V} \\
&= \frac{d}{dt} \int_{s_1}^{s_2} \boldsymbol{x}_{\mathrm{c}} \times \dot{\boldsymbol{x}}_{\mathrm{c}} \iint_{\mathcal{A}_{\mathrm{c}}} \rho_0\, d\mathcal{A}_{\mathrm{c}} + \boldsymbol{x}_{\mathrm{c}} \times \left(\boldsymbol{\omega} \times \rho_0 \iint_{\mathcal{A}_{\mathrm{c}}} \boldsymbol{x}_{\mathrm{cp}}\, d\mathcal{A}_{\mathrm{c}} \right) + \rho_0 \iint_{\mathcal{A}_{\mathrm{c}}} \boldsymbol{x}_{\mathrm{cp}}\, d\mathcal{A}_{\mathrm{c}} \times \dot{\boldsymbol{x}}_{\mathrm{c}} \\
&\quad + \left(\iint_{\mathcal{A}_{\mathrm{c}}} (\boldsymbol{x}_{\mathrm{cp}} \cdot \boldsymbol{x}_{\mathrm{cp}}) \mathbf{1} - \boldsymbol{x}_{\mathrm{cp}} \otimes \boldsymbol{x}_{\mathrm{cp}}\, \rho_0 d\mathcal{A}_{\mathrm{c}} \right) \cdot \boldsymbol{\omega}\, ds,
\end{aligned}$$

Further, using the definitions of density and mass moment of inertia given in Sec. 2.d, thus, simplifies

$$\begin{aligned}
\frac{d}{dt} \iiint_{\mathcal{V}} \rho_0 \boldsymbol{x} \times \dot{\boldsymbol{x}}\, d\mathcal{V} &= \int_{s_1}^{s_2} \boldsymbol{x}_{\mathrm{c}} \times \rho \ddot{\boldsymbol{x}}_{\mathrm{c}} + \sum_{i=1}^{2} J_i \{ \dot{\hat{\boldsymbol{d}}}_i (\hat{\boldsymbol{d}}_i \cdot \boldsymbol{\omega}) + \hat{\boldsymbol{d}}_\alpha (\dot{\hat{\boldsymbol{d}}}_\alpha \cdot \boldsymbol{\omega}) + \hat{\boldsymbol{d}}_\alpha (\hat{\boldsymbol{d}}_\alpha \cdot \dot{\boldsymbol{\omega}}) \}\, ds \\
&= \int_{s_1}^{s_2} \boldsymbol{x}_{\mathrm{c}} \times \rho \ddot{\boldsymbol{x}}_{\mathrm{c}} + \boldsymbol{\omega} \times \left(\sum_{i=1}^{2} J_\alpha \hat{\boldsymbol{d}}_i \otimes \hat{\boldsymbol{d}}_i \right) \cdot \boldsymbol{\omega} + \left(\sum_{i=1}^{2} J_i \hat{\boldsymbol{d}}_i \otimes \hat{\boldsymbol{d}}_i \right) \cdot \dot{\boldsymbol{\omega}}\, ds. \\
&= \int_{s_1}^{s_2} \boldsymbol{x}_{\mathrm{c}} \times \rho \ddot{\boldsymbol{x}}_{\mathrm{c}} + \boldsymbol{\omega} \times \boldsymbol{h} + \boldsymbol{\mathcal{J}} \cdot \dot{\boldsymbol{\omega}}\, ds = \int_{s_1}^{s_2} \boldsymbol{x}_{\mathrm{c}} \times \rho \ddot{\boldsymbol{x}}_{\mathrm{c}} + \dot{\boldsymbol{h}}\, ds,
\end{aligned}$$

where, for a circular cross-section of radius r, the mass moment of inertia (per unit length of the cable) in the reference and deformed configurations are, respectively,

$$[\boldsymbol{J}] = \begin{bmatrix} J_1 & 0 & 0 \\ 0 & J_2 & 0 \\ 0 & 0 & J_3 \end{bmatrix} = \rho \frac{\pi r^4}{4} \begin{bmatrix} 2 & 0 & 0 \\ 0 & 1 & 0 \\ 0 & 0 & 1 \end{bmatrix}, \quad \text{and} \quad \boldsymbol{\mathcal{J}} = \boldsymbol{R} \cdot \boldsymbol{J} \cdot \boldsymbol{R}^{\mathsf{T}},$$

while the angular momentum of cross-section

$$\boldsymbol{h} := \boldsymbol{\mathcal{J}} \cdot \boldsymbol{\omega}, \tag{2.2.4}$$

and the rate of change of angular momentum of cross-section is defined as

$$\dot{\boldsymbol{h}} := \boldsymbol{\omega} \times \boldsymbol{h} + \boldsymbol{\mathcal{J}} \cdot \dot{\boldsymbol{\omega}}. \tag{2.2.5}$$

Similarly, the left side of (2.2.3) is expanded using (2.1.4a) and (2.2.2) as follows

$$\iint_{\mathcal{A}} \boldsymbol{x} \times \boldsymbol{\Pi} \cdot \hat{\boldsymbol{\nu}}\, d\mathcal{A} + \iiint_{\mathcal{V}} \boldsymbol{x} \times \bar{\mathbf{b}}\, d\mathcal{V}$$

$$
\begin{aligned}
&= \left[\boldsymbol{x}_{\mathrm{c}} \times \iint_{\mathcal{A}_{\mathrm{c}}} \boldsymbol{\Pi} \cdot \hat{\boldsymbol{e}}_1 \, d\mathcal{A}_{\mathrm{c}} \right]_{s_1}^{s_2} + \int_{s_1}^{s_2} \boldsymbol{x}_{\mathrm{c}} \times \oint_{\mathcal{L}} \boldsymbol{\Pi} \cdot (\nu_\alpha \hat{\boldsymbol{e}}_\alpha) \, d\mathcal{L} ds + \int_{s_1}^{s_2} \boldsymbol{x}_{\mathrm{c}} \times \iint_{\mathcal{A}_{\mathrm{c}}} \bar{\mathbf{b}} \, d\mathcal{A}_{\mathrm{c}} ds \\
&\quad + \left[\iint_{\mathcal{A}_{\mathrm{c}}} (\boldsymbol{x}_{\mathrm{cp}} \times \boldsymbol{\Pi} \cdot \hat{\boldsymbol{e}}_1) \, d\mathcal{A}_{\mathrm{c}} \right]_{s_1}^{s_2} + \int_{s_1}^{s_2} \oint_{\mathcal{L}} \boldsymbol{x}_{\mathrm{cp}} \times \boldsymbol{\Pi} \cdot (\nu_\alpha \hat{\boldsymbol{e}}_\alpha) \, d\mathcal{L} ds + \iiint_{\mathcal{V}} \boldsymbol{x}_{\mathrm{cp}} \times \bar{\mathbf{b}} \, d\mathcal{V} \\
&= \int_{s_1}^{s_2} \frac{d}{ds} (\boldsymbol{x}_{\mathrm{c}} \times \boldsymbol{n}) ds + \int_{s_1}^{s_2} \boldsymbol{x}_{\mathrm{c}} \times \bar{\boldsymbol{n}} \, ds \\
&\quad + \int_{s_1}^{s_2} \left(\frac{d}{ds} \iint_{\mathcal{A}_{\mathrm{c}}} (\boldsymbol{x}_{\mathrm{cp}} \times \boldsymbol{\Pi} \cdot \hat{\boldsymbol{e}}_1) \, d\mathcal{A}_{\mathrm{c}} + \oint_{\mathcal{L}} \boldsymbol{x}_{\mathrm{cp}} \times \boldsymbol{\Pi} \cdot (\nu_\alpha \hat{\boldsymbol{e}}_\alpha) \, d\mathcal{L} + \iint_{\mathcal{A}_{\mathrm{c}}} \boldsymbol{x}_{\mathrm{cp}} \times \bar{\mathbf{b}} \, d\mathcal{A}_{\mathrm{c}} \right) ds \\
&= \int_{s_1}^{s_2} \boldsymbol{x}_{\mathrm{c}}' \times \boldsymbol{n} \, ds + \int_{s_1}^{s_2} \boldsymbol{x}_{\mathrm{c}} \times (\boldsymbol{n}' + \bar{\boldsymbol{n}}) \, ds \\
&\quad + \int_{s_1}^{s_2} \left(\frac{d}{ds} \iint_{\mathcal{A}_{\mathrm{c}}} (\boldsymbol{x}_{\mathrm{cp}} \times \boldsymbol{\Pi} \cdot \hat{\boldsymbol{e}}_1) \, d\mathcal{A}_{\mathrm{c}} + \oint_{\mathcal{L}} \boldsymbol{x}_{\mathrm{cp}} \times \boldsymbol{\Pi} \cdot (\nu_\alpha \hat{\boldsymbol{e}}_\alpha) \, d\mathcal{L} + \iint_{\mathcal{A}_{\mathrm{c}}} \boldsymbol{x}_{\mathrm{cp}} \times \bar{\mathbf{b}} \, d\mathcal{A}_{\mathrm{c}} \right) ds.
\end{aligned}
$$

Further, by introducing

$$
\bar{\boldsymbol{m}} := \oint_{\mathcal{L}} \boldsymbol{x}_{\mathrm{cp}} \times \boldsymbol{\Pi} \cdot (\nu_\alpha \hat{\boldsymbol{e}}_\alpha) \, d\mathcal{L} + \iint_{\mathcal{A}_{\mathrm{c}}} \boldsymbol{x}_{\mathrm{cp}} \times \bar{\mathbf{b}} \, d\mathcal{A}_{\mathrm{c}}
$$

as the external/applied moment and

$$
\boldsymbol{m}(s,t) := \iint_{\mathcal{A}_{\mathrm{c}}} \boldsymbol{x}_{\mathrm{cp}} \times \boldsymbol{\Pi} \cdot \hat{\boldsymbol{e}}_1 \, d\mathcal{A}_{\mathrm{c}}
$$

as the internal/reaction moment, and following the localization argument, we obtain

$$
\boldsymbol{m}' + \boldsymbol{x}_{\mathrm{c}}' \times \boldsymbol{n} + \bar{\boldsymbol{m}} = \dot{\boldsymbol{h}}. \tag{2.2.6}
$$

Finally, the linear momentum balance equation (2.2.2) and the angular momentum balance about the origin (2.2.6) are rewritten in the following simple form:

$$
\boldsymbol{n}' + \bar{\boldsymbol{n}} = \rho \, (\ddot{\boldsymbol{u}}_0 + \ddot{\boldsymbol{u}}) \tag{2.2.7a}
$$

and

$$
\boldsymbol{m}' + \widetilde{\boldsymbol{x}}_{\mathrm{c}}' \cdot \boldsymbol{n} + \bar{\boldsymbol{m}} = \boldsymbol{\mathcal{J}} \cdot \dot{\boldsymbol{\omega}} + \widetilde{\boldsymbol{\omega}} \cdot \boldsymbol{\mathcal{J}} \cdot \boldsymbol{\omega}, \tag{2.2.7b}
$$

where $\widetilde{\boldsymbol{x}}_{\mathrm{c}}' = \mathrm{sk}(\boldsymbol{x}_{\mathrm{c}}')$.

Next, we define the strain measures, followed by the constitutive equation relating strain measures to internal force and moment.

2.3 Strain measures

The gradient of deformation of the GE beam shown in Fig. 2.1 is defined as

$$\mathbf{F} := \boldsymbol{\nabla} \boldsymbol{x} = \frac{\partial \boldsymbol{x}}{\partial \mathbf{x}} = \frac{\partial \boldsymbol{x}}{\partial \mathrm{x}_i} \otimes \hat{\boldsymbol{e}}_i, \tag{2.3.1}$$

where $\mathbf{x}$ is the reference position vector and $\boldsymbol{x}$ is the current position. Using (2.1.1), (2.1.4a) and (2.1.2), we simplify (2.3.1) as follows:

$$\begin{aligned}
\mathbf{F} &= \left\{ \boldsymbol{x}_\mathrm{c}(s,t) + \mathrm{x}_\alpha \hat{\boldsymbol{d}}_\alpha(s,t) \right\}' \otimes \hat{\boldsymbol{e}}_1 + \frac{\partial}{\partial \mathrm{x}_\beta} \left\{ \boldsymbol{x}_\mathrm{c}(s,t) + \mathrm{x}_\alpha \hat{\boldsymbol{d}}_\alpha(s,t) \right\} \otimes \hat{\boldsymbol{e}}_\beta \\
&= \left\{ \boldsymbol{x}'_\mathrm{c}(s,t) + \mathrm{x}_\alpha \hat{\boldsymbol{d}}'_\alpha(s,t) \right\} \otimes \hat{\boldsymbol{e}}_1 + \left\{ \mathbf{0} + \delta_{\alpha\beta} \hat{\boldsymbol{d}}_\alpha(s,t) \right\} \otimes \hat{\boldsymbol{e}}_\beta \\
&= (\boldsymbol{x}'_\mathrm{c} + \mathrm{x}_\alpha \hat{\boldsymbol{d}}'_\alpha) \otimes \hat{\boldsymbol{e}}_1 + (\hat{\boldsymbol{d}}_2 \otimes \hat{\boldsymbol{e}}_2 + \hat{\boldsymbol{d}}_3 \otimes \hat{\boldsymbol{e}}_3),
\end{aligned} \tag{2.3.2}$$

where the greek indices $\alpha, \beta = 2, 3$, and we denote $\square' \equiv \partial\square/\partial \mathrm{x}_1 \equiv \partial\square/\partial s$, while the *kronecker delta* δ_{ij}=1 when i=j otherwise δ_{ij}=0. The derivative of $\hat{\boldsymbol{d}}_i(s,t)$ with respect to $s \equiv \mathrm{x}_1$ is analogous to its time derivative (2.1.8),

$$\hat{\boldsymbol{d}}'_i = \boldsymbol{R}' \cdot \boldsymbol{R}^\mathsf{T} \cdot \hat{\boldsymbol{d}}_i = \widetilde{\boldsymbol{\kappa}} \cdot \hat{\boldsymbol{d}}_i, \tag{2.3.3}$$

where the skew-symmetric tensor,

$$\widetilde{\boldsymbol{\kappa}} = \boldsymbol{R}' \cdot \boldsymbol{R}^\mathsf{T} \tag{2.3.4}$$

is called as the *curvature tensor*. It governs the spatial rate of change of the cross-section, in contrast to the angular velocity $\widetilde{\boldsymbol{\omega}}$ which governs its temporal rate. The equation of corresponding axial vector $\boldsymbol{\kappa} = \mathrm{ax}\left(\boldsymbol{R}' \cdot \boldsymbol{R}^\mathsf{T}\right)$ is obtained similar to $\boldsymbol{\omega}$ described in Sec. 2.b.

Using (2.3.4), (2.1.2) and (2.1.4c) in (2.3.2), we get

$$\begin{aligned}
\mathbf{F} &= (\boldsymbol{x}'_\mathrm{c} + \widetilde{\boldsymbol{\kappa}} \cdot \boldsymbol{x}_\mathrm{cp}) \otimes \hat{\boldsymbol{e}}_1 + (\hat{\boldsymbol{d}}_i \otimes \hat{\boldsymbol{e}}_i - \hat{\boldsymbol{d}}_1 \otimes \hat{\boldsymbol{e}}_1), \\
&= (\boldsymbol{\gamma} + \widetilde{\boldsymbol{\kappa}} \cdot \boldsymbol{x}_\mathrm{cp}) \otimes \hat{\boldsymbol{e}}_1 + \boldsymbol{R},
\end{aligned} \tag{2.3.5}$$

where we define the spatial strain vector

$$\boldsymbol{\gamma} := \boldsymbol{x}'_\mathrm{c} - \hat{\boldsymbol{d}}_1 = \gamma_i \hat{\boldsymbol{d}}_i \tag{2.3.6}$$

as the difference between the tangent $\boldsymbol{x}'_\mathrm{c}$ to the centroidal line at C and the normal $\hat{\boldsymbol{d}}_1$ to the cross-section centered at C. In contrast to the classical beam theories, the tangent to the centroidal line and the normal to the cross-section are *not* necessarily the same, which implies that (2.3.6) is generally *nonzero*. The component γ_1 defines the stretch of the elastic line, while γ_2 and γ_3 define the shearing of the plane of the cross-section.

The component κ_1 of the spatial curvature vector $\boldsymbol{\kappa}$ is the twist or torsion, while κ_2 and κ_3 are the bending of the cross-section.

Together $\boldsymbol{\gamma}$ and $\boldsymbol{\kappa}$ are the spatial strain measures of the GE beam. The corresponding material strain measures are obtained by a pull-back operation,

$$\boldsymbol{\kappa} = \boldsymbol{R}^{\mathsf{T}} \cdot \boldsymbol{\kappa} = \kappa_i \hat{\boldsymbol{e}}_i \;\text{ and }\; \boldsymbol{\gamma} = \boldsymbol{R}^{\mathsf{T}} \cdot \boldsymbol{\gamma} = \gamma_i \hat{\boldsymbol{e}}_i. \tag{2.3.7}$$

The Green-Lagrange strain tensor

The *Polar decomposition* of deformation gradient (2.3.2) yields

$$\mathbf{F} = \boldsymbol{R} \cdot \left(\boldsymbol{R}^{\mathsf{T}} \cdot \boldsymbol{\varepsilon} \otimes \hat{\boldsymbol{e}}_1 + \mathbf{1} \right), \tag{2.3.8}$$

where for brevity we denote the spatial strains by

$$\boldsymbol{\varepsilon} = \boldsymbol{\gamma} + \widetilde{\boldsymbol{\kappa}} \cdot \boldsymbol{x}_{\mathrm{cp}}.$$

The deformation gradient (2.3.8) is decomposed as finite rigid rotation $\boldsymbol{R}$ of the cross-section followed by the *right* stretch tensor $\boldsymbol{R}^{\mathsf{T}} \cdot \boldsymbol{\varepsilon} \otimes \hat{\boldsymbol{e}}_1 + \mathbf{1}$, where the components of the material strains are

$$\varepsilon_i = \hat{\boldsymbol{e}}_i \cdot \boldsymbol{R}^{\mathsf{T}} \cdot \boldsymbol{\varepsilon} = \gamma_i + (\epsilon_{ij2}\, \kappa_j \mathrm{x}_2 + \epsilon_{ij3}\, \kappa_j \mathrm{x}_3), \tag{2.3.9}$$

with the Levi-Civita symbol $\epsilon_{ijk} = 1$ for all positive permutations of the indices $\{i, j, k\}$, $\epsilon_{ijk} = -1$ for the negative permutations and $\epsilon_{ijk} = 0$ for the remaining permutations.

The Green-Lagrange strain tensor

$$\begin{aligned} 2\mathbf{E} &= \mathbf{F}^{\mathsf{T}} \cdot \mathbf{F} - \mathbf{1} \\ &= \boldsymbol{R}^{\mathsf{T}} \cdot \boldsymbol{\varepsilon} \otimes \hat{\boldsymbol{e}}_1 + \hat{\boldsymbol{e}}_1 \otimes \boldsymbol{\varepsilon} \cdot \boldsymbol{R} + (\boldsymbol{\varepsilon} \cdot \boldsymbol{\varepsilon}) \hat{\boldsymbol{e}}_1 \otimes \hat{\boldsymbol{e}}_1 \\ &= \varepsilon_k \hat{\boldsymbol{e}}_k \otimes \hat{\boldsymbol{e}}_1 + \hat{\boldsymbol{e}}_1 \otimes \varepsilon_k \hat{\boldsymbol{e}}_k + (\varepsilon_k \varepsilon_k) \hat{\boldsymbol{e}}_1 \otimes \hat{\boldsymbol{e}}_1. \end{aligned} \tag{2.3.10}$$

In components,

$$2E_{ij} = \hat{\boldsymbol{e}}_i \cdot \mathbf{E} \cdot \hat{\boldsymbol{e}}_j = \varepsilon_i \delta_{1j} + \varepsilon_j \delta_{1i} + (\varepsilon_1^2 + \varepsilon_2^2 + \varepsilon_3^2) \delta_{1i} \delta_{1j}. \tag{2.3.11}$$

where ε_1, ε_2 and ε_3 are given by (2.3.9), so that in matrix form,

$$\mathrm{E} = [\mathbf{E}] = \frac{1}{2} \begin{bmatrix} 2\varepsilon_1 + \varepsilon_1^2 + \varepsilon_2^2 + \varepsilon_3^2 & \varepsilon_2 & \varepsilon_3 \\ \varepsilon_2 & 0 & 0 \\ \varepsilon_3 & 0 & 0 \end{bmatrix}. \tag{2.3.12}$$

Using (2.3.9), we can separate E_{11} into five parts:

$$\begin{aligned} E_{11} &= \gamma_1 + \frac{1}{2}\gamma_1^2 + (\kappa_2 \mathrm{x}_3 - \kappa_3 \mathrm{x}_2) + \frac{1}{2}(\kappa_2 \mathrm{x}_3 - \kappa_3 \mathrm{x}_2)^2 + \frac{1}{2}\left(\gamma_2^2 + \gamma_3^2\right) \\ &\quad + \frac{1}{2}\kappa_1^2\left(\mathrm{x}_2^2 + \mathrm{x}_3^2\right) + (\gamma_1\kappa_2\mathrm{x}_3 - \gamma_1\kappa_3\mathrm{x}_2 - \gamma_2\kappa_1\mathrm{x}_3 + \gamma_3\kappa_1\mathrm{x}_2) \\ &=: E_{11}^{\text{extn}} + E_{11}^{\text{bend}} + E_{11}^{\text{shear}} + E_{11}^{\text{tor}} + E_{11}^{\text{coup}}, \end{aligned}$$

where

$$E_{11}^{\text{extn}} = \gamma_1 + \frac{1}{2}\gamma_1^2 \tag{2.3.13a}$$

is due to linear and nonlinear stretching/extensional components,

$$E_{11}^{\text{bend}} = (\kappa_2 \mathrm{x}_3 - \kappa_3 \mathrm{x}_2) + \frac{1}{2}(\kappa_2 \mathrm{x}_3 - \kappa_3 \mathrm{x}_2)^2 \tag{2.3.13b}$$

is from linear and nonlinear bending strain components,

$$E_{11}^{\text{shear}} = \frac{1}{2}\left(\gamma_2^2 + \gamma_3^2\right) \tag{2.3.13c}$$

has nonlinear shear strain components,

$$E_{11}^{\text{tor}} = \frac{1}{2}\left(\mathrm{x}_2^2 + \mathrm{x}_3^2\right)\kappa_1^2 \tag{2.3.13d}$$

has a nonlinear torsional strain component, and finally,

$$E_{11}^{\text{coup}} = \gamma_1\kappa_2\mathrm{x}_3 - \gamma_1\kappa_3\mathrm{x}_2 - \gamma_2\kappa_1\mathrm{x}_3 + \gamma_3\kappa_1\mathrm{x}_2 \tag{2.3.13e}$$

is a nonlinear quantity having coupled torsion, bending, shear and extensional strain terms.

We highlight following important points:

(1) $E_{12} = E_{21}$ measures both the torsion κ_1 and the shear γ_2. Similarly, $E_{13} = E_{31}$ measures both κ_1 and γ_3;

(2) The stretch measured by $\mathbf{E}$ in (2.3.13a) has an extra nonlinear $\gamma_1^2/2$ term over the preferred measure which is just γ_1;

(3) Both the bending measures κ_2 and κ_3 appear together in the Green-Lagrange strain component (2.3.13b);

(4) $\mathbf{E}$ has a separate nonlinearly coupled contribution (2.3.13e) of extension, shear, bending and torsion over the prescribed strain measures.

The above analysis suggests that the Green-Lagrange strain tensor $\mathbf{E}$, although a general choice to measure finite deformation in a three dimensional elastic continuum, results in nonlinear and coupled expressions of the individual strains: extension, shears, bending and torsion. At the

same time the prescribed strain measures $\boldsymbol{\kappa}$ and $\boldsymbol{\gamma}$ are linear and uncoupled in these strains, which makes them a preferred choice in this reduced one dimensional formulation.

We will now define the constitutive relationship between the strain measures (2.3.6) and (2.3.4) with the internal force $\boldsymbol{n}$ and moment $\boldsymbol{m}$ introduced in the previous section.

2.4 Constitutive relations

A hyperelastic material model [Ibrahimbegović, 1995; Simo, 1985; Simo & Vu-Quoc, 1986b, 1988] is used, for which the strain energy density is

$$\mathrm{w_s}(\boldsymbol{\gamma}, \boldsymbol{\kappa}) = \frac{1}{2}(\boldsymbol{\gamma} \cdot \boldsymbol{\mathcal{C}_n} \cdot \boldsymbol{\gamma} + \boldsymbol{\kappa} \cdot \boldsymbol{\mathcal{C}_m} \cdot \boldsymbol{\kappa}), \tag{2.4.1}$$

where $\boldsymbol{\mathcal{C}_n}$ and $\boldsymbol{\mathcal{C}_m}$ are the second-order spatial elasticity tensors. The tensors $\boldsymbol{\mathcal{C}_n}$ and $\boldsymbol{\mathcal{C}_m}$ are related to the material elasticity tensors $\boldsymbol{C_n}$ and $\boldsymbol{C_m}$ through

$$\boldsymbol{\mathcal{C}_n} = \boldsymbol{R} \cdot \boldsymbol{C_n} \cdot \boldsymbol{R}^{\mathsf{T}} \text{ and } \boldsymbol{\mathcal{C}_m} = \boldsymbol{R} \cdot \boldsymbol{C_m} \cdot \boldsymbol{R}^{\mathsf{T}}. \tag{2.4.2}$$

In the reference configuration,

$$[\boldsymbol{C_n}] = \mathrm{diag}(EA, k_2GA, k_3GA) \text{ and } [\boldsymbol{C_m}] = \mathrm{diag}(GI_1, EI_2, EI_3), \tag{2.4.3}$$

where E is the Young's modulus, G is the shear modulus, A is the cross-sectional area, k_2 and k_3 are the Timoshenko's shear correction factors, which have the values $9/10$ for circular and $5/6$ for a rectangular cross-section [Budynas et al., 2011, pg. 190], and I_1, I_2 and I_3 are the cross-sectional area moment of inertias relative to each of the principal axes. The term EA is called as axial stiffness, k_2GA and k_3GA are the shear stiffnesses, GI_1 is the torsional rigidity along the $\hat{\boldsymbol{e}}_1$ axis, and EI_2 and EI_3 are bending rigidity about the $\hat{\boldsymbol{e}}_2$ and the $\hat{\boldsymbol{e}}_3$ axis, respectively.

The resulting constitutive relationships between the internal force $\boldsymbol{n}$ and moment $\boldsymbol{m}$ and the strain measures $\boldsymbol{\gamma}$ and $\boldsymbol{\kappa}$, respectively, are obtained as

$$\boldsymbol{n} = \frac{\partial \mathrm{w_s}}{\partial \boldsymbol{\gamma}} = \boldsymbol{\mathcal{C}_n} \cdot \boldsymbol{\gamma} \text{ and } \boldsymbol{m} = \frac{\partial \mathrm{w_s}}{\partial \boldsymbol{\kappa}} = \boldsymbol{\mathcal{C}_m} \cdot \boldsymbol{\kappa}. \tag{2.4.4}$$

2.5 Integral/weak form of governing equations

The governing equation in strong (differential/local) form were derived in (2.2.7a) and (2.2.7b). Their weak (integral) forms are obtained in this section. Let $\boldsymbol{\mu}(s)$ and $\boldsymbol{\phi}(s)$ be admissible functions corresponding to the linear and angular momenta, respectively. The weak form is then obtained

as

$$\begin{aligned}\mathrm{w} &= \int_0^\ell \left\{ \boldsymbol{\mu} \cdot (\rho \ddot{\boldsymbol{u}}_0 + \rho \ddot{\boldsymbol{u}} - \boldsymbol{n}' - \bar{\boldsymbol{n}}) + \boldsymbol{\phi} \cdot (\boldsymbol{\mathcal{J}} \cdot \dot{\boldsymbol{\omega}} + \widetilde{\boldsymbol{\omega}} \cdot \boldsymbol{\mathcal{J}} \cdot \boldsymbol{\omega} - \boldsymbol{m}' - \widetilde{\boldsymbol{x}}_{\mathrm{c}}' \cdot \boldsymbol{n} - \bar{\boldsymbol{m}}) \right\} ds = 0 \\ &= \int_0^\ell \left\{ \boldsymbol{\mu} \cdot (\rho \ddot{\boldsymbol{u}}_0 + \rho \ddot{\boldsymbol{u}} - \bar{\boldsymbol{n}}) + \boldsymbol{\mu}' \cdot \boldsymbol{n} + \boldsymbol{\phi} \cdot (\boldsymbol{\mathcal{J}} \cdot \dot{\boldsymbol{\omega}} + \widetilde{\boldsymbol{\omega}} \cdot \boldsymbol{\mathcal{J}} \cdot \boldsymbol{\omega} - \widetilde{\boldsymbol{x}}_{\mathrm{c}}' \cdot \boldsymbol{n} - \bar{\boldsymbol{m}}) + \boldsymbol{\phi}' \cdot \boldsymbol{m} \right\} ds \\ &\quad - \left| \boldsymbol{\mu} \cdot \boldsymbol{n} + \boldsymbol{\phi} \cdot \boldsymbol{m} \right|_0^\ell = 0,\end{aligned}$$

where we have used integration by parts on $\boldsymbol{\mu} \cdot \boldsymbol{n}'$ and $\boldsymbol{\phi} \cdot \boldsymbol{m}'$. The above weak form can be split into the inertial, external, internal and the boundary conditions:

$$\mathrm{w} = \mathrm{w}_{\mathsf{iner}} + \mathrm{w}_{\mathsf{int}} - \mathrm{w}_{\mathsf{ext}} - \mathrm{w}_{\mathsf{bc}} = 0 \tag{2.5.1a}$$

which are defined as, respectively,

$$\mathrm{w}_{\mathsf{iner}} := \int_0^\ell \left\{ \boldsymbol{\mu} \cdot \rho \left(\ddot{\boldsymbol{u}}_0 + \ddot{\boldsymbol{u}} \right) + \boldsymbol{\phi} \cdot \left(\boldsymbol{\mathcal{J}} \cdot \dot{\boldsymbol{\omega}} + \widetilde{\boldsymbol{\omega}} \cdot \boldsymbol{\mathcal{J}} \cdot \boldsymbol{\omega} \right) \right\} ds, \tag{2.5.1b}$$

$$\mathrm{w}_{\mathsf{ext}} := \int_0^\ell \left\{ \boldsymbol{\mu} \cdot \bar{\boldsymbol{n}} + \boldsymbol{\phi} \cdot \bar{\boldsymbol{m}} \right\} ds, \tag{2.5.1c}$$

$$\mathrm{w}_{\mathsf{int}} := \int_0^\ell \left\{ \boldsymbol{\mu}' \cdot \boldsymbol{n} + \boldsymbol{\phi}' \cdot \boldsymbol{m} - \boldsymbol{\phi} \cdot \widetilde{\boldsymbol{x}}_{\mathrm{c}}' \cdot \boldsymbol{n} \right\} ds, \tag{2.5.1d}$$

and

$$\mathrm{w}_{\mathsf{bc}} = \left| \boldsymbol{\mu} \cdot \boldsymbol{n} + \boldsymbol{\phi} \cdot \boldsymbol{m} \right|_0^\ell. \tag{2.5.1e}$$

In matrix notation,

$$\mathrm{w}_{\mathsf{iner}} = \int_0^\ell \eta^{\mathsf{T}} \mathtt{f}_{\mathsf{iner}} \, ds, \; \mathrm{w}_{\mathsf{ext}} = \int_0^\ell \eta^{\mathsf{T}} \mathtt{f}_{\mathsf{ext}} \, ds, \; \mathrm{w}_{\mathsf{int}} = \int_0^\ell \left(\eta'^{\mathsf{T}} \mathtt{f}_{\mathsf{int}}^{\mathsf{I}} + \eta^{\mathsf{T}} \mathtt{f}_{\mathsf{int}}^{\mathsf{II}} \right) ds \;\text{ and }\; \mathrm{w}_{\mathsf{bc}} = \left| \eta^{\mathsf{T}} \mathtt{f} \right|_0^\ell, \tag{2.5.1f}$$

where we have introduced the 6×1 column vector $\eta^{\mathsf{T}}(s) := [\boldsymbol{\mu} \quad \boldsymbol{\phi}]$ of the admissible functions, with derivative η', while

$$\mathtt{f}_{\mathsf{iner}} := \begin{bmatrix} \rho \left(\ddot{\boldsymbol{u}}_0 + \ddot{\boldsymbol{u}} \right) \\ \boldsymbol{\mathcal{J}} \cdot \dot{\boldsymbol{\omega}} + \widetilde{\boldsymbol{\omega}} \cdot \boldsymbol{\mathcal{J}} \cdot \boldsymbol{\omega} \end{bmatrix}, \; \mathtt{f}_{\mathsf{int}}^{\mathsf{I}} := \begin{bmatrix} \boldsymbol{n} \\ \boldsymbol{m} \end{bmatrix}, \mathtt{f}_{\mathsf{int}}^{\mathsf{II}} := \begin{bmatrix} \boldsymbol{0} \\ -\widetilde{\boldsymbol{x}}_{\mathrm{c}}' \cdot \boldsymbol{n} \end{bmatrix}, \text{ and } \mathtt{f}_{\mathsf{ext}} := \begin{bmatrix} \bar{\boldsymbol{n}} \\ \bar{\boldsymbol{m}} \end{bmatrix}, \tag{2.5.1g}$$

are the 6×1 column vectors of the inertial, the internal, and the external forces and moments, respectively. Note that the column vector of the internal force and moment is split into $\mathtt{f}_{\mathsf{int}}^{\mathsf{I}}$ and

$\mathtt{f}_{\text{int}}^{\text{II}}$, where the former consists of internal force $\boldsymbol{n}$ and the local internal moment $\boldsymbol{m}$, while the latter is the moment $\boldsymbol{x}_c' \times \boldsymbol{n}$. The external force and moment vector, $\mathtt{f}_{\text{ext}}$, is a combination of gravitational and aerodynamic loads on the cable system, and we discuss these in the following section. The boundary conditions w_{bc} are discussed in Sec. 2.7.

2.6 External forces

The external forces (per unit length) due to *gravitational* and *aerodynamic* forces are discussed here. In a 6×1 column vector notation, we represent

$$\mathtt{f}_{\text{ext}} = \begin{bmatrix} \bar{\boldsymbol{n}} \\ \bar{\boldsymbol{m}} \end{bmatrix} = \mathtt{f}_{\text{grav}} + \mathtt{f}_{\text{aero}} \tag{2.6.1}$$

2.6.1 Gravitational force

Figure 1.8 shows the acceleration due to gravity g along the $\hat{\boldsymbol{e}}_1$ direction. The column vector of gravitational force

$$\mathtt{f}_{\text{grav}} = \begin{bmatrix} \rho g \\ 0 \\ 0 \\ 0 \\ 0 \\ 0 \end{bmatrix}. \tag{2.6.2}$$

2.6.2 Aerodynamic force

The aerodynamic force depends on three kinematic quantities, namely the air velocity $\boldsymbol{v}_{\text{air}}$, local velocity of the cable $\dot{\boldsymbol{u}}_0(t) + \dot{\boldsymbol{u}}(s,t)$ and the local unit tangent $\hat{\boldsymbol{x}}_c' = \boldsymbol{x}_c'/|\boldsymbol{x}_c'|$ along the cable, assuming that the cable element (Fig. 2.3) is a cylinder which is inclined in cross-flow [Hoerner, 1992; Païdoussis et al., 2010].

The velocity of air relative to the cable element is

$$\boldsymbol{v} = \boldsymbol{v}_{\text{air}} - \dot{\boldsymbol{u}}_0 - \dot{\boldsymbol{u}} = v_t \hat{\boldsymbol{e}}_t + v_n \hat{\boldsymbol{e}}_n, \tag{2.6.3}$$

where $v_t = \boldsymbol{v} \cdot \hat{\boldsymbol{e}}_t$ is tangential velocity and $v_n = \boldsymbol{v} \cdot \hat{\boldsymbol{e}}_n$ is the normal velocity, while the unit tangent, unit bi-normal and unit normal are, respectively,

$$\hat{\boldsymbol{e}}_t = \begin{cases} -\hat{\boldsymbol{x}}_c' & \text{if } \boldsymbol{v} \cdot \hat{\boldsymbol{x}}_c' < 0 \\ \hat{\boldsymbol{x}}_c' & \text{if } \boldsymbol{v} \cdot \hat{\boldsymbol{x}}_c' \geq 0 \end{cases}, \quad \hat{\boldsymbol{e}}_b = \frac{\hat{\boldsymbol{e}}_t \times \boldsymbol{v}}{|\hat{\boldsymbol{e}}_t \times \boldsymbol{v}|} \quad \text{and} \quad \hat{\boldsymbol{e}}_n = \hat{\boldsymbol{e}}_b \times \hat{\boldsymbol{e}}_t. \tag{2.6.4}$$

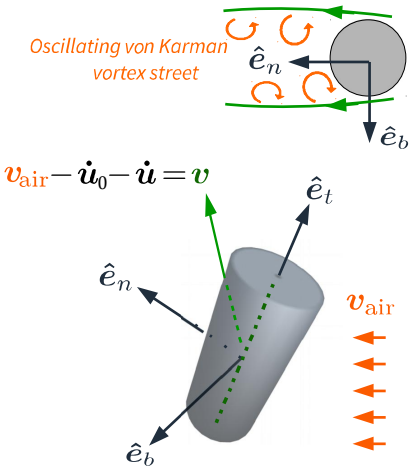

Figure 2.3: *Schematic of the beam element which is assumed to be a cylinder in 3D cross-flow (bottom), with von Karman vortex shedding (top).*

The choice above ensures that $\hat{e}_t$ - $\hat{e}_n$ is the plane in which air/wind flow takes place. The aerodynamic force and moment on the cylinder (cable element) of radius r are written in the following column vector notation:

$$\mathtt{f}_{\text{aero}} = \begin{bmatrix} \bar{n}^{\text{cyl}}_{\text{aero}} \\ \bar{m}^{\text{cyl}}_{\text{aero}} \end{bmatrix} = \begin{bmatrix} \mathtt{c}_t \rho_{\text{air}} \pi r v_t^2 \hat{e}_t \\ \mathbf{0} \end{bmatrix} + \begin{bmatrix} \mathtt{c}_n \rho_{\text{air}} r v_n^2 \hat{e}_n \\ \mathbf{0} \end{bmatrix} + \begin{bmatrix} \mathtt{c}_\kappa \rho_{\text{air}} r v_n^2 \sin(\omega_\kappa t)\, \hat{e}_b \\ \mathbf{0} \end{bmatrix}, \tag{2.6.5}$$

where the aerodynamic coefficients $\mathtt{c}_n \approx 1.0 - 1.3$ and $\mathtt{c}_t \approx 0.01\mathtt{c}_n - 0.03\mathtt{c}_n$ [Hoerner, 1992] for a cylinder in cross-flow. The *von Karman* coefficient and frequency are, respectively,

$$\mathtt{c}_\kappa \approx 0 - 1.0 \;\text{ and }\; \omega_\kappa = \frac{\mathrm{St}\,\pi |\boldsymbol{v}_{\text{air}}|}{r},$$

where the Strouhal number $\mathrm{St} = 0.22$ for a cylinder over a wide range of cross-flows [Den Hartog, 2013, pp. 305-306]. In (2.6.5), the first term (along $\hat{e}_t$) is the tangential/skin drag, the middle term (along $\hat{e}_n$) is the normal/pressure drag and the third term is the oscillating von Karman force (per unit length) acting along $\hat{e}_b$ direction.

2.7 Boundary conditions

The weak form of boundary conditions to the beam is discussed here. The translating hinge point (helicopter), as mentioned in Chapter 1, specifies a displacement-trajectory and offers a moment-free condition at $s = 0$ in the frame attached to the cable at the hinge:

$$\boldsymbol{u}_0(t) + \boldsymbol{u}(0,t) = \boldsymbol{u}_0(t) \;\text{ or }\; \boldsymbol{u}(0,t) = \mathbf{0},\; \boldsymbol{\mu}(0) = \mathbf{0} \;\text{ and }\; \boldsymbol{m}(0,t) = \mathbf{0},$$

where the admissible variation $\boldsymbol{\mu}$ satisfies the same condition as $\boldsymbol{u}$ at $s = 0$.

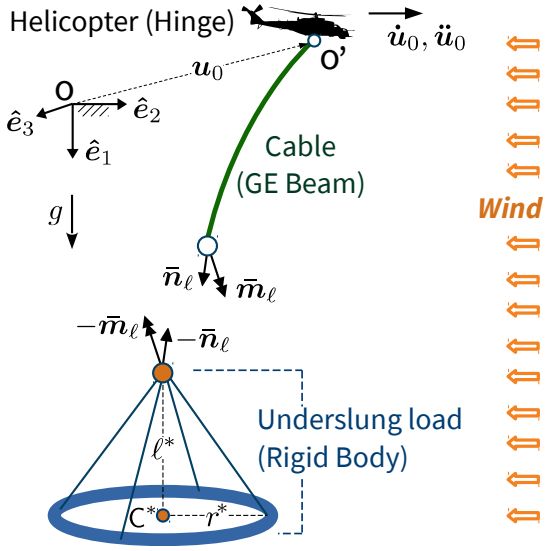

Figure 2.4: *Schematic showing the reaction force and moments at the point of connection between the towing cable and the underslung load.*

At the $s = \ell$ end of the cable in Fig. 2.4, the connection with the slung load (rigid body) offers equal and opposite reaction force and moment to the cable,

$$\boldsymbol{n}(\ell, t) = \bar{\boldsymbol{n}}_\ell(t) \quad \text{and} \quad \boldsymbol{m}(\ell, t) = \bar{\boldsymbol{m}}_\ell(t),$$

where the reaction force and moment from the slung load to the cable at the point of connection:

$$\mathtt{f}_\ell = \begin{bmatrix} \bar{\boldsymbol{n}}_\ell \\ \bar{\boldsymbol{m}}_\ell \end{bmatrix},$$

is computed in Sec. 3.3 of Chapter 3.

With these boundary conditions, we may rewrite (2.5.1e) as follows:

$$\begin{aligned} \mathrm{w}_{\mathrm{bc}} &= \boldsymbol{\mu}(\ell) \cdot \boldsymbol{n}(\ell, t) + \boldsymbol{\phi}(\ell) \cdot \boldsymbol{m}(\ell, t) - \boldsymbol{\mu}(0) \cdot \boldsymbol{n}(0, t) - \boldsymbol{\phi}(0) \cdot \boldsymbol{m}(0, t) \\ &= \boldsymbol{\mu}(\ell) \cdot \bar{\boldsymbol{n}}_\ell(t) + \boldsymbol{\phi}(\ell) \cdot \bar{\boldsymbol{m}}_\ell(t) = \eta^{\mathsf{T}}(\ell) \mathtt{f}^*_\ell(t). \end{aligned} \tag{2.7.1}$$

2.8 Planar (2D) GE beam

When the beam's motion is restricted to the $\hat{\boldsymbol{e}}_1$-$\hat{\boldsymbol{e}}_2$ plane, the governing equations (2.2.7a) and (2.2.7b) reduce to, respectively,

$$\boldsymbol{n}' + \bar{\boldsymbol{n}} = \rho\,(\ddot{\boldsymbol{u}}_0 + \ddot{\boldsymbol{u}}) \tag{2.8.1a}$$

and

$$m_3'\hat{\boldsymbol{e}}_3 + \boldsymbol{x}_{\mathrm{c}}' \times \boldsymbol{n} + \bar{m}_3\hat{\boldsymbol{e}}_3 = \mathcal{J}\dot{\boldsymbol{\omega}} = \mathcal{J}\ddot{\varphi}_3\hat{\boldsymbol{e}}_3, \tag{2.8.1b}$$

where $\boldsymbol{u}_0 + \boldsymbol{u} = (u_{01} + u_1)\hat{\boldsymbol{e}}_1 + (u_{02} + u_2)\hat{\boldsymbol{e}}_2$ is the total displacement of the centoidal axis, $\boldsymbol{x}_{\mathrm{c}}' = (1 + u_1')\hat{\boldsymbol{e}}_1 + u_2'\hat{\boldsymbol{e}}_2$ is the tangent, $\boldsymbol{n} = n_1\hat{\boldsymbol{e}}_1 + n_2\hat{\boldsymbol{e}}_2$ in the internal force, ρ is the mass

density (per unit length) and $\mathcal{J} = J = \rho I$ is the polar mass moment of inertia. The equations (2.8.1a) and (2.8.1b) can be written in the following matrix form:

$$\mathtt{f}_{\text{iner}} = \left(\mathtt{f}^{\text{I}}_{\text{int}}\right)' - \mathtt{f}^{\text{II}}_{\text{int}} + \mathtt{f}_{\text{ext}}, \tag{2.8.2}$$

$$\text{where } \mathtt{f}_{\text{iner}} = \begin{bmatrix} \rho\left(\ddot{u}_{01} + \ddot{u}_1\right) \\ \rho\left(\ddot{u}_{02} + \ddot{u}_2\right) \\ \mathcal{J}\ddot{\varphi}_3 \end{bmatrix}, \ \mathtt{f}^{\text{I}}_{\text{int}} = \begin{bmatrix} n_1 \\ n_2 \\ m_3 \end{bmatrix}, \ \mathtt{f}^{\text{II}}_{\text{int}} = \begin{bmatrix} 0 \\ 0 \\ u_2' n_1 - (1 + u_1') n_2 \end{bmatrix}$$

and $\mathtt{f}_{\text{ext}} = \begin{bmatrix} \rho g \\ 0 \\ 0 \end{bmatrix} + \mathtt{f}_{\text{aero}}$.

In (2.8.2), the aerodynamic load vector

$$\mathtt{f}_{\text{aero}} = \mathtt{c}_t \rho_{\text{air}} \pi r v_t^2 \left[\hat{\boldsymbol{e}}_t\right] + \mathtt{c}_n \rho_{\text{air}} r v_n^2 \left[\hat{\boldsymbol{e}}_n\right], \tag{2.8.3}$$

$$\text{where } \hat{\boldsymbol{e}}_t = \begin{cases} -\hat{\boldsymbol{x}}_c' & \text{if } \boldsymbol{v} \cdot \hat{\boldsymbol{x}}_c' < 0 \\ \hat{\boldsymbol{x}}_c' & \text{if } \boldsymbol{v} \cdot \hat{\boldsymbol{x}}_c' \geq 0 \end{cases}, \quad \hat{\boldsymbol{e}}_n = \hat{\boldsymbol{e}}_3 \times \hat{\boldsymbol{e}}_t, \ v_t = \boldsymbol{v} \cdot \hat{\boldsymbol{e}}_t \ \text{ and } \ v_n = \boldsymbol{v} \cdot \hat{\boldsymbol{e}}_n.$$

The rotation tensor (2.b.4) is defined by a planar rotation by angle $\varphi_3(s,t)$ about the $\hat{\boldsymbol{e}}_3$ axis,

$$[\boldsymbol{R}] = \begin{bmatrix} \cos\varphi_3 & -\sin\varphi_3 & 0 \\ \sin\varphi_3 & \cos\varphi_3 & 0 \\ 0 & 0 & 1 \end{bmatrix},$$

and the strain measures are

$$\begin{bmatrix} \gamma_1 \\ \gamma_2 \\ \kappa_3 \end{bmatrix} = \begin{bmatrix} 1 + u_1' - \cos\varphi_3 \\ u_2' - \sin\varphi_3 \\ \varphi_3' \end{bmatrix}.$$

The material and spatial elasticity tensors are, respectively,

$$[\boldsymbol{C}] = \text{diag}\left([EA, kGA, EI]\right) \quad \text{and} \quad [\boldsymbol{\mathcal{C}}] = [\boldsymbol{R} \cdot \boldsymbol{C} \cdot \boldsymbol{R}^{\mathsf{T}}].$$

Thus, the constitutive relationship is

$$\begin{bmatrix} n_1 \\ n_2 \\ m_3 \end{bmatrix} = [\boldsymbol{\mathcal{C}}] \begin{bmatrix} \gamma_1 \\ \gamma_2 \\ \kappa_3 \end{bmatrix} = [\boldsymbol{\mathcal{C}}] \begin{bmatrix} 1 + u_1' - \cos\varphi_3 \\ u_2' - \sin\varphi_3 \\ \varphi_3' \end{bmatrix}. \tag{2.8.4}$$

Differentiating the above relations we obtain

$$\begin{bmatrix} n_1 \\ n_2 \\ m_3 \end{bmatrix}' = [\boldsymbol{\mathcal{C}}]' \begin{bmatrix} 1 + u_1' - \cos\varphi_3 \\ u_2' - \sin\varphi_3 \\ \varphi_3' \end{bmatrix} + [\boldsymbol{\mathcal{C}}] \begin{bmatrix} u_1' \\ u_2' \\ \varphi_3' \end{bmatrix}' + \varphi_3' [\boldsymbol{\mathcal{C}}] \begin{bmatrix} \sin\varphi_3 \\ \cos\varphi_3 \\ 0 \end{bmatrix}, \tag{2.8.5}$$

where

$$[\boldsymbol{\mathcal{C}}]' = (EA - kGA)\varphi_3' \begin{bmatrix} -2\sin\varphi_3\cos\varphi_3 & \cos^2\varphi_3 - \sin^2\varphi_3 & 0 \\ \cos^2\varphi_3 - \sin^2\varphi_3 & 2\sin\varphi_3\cos\varphi_3 & 0 \\ 0 & 0 & 0 \end{bmatrix}$$

Substituting (2.8.4) and (2.8.5) into (2.8.2), we obtain the final form of governing equations:

$$\begin{bmatrix} \rho\,(\ddot{u}_{01} + \ddot{u}_1) \\ \rho\,(\ddot{u}_{02} + \ddot{u}_2) \\ \mathcal{J}\ddot{\varphi}_3 \end{bmatrix} = [\boldsymbol{\mathcal{C}}]' \begin{bmatrix} 1 + u_1' - \cos\varphi_3 \\ u_2' - \sin\varphi_3 \\ \varphi_3' \end{bmatrix} + [\boldsymbol{\mathcal{C}}] \begin{bmatrix} u_1' \\ u_2' \\ \varphi_3' \end{bmatrix}' + \varphi_3' [\boldsymbol{\mathcal{C}}] \begin{bmatrix} \sin\varphi_3 \\ \cos\varphi_3 \\ 0 \end{bmatrix} + \begin{bmatrix} \rho g \\ 0 \\ 0 \end{bmatrix} + \mathtt{f}_{\text{aero}}$$
$$+ \begin{bmatrix} 0 \\ 0 \\ [(1 + u_1')\sin\varphi_3 - u_2'\cos\varphi_3][(EA - kGA)\{(1 + u_1')\cos\varphi_3 + u_2'\sin\varphi_3\} - EA] \end{bmatrix}. \tag{2.8.6}$$

Appendix

2.a Useful vector and tensor identities

Here we give proofs of the vector and tensor identities used at various places in this work.

1. $\hat{\boldsymbol{a}} \otimes \hat{\boldsymbol{a}} - (\hat{\boldsymbol{a}} \cdot \hat{\boldsymbol{a}})\mathbf{1} = \widetilde{\boldsymbol{a}}^2$

   For any arbitrary three dimensional vector $\boldsymbol{v}$,

   $$\begin{aligned}\{\hat{\boldsymbol{a}} \otimes \hat{\boldsymbol{a}} - (\hat{\boldsymbol{a}} \cdot \hat{\boldsymbol{a}})\mathbf{1}\} \cdot \boldsymbol{v} &= \hat{\boldsymbol{a}} \otimes \hat{\boldsymbol{a}} \cdot \boldsymbol{v} - (\hat{\boldsymbol{a}} \cdot \hat{\boldsymbol{a}})\boldsymbol{v} \\ &= (\hat{\boldsymbol{a}} \cdot \boldsymbol{v})\hat{\boldsymbol{a}} - (\hat{\boldsymbol{a}} \cdot \hat{\boldsymbol{a}})\boldsymbol{v} \\ &= \hat{\boldsymbol{a}} \times (\hat{\boldsymbol{a}} \times \boldsymbol{v}) \\ &= \widetilde{\boldsymbol{a}}^2 \cdot \boldsymbol{v}, \end{aligned} \tag{2.a.1}$$

   where as per our notation $\widetilde{\boldsymbol{a}}$ is the skew-symmetric spin tensor corresponding to the unit vector $\hat{\boldsymbol{a}}$.

2. $\widetilde{\boldsymbol{a}}^3 = -\widetilde{\boldsymbol{a}}, \quad \widetilde{\boldsymbol{a}}^4 = -\widetilde{\boldsymbol{a}}^2, \quad \widetilde{\boldsymbol{a}} \cdot \dot{\widetilde{\boldsymbol{a}}} \cdot \widetilde{\boldsymbol{a}} = \widetilde{\boldsymbol{a}} \cdot \dot{\widetilde{\boldsymbol{a}}} \cdot \widetilde{\boldsymbol{a}}^2 = \mathbf{O}, \text{ and } \dot{\widetilde{\boldsymbol{a}}} \cdot \widetilde{\boldsymbol{a}}^3 = -\dot{\widetilde{\boldsymbol{a}}} \cdot \widetilde{\boldsymbol{a}}$

   Let $\boldsymbol{v}$ be any three dimensional vector. Then,

   $$\begin{aligned}\widetilde{\boldsymbol{a}}^3 \cdot \boldsymbol{v} &= \hat{\boldsymbol{a}} \times [\hat{\boldsymbol{a}} \times (\hat{\boldsymbol{a}} \times \boldsymbol{v})] \\ &= \hat{\boldsymbol{a}} \times [(\hat{\boldsymbol{a}} \cdot \boldsymbol{v})\hat{\boldsymbol{a}} - (\hat{\boldsymbol{a}} \cdot \hat{\boldsymbol{a}})\boldsymbol{v}] \\ &= (\hat{\boldsymbol{a}} \cdot \boldsymbol{v})\hat{\boldsymbol{a}} \times \hat{\boldsymbol{a}} - (1)\hat{\boldsymbol{a}} \times \boldsymbol{v} \\ &= (\hat{\boldsymbol{a}} \cdot \boldsymbol{v})\mathbf{0} - (1)\widetilde{\boldsymbol{a}} \cdot \boldsymbol{v} \\ &= -\widetilde{\boldsymbol{a}} \cdot \boldsymbol{v}, \end{aligned}$$

   which implies that

   $$\widetilde{\boldsymbol{a}}^3 = -\widetilde{\boldsymbol{a}}. \tag{2.a.2a}$$

   Multiplying the above by $\widetilde{\boldsymbol{a}}$, we deduce that

   $$\widetilde{\boldsymbol{a}}^4 = -\widetilde{\boldsymbol{a}}^2. \tag{2.a.2b}$$

   Now, the remaining three identities are proved while observing that the rate (derivative) of a unit vector is orthogonal to that unit vector, i.e., $\hat{\boldsymbol{a}} \cdot \dot{\hat{\boldsymbol{a}}} = 0$,

   $$\widetilde{\boldsymbol{a}} \cdot \dot{\widetilde{\boldsymbol{a}}} \cdot \widetilde{\boldsymbol{a}} \cdot \boldsymbol{v} = \hat{\boldsymbol{a}} \times [\dot{\hat{\boldsymbol{a}}} \times (\hat{\boldsymbol{a}} \times \boldsymbol{v})]$$

$$= \hat{\boldsymbol{a}} \times [(\dot{\hat{\boldsymbol{a}}} \cdot \boldsymbol{v})\hat{\boldsymbol{a}} - (\dot{\hat{\boldsymbol{a}}} \cdot \hat{\boldsymbol{a}})\boldsymbol{v}]$$

$$= (\dot{\hat{\boldsymbol{a}}} \cdot \boldsymbol{v})\hat{\boldsymbol{a}} \times \hat{\boldsymbol{a}} - (0)\hat{\boldsymbol{a}} \times \boldsymbol{v} = \boldsymbol{0},$$

where $\boldsymbol{0}$ is the zero vector. As $\boldsymbol{v}$ is arbitrary, we deduce

$$\widetilde{\boldsymbol{a}} \cdot \dot{\widetilde{\boldsymbol{a}}} \cdot \widetilde{\boldsymbol{a}} = \boldsymbol{O}, \tag{2.a.2c}$$

where $\boldsymbol{O}$ is the zero tensor.

Post-multiplying the above by $\widetilde{\boldsymbol{a}}$, we obtain the relation

$$\widetilde{\boldsymbol{a}} \cdot \dot{\widetilde{\boldsymbol{a}}} \cdot \widetilde{\boldsymbol{a}}^2 = \boldsymbol{O}. \tag{2.a.2d}$$

Finally, pre-Multiplying (2.a.2a) by $\dot{\widetilde{\boldsymbol{a}}}$, we obtain

$$\dot{\widetilde{\boldsymbol{a}}} \cdot \widetilde{\boldsymbol{a}}^3 = -\dot{\widetilde{\boldsymbol{a}}} \cdot \widetilde{\boldsymbol{a}}. \tag{2.a.2e}$$

3. $\operatorname{ax}(\widetilde{\boldsymbol{a}} \cdot \dot{\widetilde{\boldsymbol{a}}} - \dot{\widetilde{\boldsymbol{a}}} \cdot \widetilde{\boldsymbol{a}}) = \widetilde{\boldsymbol{a}} \cdot \dot{\boldsymbol{a}}$

For any three arbitrary vectors $\boldsymbol{v}$, $\boldsymbol{y}$ and $\boldsymbol{z}$, we have

$$(\widetilde{\boldsymbol{y}} \cdot \widetilde{\boldsymbol{z}} - \widetilde{\boldsymbol{z}} \cdot \widetilde{\boldsymbol{y}}) \cdot \boldsymbol{v} = \boldsymbol{y} \times (\boldsymbol{z} \times \boldsymbol{v}) - \boldsymbol{z} \times (\boldsymbol{y} \times \boldsymbol{v})$$

$$= (\boldsymbol{y} \times \boldsymbol{z}) \times \boldsymbol{v}$$

$$= (\widetilde{\boldsymbol{y} \cdot \boldsymbol{z}}) \cdot \boldsymbol{v}.$$

Therefore, setting $\boldsymbol{y} = \hat{\boldsymbol{a}}$ and $\boldsymbol{z} = \dot{\hat{\boldsymbol{a}}}$ the above relation, we deduce

$$\widetilde{\boldsymbol{a}} \cdot \dot{\widetilde{\boldsymbol{a}}} - \dot{\widetilde{\boldsymbol{a}}} \cdot \widetilde{\boldsymbol{a}} = (\widetilde{\widetilde{\boldsymbol{a}} \cdot \dot{\hat{\boldsymbol{a}}}}),$$

whose axial vectors are

$$\operatorname{ax}(\widetilde{\boldsymbol{a}} \cdot \dot{\widetilde{\boldsymbol{a}}} - \dot{\widetilde{\boldsymbol{a}}} \cdot \widetilde{\boldsymbol{a}}) = \widetilde{\boldsymbol{a}} \cdot \dot{\hat{\boldsymbol{a}}}. \tag{2.a.3}$$

4. $\vartheta\, \dot{\hat{\boldsymbol{a}}} = -\widetilde{\boldsymbol{a}}^2 \cdot \dot{\boldsymbol{\varphi}} = -\vartheta\, \widetilde{\boldsymbol{a}}^2 \cdot \dot{\hat{\boldsymbol{a}}}$

From the derivative of $\boldsymbol{\varphi} = \vartheta \hat{\boldsymbol{a}}$ (2.b.3), we obtain

$$\vartheta \dot{\hat{\boldsymbol{a}}} = \dot{\boldsymbol{\varphi}} - \dot{\vartheta} \hat{\boldsymbol{a}},$$

which is pre-multiplied by $-\widetilde{\boldsymbol{a}}^2$ on both the sides to obtain the desired identity,

$$\begin{aligned}
-\vartheta\, \widetilde{\boldsymbol{a}}^2 \cdot \dot{\hat{\boldsymbol{a}}} &= -\widetilde{\boldsymbol{a}}^2 \cdot (\vartheta \dot{\hat{\boldsymbol{a}}}) && = -\widetilde{\boldsymbol{a}}^2 \cdot (\dot{\boldsymbol{\varphi}} - \dot{\vartheta} \hat{\boldsymbol{a}}) \\
&= -\hat{\boldsymbol{a}} \times [\hat{\boldsymbol{a}} \times (\vartheta \dot{\hat{\boldsymbol{a}}})] && = -\widetilde{\boldsymbol{a}}^2 \cdot \dot{\boldsymbol{\varphi}} + \dot{\vartheta}\, \widetilde{\boldsymbol{a}}^2 \cdot \hat{\boldsymbol{a}} \\
&= -\vartheta(\hat{\boldsymbol{a}} \cdot \dot{\hat{\boldsymbol{a}}})\hat{\boldsymbol{a}} + (\hat{\boldsymbol{a}} \cdot \hat{\boldsymbol{a}})(\vartheta \dot{\hat{\boldsymbol{a}}}) && = -\widetilde{\boldsymbol{a}}^2 \cdot \dot{\boldsymbol{\varphi}} + \dot{\vartheta} \hat{\boldsymbol{a}} \times (\hat{\boldsymbol{a}} \times \hat{\boldsymbol{a}}) \\
&= -\vartheta(0)\hat{\boldsymbol{a}} + (1)(\vartheta \dot{\hat{\boldsymbol{a}}}) && = -\widetilde{\boldsymbol{a}}^2 \cdot \dot{\boldsymbol{\varphi}} + \dot{\vartheta} \boldsymbol{0} \\
&= \vartheta \dot{\hat{\boldsymbol{a}}} && = -\widetilde{\boldsymbol{a}}^2 \cdot \dot{\boldsymbol{\varphi}}.
\end{aligned} \tag{2.a.4}$$

2.b Rotation tensor

We now discuss the properties of the rotation tensor $\boldsymbol{R}$ and its parameterization into a minimum independent set of parameters.

All three-dimensional rotation tensors belong to the Special Orthogonal or the SO(3) group. The determinant of the members of this group is 1. A *group* is defined as a set which contains the product and the inverse of its members. For example, if $\boldsymbol{R}$ and $\boldsymbol{T}$ belong to the group SO(3) then it implies that $\boldsymbol{R}\cdot\boldsymbol{T}$, $\boldsymbol{T}\cdot\boldsymbol{R}$, $\boldsymbol{R}^{-1}$, and $\boldsymbol{T}^{-1}$, also belong to the SO(3) group. Similarly, all skew-symmetric tensors belong to another kind of group known as the so(3) group. According to Hall [2015], so(3) is the *Lie Algebra* of the rotation group SO(3). That is, when a skew-symmetric tensor $\widetilde{\boldsymbol{\varphi}} = -\widetilde{\boldsymbol{\varphi}}^{\mathsf{T}}$ belongs to the so(3) group, then its exponential $\exp(\widetilde{\boldsymbol{\varphi}})$ is an orthogonal tensor belonging to the SO(3) group. Thus, $\exp(\widetilde{\boldsymbol{\varphi}})$ is a rotation tensor.

Since eigenvalues of a skew-symmetric tensor are 0 and $\pm i\vartheta$, where ϑ is a real number, then the eigenvalues of its exponential will be 1 and $\exp(\pm i\vartheta)$. This means that the rotation tensor $\boldsymbol{R} = \exp(\widetilde{\boldsymbol{\varphi}})$ is a *proper* orthogonal tensor which satisfies the following relations:

$$\boldsymbol{R}^{-1} = \boldsymbol{R}^{\mathsf{T}},\ \boldsymbol{R}^{\mathsf{T}}\cdot\boldsymbol{R} = \boldsymbol{R}\cdot\boldsymbol{R}^{\mathsf{T}} = \mathbf{1}, \tag{2.b.1a}$$

where $\mathbf{1}$ is an identity tensor. The determinant (third invariant) of $\boldsymbol{R}$ is the product of its eigenvalues,

$$\det(\boldsymbol{R}) = 1\exp(i\vartheta)\exp(-i\vartheta) = 1. \tag{2.b.1b}$$

The trace (first invariant) of $\boldsymbol{R}$ is given by the sum of its eigenvalues,

$$\operatorname{tr}(\boldsymbol{R}) = 1 + \exp(i\vartheta) + \exp(-i\vartheta) = 1 + 2\cos\vartheta, \tag{2.b.1c}$$

which defines the angle of rotation

$$\vartheta := \arccos\frac{\operatorname{tr}(\boldsymbol{R}) - 1}{2}. \tag{2.b.1d}$$

Let $\hat{\boldsymbol{a}}$ be the unit eigenvector of $\boldsymbol{R}$ corresponding to the unit eigenvalue,

$$\boldsymbol{R}\cdot\hat{\boldsymbol{a}} = \hat{\boldsymbol{a}}. \tag{2.b.2a}$$

Then the rotation or transformation of any vector is quantified as a rotation of that vector by an angle ϑ about the axis vector $\hat{\boldsymbol{a}}$, which allows the rotation tensor $\boldsymbol{R}$ to be represented by the following *axis-angle formula* [Beatty, 2013; Spencer, 2012]:

$$\boldsymbol{R} = \cos\vartheta\mathbf{1} + \sin\vartheta\,\widetilde{\boldsymbol{a}} + (1-\cos\vartheta)\,\hat{\boldsymbol{a}}\otimes\hat{\boldsymbol{a}},$$

$$= \cos\vartheta\mathbf{1} + \sin\vartheta\,\widetilde{\hat{\boldsymbol{a}}} + (1-\cos\vartheta)\,(\hat{\boldsymbol{a}}\otimes\hat{\boldsymbol{a}} - \mathbf{1} + \mathbf{1}),$$

$$= (\cos\vartheta + 1 - \cos\vartheta)\mathbf{1} + \sin\vartheta\,\widetilde{\hat{\boldsymbol{a}}} + (1-\cos\vartheta)\,[\hat{\boldsymbol{a}}\otimes\hat{\boldsymbol{a}} - (\hat{\boldsymbol{a}}\cdot\hat{\boldsymbol{a}})\mathbf{1}]$$

$$= \mathbf{1} + \sin\vartheta\,\widetilde{\hat{\boldsymbol{a}}} + (1-\cos\vartheta)\,[\hat{\boldsymbol{a}}\otimes\hat{\boldsymbol{a}} - (\hat{\boldsymbol{a}}\cdot\hat{\boldsymbol{a}})\mathbf{1}]\,, \tag{2.b.2b}$$

where $\widetilde{\hat{\boldsymbol{a}}}$ is the skew-symmetric spin tensor associated with the unit vector $\hat{\boldsymbol{a}}$. Using (2.a.1) in (2.b.2b) we obtain the following expression of the rotation tensor:

$$\boldsymbol{R} = \mathbf{1} + \sin\vartheta\,\widetilde{\hat{\boldsymbol{a}}} + (1-\cos\vartheta)\,\widetilde{\hat{\boldsymbol{a}}}^2. \tag{2.b.2c}$$

By expanding (2.b.2c) in series of ϑ and simplifying using (2.a.2), we get

$$\begin{aligned}
\boldsymbol{R} &= \mathbf{1} + \left(\vartheta - \frac{\vartheta^3}{3!} + \frac{\vartheta^5}{5!} - \dots\right)\widetilde{\hat{\boldsymbol{a}}} + \left(1 - 1 + \frac{\vartheta^2}{2!} - \frac{\vartheta^4}{4!} + \dots\right)\widetilde{\hat{\boldsymbol{a}}}^2 \\
&= \mathbf{1} + \left(\vartheta\widetilde{\hat{\boldsymbol{a}}} - \frac{\vartheta^3}{3!}\widetilde{\hat{\boldsymbol{a}}} + \frac{\vartheta^5}{5!}\widetilde{\hat{\boldsymbol{a}}} - \dots\right) + \left(\frac{\vartheta^2}{2!}\widetilde{\hat{\boldsymbol{a}}}^2 - \frac{\vartheta^4}{4!}\widetilde{\hat{\boldsymbol{a}}}^2 + \dots\right) \\
&= \mathbf{1} + \left(\vartheta\widetilde{\hat{\boldsymbol{a}}} + \frac{\vartheta^3}{3!}\widetilde{\hat{\boldsymbol{a}}}^3 + \dots\right) + \left(\frac{\vartheta^2}{2!}\widetilde{\hat{\boldsymbol{a}}}^2 + \frac{\vartheta^4}{4!}\widetilde{\hat{\boldsymbol{a}}}^4 + \dots\right) \\
&= \mathbf{1} + \vartheta\widetilde{\hat{\boldsymbol{a}}} + \frac{\vartheta^2}{2!}\widetilde{\hat{\boldsymbol{a}}}^2 + \frac{\vartheta^3}{3!}\widetilde{\hat{\boldsymbol{a}}}^3 + \frac{\vartheta^4}{4!}\widetilde{\hat{\boldsymbol{a}}}^4 + \dots = \exp(\vartheta\widetilde{\hat{\boldsymbol{a}}}),
\end{aligned} \tag{2.b.2d}$$

which is the *exponential map* of $\vartheta\widetilde{\hat{\boldsymbol{a}}}$.

Now, if we define a rotation vector

$$\boldsymbol{\varphi} = \vartheta\hat{\boldsymbol{a}}, \tag{2.b.3}$$

so that $\vartheta = (\boldsymbol{\varphi}\cdot\boldsymbol{\varphi})^{1/2}$, $\hat{\boldsymbol{a}} = \boldsymbol{\varphi}/\vartheta$, and $\widetilde{\boldsymbol{\varphi}} = \mathrm{sk}\,(\boldsymbol{\varphi})$, then (2.b.2c) can be written as

$$\boldsymbol{R} = \mathbf{1} + \frac{\sin\vartheta}{\vartheta}\,\widetilde{\boldsymbol{\varphi}} + \frac{1-\cos\vartheta}{\vartheta^2}\,\widetilde{\boldsymbol{\varphi}}^2, \tag{2.b.4}$$

which is commonly known as the Rodrigues' formula [Simo & Vu-Quoc, 1986a], and (2.b.2d) can be expressed as the exponential map of $\widetilde{\boldsymbol{\varphi}}$:

$$\boldsymbol{R} = \exp(\widetilde{\boldsymbol{\varphi}}). \tag{2.b.5}$$

Alternatively, the exponential map (2.b.5) may also be obtained by solving the differential equation:

$$\frac{d\boldsymbol{x}_{\mathrm{cp}}}{d\vartheta} = \left(\frac{d}{d\vartheta}\boldsymbol{R}\right)\cdot\mathbf{x}_{\mathrm{cp}} = \left(\frac{d}{d\vartheta}\boldsymbol{R}\right)\cdot\boldsymbol{R}^{\mathsf{T}}\cdot\boldsymbol{x}_{\mathrm{cp}}, \tag{2.b.6}$$

which is obtained by differentiating (2.1.4c) with respect to ϑ. Here it is easily verified using (2.b.2c) and (2.a.2) that

$$\left(\frac{d}{d\vartheta}\boldsymbol{R}\right)\cdot\boldsymbol{R}^{\mathsf{T}} = \left(\cos\vartheta\,\widetilde{\hat{\boldsymbol{a}}} + \sin\vartheta\,\widetilde{\hat{\boldsymbol{a}}}^2\right)\cdot\left[\mathbf{1} - \sin\vartheta\widetilde{\hat{\boldsymbol{a}}} + (1-\cos\vartheta)\widetilde{\hat{\boldsymbol{a}}}^2\right]$$

$$
\begin{aligned}
&= \left(\cos\vartheta\,\widetilde{\boldsymbol{a}} + \sin\vartheta\,\widetilde{\boldsymbol{a}}^2\right) - \sin\vartheta\left(\cos\vartheta\,\widetilde{\boldsymbol{a}}^2 + \sin\vartheta\,\widetilde{\boldsymbol{a}}^3\right) \\
&\quad + (1-\cos\vartheta)\left(\cos\vartheta\,\widetilde{\boldsymbol{a}}^3 + \sin\vartheta\,\widetilde{\boldsymbol{a}}^4\right) \\
&= \left(\cos\vartheta\,\widetilde{\boldsymbol{a}} + \sin\vartheta\,\widetilde{\boldsymbol{a}}^2\right) - \sin\vartheta\,\left(\cos\vartheta\,\widetilde{\boldsymbol{a}}^2 - \sin\vartheta\,\widetilde{\boldsymbol{a}}\right) \\
&\quad + (1-\cos\vartheta)\left(-\cos\vartheta\,\widetilde{\boldsymbol{a}} - \sin\vartheta\,\widetilde{\boldsymbol{a}}^2\right) \\
&= \left(\cos\vartheta + \sin^2\vartheta - \cos\vartheta + \cos^2\vartheta\right)\widetilde{\boldsymbol{a}} \\
&\quad + \left(\sin\vartheta - \sin\vartheta\cos\vartheta - \sin\vartheta + \cos\vartheta\sin\vartheta\right)\widetilde{\boldsymbol{a}}^2 = \widetilde{\boldsymbol{a}}.
\end{aligned}
\tag{2.b.7}
$$

Thus, (2.b.6) reads

$$
\frac{d\boldsymbol{x}_{\text{cp}}}{d\vartheta} = \widetilde{\boldsymbol{a}}\cdot\boldsymbol{x}_{\text{cp}}, \quad \text{with } \boldsymbol{x}_{\text{cp}} = \mathbf{x}_{\text{cp}} \text{ when } \vartheta = 0. \tag{2.b.8}
$$

The solution to this linear differential equation is

$$
\boldsymbol{x}_{\text{cp}} = \exp(\vartheta\widetilde{\boldsymbol{a}})\cdot\mathbf{x}_{\text{cp}} = \exp(\widetilde{\boldsymbol{\varphi}})\cdot\mathbf{x}_{\text{cp}}. \tag{2.b.9}
$$

Thus, by comparing (2.b.9) and (2.1.4c) we can confirm that $\boldsymbol{R} = \exp(\widetilde{\boldsymbol{\varphi}})$ is the exponential map given by (2.b.5). This completes the discussion on the representation of rotation tensor as an exponential map, and in the next section we discuss its differentiation.

2.c Derivatives of rotation tensor

The rotation parameters ϑ and $\hat{\boldsymbol{a}}$, or the vector $\boldsymbol{\varphi} = \vartheta\hat{\boldsymbol{a}}$, are functions of both the space coordinate s and the time t. The derivatives of the rotation tensor $\boldsymbol{R}$ with respect to s and t are important when calculating the angular velocity, angular acceleration, curvature, and other similar quantities. The differentiation of the orthogonality relation (2.b.1a) yields skew-symmetric tensors,

$$
\dot{\boldsymbol{R}}\cdot\boldsymbol{R}^{\mathsf{T}} = -\boldsymbol{R}\cdot\dot{\boldsymbol{R}}^{\mathsf{T}}, \quad \text{or} \quad \boldsymbol{R}'\cdot\boldsymbol{R}^{\mathsf{T}} = -\boldsymbol{R}\cdot\boldsymbol{R}'^{\mathsf{T}}, \tag{2.c.1}
$$

where we denote $\dot{\square} \equiv d\square/dt$ and $\square' \equiv d\square/ds$. The tensor quantity $\dot{\boldsymbol{R}}\cdot\boldsymbol{R}^{\mathsf{T}} =: \widetilde{\boldsymbol{\omega}}$ is called as the angular velocity, while $\boldsymbol{R}'\cdot\boldsymbol{R}^{\mathsf{T}} =: \widetilde{\boldsymbol{\kappa}}$ is the curvature. In this section, we derive the parametric forms of these quantities in terms of ϑ and $\hat{\boldsymbol{a}}$, or $\boldsymbol{\varphi}$.

The parametric form of $\dot{\boldsymbol{R}}$ in terms of ϑ and $\hat{\boldsymbol{a}}$ is obtained upon differentiation of (2.b.2c),

$$
\dot{\boldsymbol{R}} = \dot{\vartheta}\cos\vartheta\,\widetilde{\boldsymbol{a}} + \sin\vartheta\,\dot{\widetilde{\boldsymbol{a}}} + \dot{\vartheta}\sin\vartheta\,\widetilde{\boldsymbol{a}}^2 + (1-\cos\vartheta)\left(\dot{\widetilde{\boldsymbol{a}}}\cdot\widetilde{\boldsymbol{a}} + \widetilde{\boldsymbol{a}}\cdot\dot{\widetilde{\boldsymbol{a}}}\right), \tag{2.c.2}
$$

where $\widetilde{\boldsymbol{a}} = \text{sk}(\hat{\boldsymbol{a}})$ and $\dot{\widetilde{\boldsymbol{a}}} = \text{sk}(\dot{\hat{\boldsymbol{a}}})$. The parametric form of $\boldsymbol{R}'$ is analogous to (2.c.2), where the $\dot{\square}$ is replaced by the $\square'$.

Angular velocity is obtained in terms of the parameters ϑ and $\hat{\boldsymbol{a}}$ by using (2.c.2) and (2.a.2),

$$\widetilde{\boldsymbol{\omega}} = \dot{\boldsymbol{R}} \cdot \boldsymbol{R}^{\mathsf{T}} = \dot{\vartheta}\widetilde{\boldsymbol{a}} + \sin\vartheta\,\dot{\widetilde{\boldsymbol{a}}} + (1-\cos\vartheta)\left(\widetilde{\boldsymbol{a}}\cdot\dot{\widetilde{\boldsymbol{a}}} - \dot{\widetilde{\boldsymbol{a}}}\cdot\widetilde{\boldsymbol{a}}\right), \tag{2.c.3}$$

and whose axial vector

$$\boldsymbol{\omega} = \mathrm{ax}\,(\widetilde{\boldsymbol{\omega}}) = \dot{\vartheta}\hat{\boldsymbol{a}} + \sin\vartheta\,\dot{\hat{\boldsymbol{a}}} + (1-\cos\vartheta)\widetilde{\boldsymbol{a}}\cdot\dot{\hat{\boldsymbol{a}}}, \tag{2.c.4}$$

where we used (2.a.3).

However, to represent the $\boldsymbol{\omega}$ in terms of parameter $\boldsymbol{\varphi}$, we replace the term $\dot{\vartheta}\hat{\boldsymbol{a}}$ in (2.c.4) by

$$\dot{\vartheta}\hat{\boldsymbol{a}} = \dot{\boldsymbol{\varphi}} + \widetilde{\boldsymbol{a}}^2\cdot\dot{\boldsymbol{\varphi}}, \tag{2.c.5}$$

which is obtained by differentiating (2.b.3) and using (2.a.4). Then (2.c.4) simplifies as follows,

$$\boldsymbol{\omega} = \dot{\boldsymbol{\varphi}} + \widetilde{\boldsymbol{a}}^2\cdot\dot{\boldsymbol{\varphi}} - \frac{\sin\vartheta}{\vartheta}\widetilde{\boldsymbol{a}}^2\cdot\dot{\boldsymbol{\varphi}} + \frac{1-\cos\vartheta}{\vartheta}\widetilde{\boldsymbol{a}}\cdot\dot{\boldsymbol{\varphi}} = \boldsymbol{T}\cdot\dot{\boldsymbol{\varphi}}, \tag{2.c.6}$$

where the linear transformation

$$\boldsymbol{T} = \mathbf{1} + \frac{1-\cos\vartheta}{\vartheta^2}\,\widetilde{\boldsymbol{\varphi}} + \frac{\vartheta-\sin\vartheta}{\vartheta^3}\,\widetilde{\boldsymbol{\varphi}}^2, \tag{2.c.7}$$

is called as the *tangent tensor*.

Angular acceleration is then calculated by differentiating the angular velocity (2.c.6) with respect to t,

$$\dot{\boldsymbol{\omega}} = \dot{\boldsymbol{T}}\cdot\dot{\boldsymbol{\varphi}} + \boldsymbol{T}\cdot\ddot{\boldsymbol{\varphi}}, \tag{2.c.8}$$

where $\dot{\boldsymbol{T}}$ is the time derivative of (2.c.7)

Also, analogous to (2.c.6), we obtain the **curvature** as a linear transformation of $\boldsymbol{\varphi}'$:

$$\boldsymbol{\kappa} = \boldsymbol{T}\cdot\boldsymbol{\varphi}'. \tag{2.c.9}$$

2.d Moment of inertia

The beam is homogeneous and isotropic with uniform mass density ρ_0 per unit volume, and the density per unit length is

$$\rho = \iint_{\mathcal{A}_c} \rho_0\, d\mathrm{x}_\alpha d\mathrm{x}_\beta, \tag{2.d.1a}$$

where $\mathcal{A}_c$ is the area of cross-section, while the greek indices $\alpha,\beta = 2,3$. As the centroidal axis coincides with the principal axis $\hat{\boldsymbol{e}}_1$ in the reference configuration, the distribution of area about the centroidal axis, i.e. the first moment of area, vanishes:

$$\iint_{\mathcal{A}_c} \mathrm{x}_\alpha\, d\mathrm{x}_\alpha d\mathrm{x}_\beta = 0, \tag{2.d.1b}$$

while the second moment of $\mathcal{A}_c$ is

$$I_{\alpha\beta} = \iint_{\mathcal{A}_c} x_\alpha x_\beta \, dx_\alpha dx_\beta = \begin{cases} 0, & \alpha \neq \beta \\ I_\alpha, & \alpha = \beta \end{cases} . \tag{2.d.1c}$$

Therefore, the **area moment of inertia** tensor is diagonal:

$$\boldsymbol{I} = \iint_{\mathcal{A}_c} (\mathbf{x}_{cp} \cdot \mathbf{x}_{cp})\mathbf{1} - \mathbf{x}_{cp} \otimes \mathbf{x}_{cp} \, dx_\alpha dx_\beta = \sum_{i=1}^{3} I_i \, \hat{\boldsymbol{e}}_i \otimes \hat{\boldsymbol{e}}_i, \tag{2.d.1d}$$

where $\mathbf{1} = \hat{\boldsymbol{e}}_i \otimes \hat{\boldsymbol{e}}_i$ is the identity tensor, while the components I_2 and I_3 are the principal moment of inertia about $\hat{\boldsymbol{e}}_2$ and $\hat{\boldsymbol{e}}_3$ axes, respectively, and $I_1 = I_2 + I_3$ is the polar moment of inertia about the centroidal axis $\hat{\boldsymbol{e}}_1$.

Mass moment of inertia per unit length

$$\boldsymbol{J} = \iint_{\mathcal{A}_c} (\mathbf{x}_{cp} \cdot \mathbf{x}_{cp})\mathbf{1} - \mathbf{x}_{cp} \otimes \mathbf{x}_{cp} \, \rho_0 dx_\alpha dx_\beta = \sum_{i=1}^{3} J_i \, \hat{\boldsymbol{e}}_i \otimes \hat{\boldsymbol{e}}_i, \text{ where } J_i = \rho I_i. \tag{2.d.1e}$$

The spatial mass moment of inertia tensor $\boldsymbol{\mathcal{J}}$ (per unit arc-length) can be obtained by a push-forward transformation:

$$\boldsymbol{\mathcal{J}} = \boldsymbol{R} \cdot \boldsymbol{J} \cdot \boldsymbol{R}^{\mathsf{T}} = \sum_{i=1}^{3} J_i \, \hat{\boldsymbol{d}}_i \otimes \hat{\boldsymbol{d}}_i. \tag{2.d.1f}$$

The rate of change of spatial inertia tensor (2.d.1f) with respect to time is given by

$$\dot{\boldsymbol{\mathcal{J}}} = \dot{\boldsymbol{R}} \cdot \boldsymbol{J} \cdot \boldsymbol{R}^{\mathsf{T}} + \boldsymbol{R} \cdot \boldsymbol{J} \cdot \dot{\boldsymbol{R}}^{\mathsf{T}} = \widetilde{\boldsymbol{\omega}} \cdot \boldsymbol{\mathcal{J}} - \boldsymbol{\mathcal{J}} \cdot \widetilde{\boldsymbol{\omega}}, \tag{2.d.1g}$$

where $\dot{\boldsymbol{R}} \cdot \boldsymbol{R}^{\mathsf{T}} = \widetilde{\boldsymbol{\omega}}$ was defined in (2.1.8b).

2.e Energetics

The total energy of the GE beam

$$w_{TOT} = w_S + w_G + w_K, \tag{2.e.1}$$

where w_S is the strain energy density, which was given by (2.4.1):

$$w_S(\boldsymbol{\gamma}, \boldsymbol{\kappa}) = \frac{1}{2} \left(\boldsymbol{\gamma} \cdot \boldsymbol{n} + \boldsymbol{\kappa} \cdot \boldsymbol{m} \right), \tag{2.e.2}$$

while w_G is the gravitational potential per unit length, which is defined as

$$w_G := \rho \boldsymbol{g} \cdot \boldsymbol{x}_c, \tag{2.e.3}$$

where $\boldsymbol{g} = g\hat{\boldsymbol{e}}_1$ is the acceleration due to gravity.

The kinetic energy density (per unit length) w_κ of the beam

$$\mathrm{w}_\kappa := \frac{1}{2}\sum_{\alpha=2}^{3}\sum_{\beta=2}^{3}\iint_{\mathcal{A}_c} \dot{\boldsymbol{x}}\cdot\dot{\boldsymbol{x}}\,\rho_0 d\mathrm{x}_\alpha d\mathrm{x}_\beta, \tag{2.e.4a}$$

where, from (2.1.9), we obtain

$$\begin{aligned}\dot{\boldsymbol{x}}\cdot\dot{\boldsymbol{x}} &= \dot{\boldsymbol{x}}_c\cdot\dot{\boldsymbol{x}}_c + 2\dot{\boldsymbol{x}}_c\cdot(\boldsymbol{\omega}\times\boldsymbol{x}_{cp}) + (\boldsymbol{\omega}\times\boldsymbol{x}_{cp})\cdot(\boldsymbol{\omega}\times\boldsymbol{x}_{cp}),\\ &= \dot{\boldsymbol{x}}_c\cdot\dot{\boldsymbol{x}}_c + 2(\dot{\boldsymbol{x}}_c\times\boldsymbol{\omega})\cdot\boldsymbol{x}_{cp} + \boldsymbol{\omega}\cdot\left[(\boldsymbol{x}_{cp}\cdot\boldsymbol{x}_{cp})\mathbf{1} - \boldsymbol{x}_{cp}\otimes\boldsymbol{x}_{cp}\right]\cdot\boldsymbol{\omega}.\end{aligned}$$

Finally, using (2.d.1b) and (2.d.1f), we can rewrite the kinetic energy density (2.e.4a) as

$$\begin{aligned}\mathrm{w}_\kappa &= \frac{1}{2}\sum_{\alpha=2}^{3}\sum_{\beta=2}^{3}\left\{\dot{\boldsymbol{x}}_c\cdot\dot{\boldsymbol{x}}_c\iint_{\mathcal{A}_c}\rho_0 d\mathrm{x}_\alpha d\mathrm{x}_\beta + 2(\dot{\boldsymbol{x}}_c\times\boldsymbol{\omega})\cdot\iint_{\mathcal{A}_c}\boldsymbol{x}_{cp}\,\rho_0\,d\mathrm{x}_\alpha d\mathrm{x}_\beta\right.\\ &\qquad\left.+\,\boldsymbol{\omega}\cdot\iint_{\mathcal{A}_c}\left\{(\boldsymbol{x}_{cp}\cdot\boldsymbol{x}_{cp})\mathbf{1} - \boldsymbol{x}_{cp}\otimes\boldsymbol{x}_{cp}\right\}\rho_0 d\mathrm{x}_\alpha d\mathrm{x}_\beta\cdot\boldsymbol{\omega}\right\}\\ &= \frac{\rho}{2}(\dot{\boldsymbol{u}}_0+\dot{\boldsymbol{u}})\cdot(\dot{\boldsymbol{u}}_0+\dot{\boldsymbol{u}}) + \frac{1}{2}\,\boldsymbol{\omega}\cdot\boldsymbol{\mathcal{J}}\cdot\boldsymbol{\omega},\end{aligned} \tag{2.e.4b}$$

where $\dot{\boldsymbol{x}}_c = \dot{\boldsymbol{u}}_0 + \dot{\boldsymbol{u}}$ is obtained by differentiating (2.1.4b).

Chapter 3

Mathematical Model of Underslung Load

As discussed in Chapter 1, the underslung load, which is being towed by the cable, is a large, rigid, ring-shaped structure that is firmly connected to the cable by rigid rods. In this chapter, we model the underslung load as a three dimensional (3D) rigid body with six degrees of freedom [Greenwood, 1988]. Further, we derive the exact equations of the aerodynamic load acting on the underslung load due to the wind/cross-flow. In literature [Cox, 1996; Thaokar et al., 2007], the exact hydrodynamic drag for a ring or torus are obtained only in the case of axisymmetric and very low Reynolds number (≤ 1) flows. However, we typically encouter winds/cross-flows of Reynolds number in the range of 3000 to about 30000 during towing operations. Therefore, we rely on the equations of drag on cylinder [Hoerner, 1992; Païdoussis et al., 2010], and calculate the total drag by approximating the ring by a large number of small rigidly connected cylinders. Lastly, we discuss how equations governing the underslung load enter as natural boundary conditions for the governing equations of the towing cable. We begin with the governing equations of the underslung load.

3.1 Equations for the underslung load

The underslung load shown in Fig. 3.1 is modeled as a 3D rigid body, which is a ring-shaped structure of mass m^* connected to the cable by massless rigid rods. The moment of inertia of the underslung load is then approximately that of a torus[1] with a mean radius r^* and cross-sectional radius r^*_{cs}:

$$[\boldsymbol{J}^*] = m^* \begin{bmatrix} r^{*2} + \frac{3}{4} r^{*2}_{cs} & 0 & 0 \\ 0 & \frac{1}{2} r^{*2} + \frac{5}{8} r^{*2}_{cs} & 0 \\ 0 & 0 & \frac{1}{2} r^{*2} + \frac{5}{8} r^{*2}_{cs} \end{bmatrix}.$$

[1] *http://mathworld.wolfram.com/Torus.html*

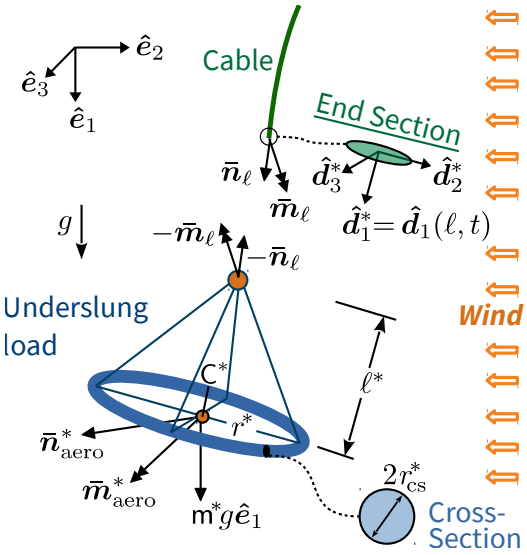

Figure 3.1: *Free body diagram of the underslung load which is connected to the end-section of the cable.*

The underslung load is rigidly fixed to the end-section of the cable at $s = \ell$. The equations of motion of the underslung load written about its center of mass C* are

$$-\bar{\boldsymbol{n}}_\ell + m^* \boldsymbol{g} + \bar{\boldsymbol{n}}^*_{\text{aero}} = m^* \ddot{\boldsymbol{u}}^* \tag{3.1.1a}$$

and

$$-\bar{\boldsymbol{m}}_\ell - \boldsymbol{\ell}^* \times \bar{\boldsymbol{n}}_\ell + \bar{\boldsymbol{m}}^*_{\text{aero}} = \boldsymbol{\mathcal{J}}^* \cdot \dot{\boldsymbol{\omega}}^* + \boldsymbol{\omega}^* \times \boldsymbol{\mathcal{J}}^* \cdot \boldsymbol{\omega}^*, \tag{3.1.1b}$$

where $\boldsymbol{g} = g\hat{\boldsymbol{e}}_1$ and we have

$$\boldsymbol{\ell}^* = \ell^* \hat{\boldsymbol{d}}_1^*, \quad \hat{\boldsymbol{d}}_i^*(t) = \hat{\boldsymbol{d}}_i(\ell, t), \text{ for } i = 1, 2, 3; \quad \boldsymbol{\omega}^*(t) = \boldsymbol{\omega}(\ell, t), \quad \dot{\boldsymbol{\omega}}^*(t) = \dot{\boldsymbol{\omega}}(\ell, t),$$
$$\boldsymbol{\mathcal{J}}^*(t) = \boldsymbol{R}^*(t) \cdot \boldsymbol{J}^* \cdot \boldsymbol{R}^{*\mathsf{T}}(t), \quad \boldsymbol{R}^*(t) = \boldsymbol{R}(\ell, t), \quad \dot{\boldsymbol{u}}^*(t) = \dot{\boldsymbol{u}}_0(t) + \dot{\boldsymbol{u}}(\ell, t) + \boldsymbol{\omega}^*(t) \times \boldsymbol{\ell}^*(t),$$
$$\text{and} \quad \ddot{\boldsymbol{u}}^*(t) = \ddot{\boldsymbol{u}}_0(t) + \ddot{\boldsymbol{u}}(\ell, t) + \boldsymbol{\omega}^*(t) \times \{\boldsymbol{\omega}^*(t) \times \boldsymbol{\ell}^*(t)\} + \dot{\boldsymbol{\omega}}^*(t) \times \boldsymbol{\ell}^*(t), \tag{3.1.2}$$

$-\bar{\boldsymbol{n}}_\ell$ and $-\bar{\boldsymbol{m}}_\ell$ are, respectively, the force and moment on the underslung load by the towing cable at the point of attachment, as shown in Fig. 3.1, while the aerodynamic force $\bar{\boldsymbol{n}}^*_{\text{aero}}$ and moment $\bar{\boldsymbol{m}}^*_{\text{aero}}$ on the underslung load are computed in the next section.

3.2 Aerodynamic force on the underslung load

We consider the aerodynamic force acting on the ring only, while the aerodynamic force on the massless and slender connecting rods is ignored because it is small compared to the aerodynamic forces on the ring.

To calculate the drag on the ring, we assume that the rigid circular ring is comprised of many cylinders of length $r^* d\theta$, where θ is measured from the $\hat{\boldsymbol{d}}_2^*$ axis, and the cross-sectional radius r^*_{cs} in 3D cross-flow (wind) as shown in Fig. 3.2. The tangent, bi-normal and normal unit vectors

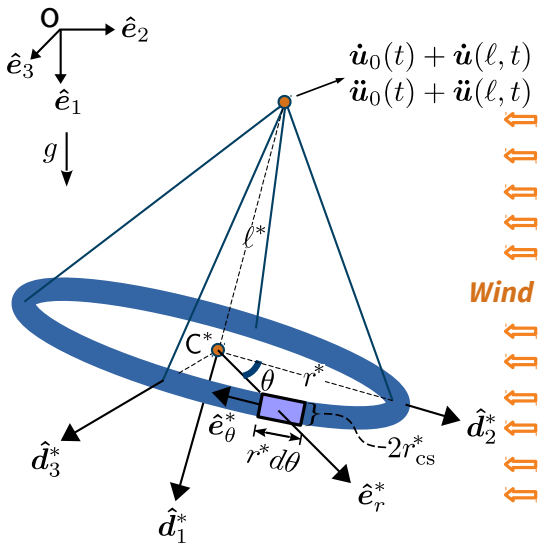

Figure 3.2: *Schematic of the underslung load in 3D cross-flow.*

local to each cylindrical element are, respectively,

$$\hat{\boldsymbol{e}}^*_t(\theta,t) = \begin{cases} -\hat{\boldsymbol{e}}^*_\theta & \text{if } \boldsymbol{v}^* \cdot \hat{\boldsymbol{e}}^*_\theta < 0 \\ \hat{\boldsymbol{e}}^*_\theta & \text{if } \boldsymbol{v}^* \cdot \hat{\boldsymbol{e}}^*_\theta \geq 0 \end{cases}, \quad \hat{\boldsymbol{e}}^*_b(\theta,t) = \frac{\hat{\boldsymbol{e}}_t \times \boldsymbol{v}^*}{|\hat{\boldsymbol{e}}_t \times \boldsymbol{v}^*|} \text{ and } \hat{\boldsymbol{e}}^*_n(\theta,t) = \hat{\boldsymbol{e}}^*_b \times \hat{\boldsymbol{e}}^*_t, \tag{3.2.1}$$

which are functions of the relative velocity of the element,

$$\boldsymbol{v}^*(\theta,t) = \boldsymbol{v}_{\text{air}} - \dot{\boldsymbol{u}}^* - \boldsymbol{\omega}^* \times \boldsymbol{r}^*, \tag{3.2.2}$$

where the radial vector $\boldsymbol{r}^* = r^* \hat{\boldsymbol{e}}^*_r$, while

$$\hat{\boldsymbol{e}}^*_\theta = \cos\theta\, \hat{\boldsymbol{d}}^*_3 - \sin\theta\, \hat{\boldsymbol{d}}^*_2, \text{ and } \hat{\boldsymbol{e}}^*_r = \cos\theta\, \hat{\boldsymbol{d}}^*_2 + \sin\theta\, \hat{\boldsymbol{d}}^*_3. \tag{3.2.3}$$

The aerodynamic force on a cylindrical element is

$$\bar{\boldsymbol{n}}^{*\text{cyl}}_{\text{aero}}(\theta,t) = \mathrm{c}_t \rho_{\text{air}} \pi r^*_{\text{cs}} \left(\boldsymbol{v}^* \cdot \hat{\boldsymbol{e}}^*_t\right)^2 \hat{\boldsymbol{e}}^*_t + \mathrm{c}_n \rho_{\text{air}} r^*_{\text{cs}} \left(\boldsymbol{v}^* \cdot \hat{\boldsymbol{e}}^*_n\right)^2 \hat{\boldsymbol{e}}^*_n, \tag{3.2.4}$$

where the first term (along $\hat{\boldsymbol{e}}^*_t$) is tangential/skin-friction drag and the second term (along $\hat{\boldsymbol{e}}^*_n$) is the normal/pressure drag on the cylindrical element. Note that, in contrast to the drag model on the cable (Sec. 2.6.2), we assume that there is no oscillating von Karman force on the ring because the wake-cutters present on the circumference of the ring wipe out any vortices formed after the flow separates.

Similarly, the aerodynamic moment on the element is

$$\bar{\boldsymbol{m}}^{*\text{cyl}}_{\text{aero}}(\theta,t) = \boldsymbol{r}^* \times \bar{\boldsymbol{n}}^{*\text{cyl}}_{\text{aero}}. \tag{3.2.5}$$

The total aerodynamic force and moment on the center of the ring are then computed by integrating the elemental quantities over the ring's circumference,

$$\bar{\boldsymbol{n}}^*_{\text{aero}}(t) = \int_0^{2\pi} \bar{\boldsymbol{n}}^{*\text{cyl}}_{\text{aero}}(\theta, t)\; r^* d\theta \tag{3.2.6a}$$

and

$$\bar{\boldsymbol{m}}^*_{\text{aero}}(t) = \int_0^{2\pi} \bar{\boldsymbol{m}}^{*\text{cyl}}_{\text{aero}}(\theta, t)\; r^* d\theta. \tag{3.2.6b}$$

Finally, we discuss how the underslung load equations are the natural boundary conditions for the equations of the towing cable.

3.3 Natural boundary condition to towing cable's equations

As discussed in Sec. 2.7, the reaction force $\bar{\boldsymbol{n}}_\ell$ and reaction moment $\bar{\boldsymbol{m}}_\ell$ from the underslung load to the cable, and vice versa, are communicated via the point of attachment; see Fig. 3.1. These force and moments actually couple the dynamics of the towing cable and the underslung load, while holding them together. The governing equation (3.1.1) of the underslung load become the natural boundary conditions to the governing equations (2.2.7) of the towing cable at the tail-end ($s = \ell$). Alternatively, $\bar{\boldsymbol{n}}_\ell$ and $\bar{\boldsymbol{m}}_\ell$ are impedance force and moment from the underslung load to the towing cable. Accordingly, we set (3.1.1) in the form of an external force vector (Sec. 2.7) or impedance to the towing cable's tail-end ($s = \ell$),

$$\mathtt{f}_\ell = \begin{bmatrix} \bar{\boldsymbol{n}}_\ell \\ \bar{\boldsymbol{m}}_\ell \end{bmatrix} = -\mathtt{f}^*_{\text{iner}} + \mathtt{f}^*_{\text{grav}} + \mathtt{f}^*_{\text{aero}}, \tag{3.3.1a}$$

where

$$\mathtt{f}^*_{\text{iner}} = \begin{bmatrix} \mathsf{m}^* \ddot{\boldsymbol{u}}^* \\ \boldsymbol{\mathcal{J}}^* \cdot \dot{\boldsymbol{\omega}}^* + \boldsymbol{\omega}^* \times \boldsymbol{\mathcal{J}}^* \cdot \boldsymbol{\omega}^* + \boldsymbol{\ell}^* \times \mathsf{m}^* \ddot{\boldsymbol{u}}^* \end{bmatrix} \tag{3.3.1b}$$

$$\mathtt{f}^*_{\text{grav}} = \begin{bmatrix} \mathsf{m}^* \boldsymbol{g} \\ \boldsymbol{\ell}^* \times \mathsf{m}^* \boldsymbol{g} \end{bmatrix} \tag{3.3.1c}$$

and

$$\mathtt{f}^*_{\text{aero}} = \int_0^{2\pi} \begin{bmatrix} \bar{\boldsymbol{n}}^{*\text{cyl}}_{\text{aero}}(\theta, t) \\ (\boldsymbol{r}^* + \boldsymbol{\ell}^*) \times \bar{\boldsymbol{n}}^{*\text{cyl}}_{\text{aero}}(\theta, t) \end{bmatrix} r^* d\theta. \tag{3.3.1d}$$

Chapter 4

Nonlinear finite element formulation

The cable's coupled differential equations (2.2.7) or their integral/weak form (2.5.1a) are nonlinear in the displacement measures $\boldsymbol{u}(s,t)$ and $\boldsymbol{\varphi}(s,t)$. To solve them computationally using the nonlinear finite element (FE) method [Bathe, 2006; Ibrahimbegović, 1995; Simo & Vu-Quoc, 1986b], we linearize the weak form (2.5.1a) about the base configuration. After linearization, we will solve the same nonlinear equations of the cable for the increments $\Delta\boldsymbol{u}(s,t)$ and $\Delta\boldsymbol{\varphi}(s,t)$ in the displacement measures $\boldsymbol{u}(s,t)$ and $\boldsymbol{\varphi}(s,t)$, respectively.

4.1 Linearized weak form of the cable's governing equations

The linearization of (2.5.1a) about base configuration, which is defined by the column vector $\mathtt{q}(s,t) := [\boldsymbol{u}(s,t)\ \boldsymbol{\varphi}(s,t)]^{\mathsf{T}}$, is:

$$\mathrm{w}(\mathtt{q},\dot{\mathtt{q}},\ddot{\mathtt{q}}) + \Delta\mathrm{w}_{\mathrm{iner}} + \Delta\mathrm{w}_{\mathrm{int}} - \Delta\mathrm{w}_{\mathrm{ext}} - \Delta\mathrm{w}_{\mathrm{bc}} = 0, \tag{4.1.1}$$

where
$$\Delta\mathrm{w}_{\mathrm{iner}} = \int_0^\ell \eta^{\mathsf{T}}\Delta\mathtt{f}_{\mathrm{iner}}\,ds, \quad \Delta\mathrm{w}_{\mathrm{int}} = \int_0^\ell \eta'^{\mathsf{T}}\Delta\mathtt{f}^{\mathrm{I}}_{\mathrm{int}} + \eta^{\mathsf{T}}\Delta\mathtt{f}^{\mathrm{II}}_{\mathrm{int}}\,ds,$$

$$\Delta\mathrm{w}_{\mathrm{ext}} = \int_0^\ell \eta^{\mathsf{T}}\Delta\mathtt{f}_{\mathrm{ext}}\,ds \quad \text{and} \quad \Delta\mathrm{w}_{\mathrm{bc}} = \eta^{\mathsf{T}}(\ell)\Delta\mathtt{f}^{*}_{\ell}(\ell,t).$$

The incremental force vectors $\Delta\mathtt{f}_{\mathrm{iner}}$, $\Delta\mathtt{f}^{\mathrm{I}}_{\mathrm{int}}$, $\Delta\mathtt{f}^{\mathrm{II}}_{\mathrm{int}}$ and $\Delta\mathtt{f}_{\mathrm{ext}}$ are derived in Sec. 4.4, followed by the increment of the boundary condition (reaction) force vector $\Delta\mathtt{f}^{*}_{\ell}(\ell,t)$ exerted by the slung load on the cable in Sec. 4.5, and finally the finite element formulation in Sec. 4.6.

However, before that, we derive the incremental forms of kinematic quantities (Sec.4.2) and strain measures (Sec.4.3) that are essential in the derivation of the incremental forces.

4.2 Incremental angular velocity and angular acceleration

We saw in (2.c.6) that the angular velocity $\boldsymbol{\omega}$ is a function on $\boldsymbol{\varphi}$ and $\dot{\boldsymbol{\varphi}}$. Linearizing $\boldsymbol{\omega}$ and using (4.a.1), we obtain

$$\Delta\boldsymbol{\omega} = \frac{\partial\boldsymbol{\omega}}{\partial\boldsymbol{\varphi}}\cdot\Delta\boldsymbol{\varphi} + \frac{\partial\boldsymbol{\omega}}{\partial\dot{\boldsymbol{\varphi}}}\cdot\Delta\dot{\boldsymbol{\varphi}}, = \left(\dot{\boldsymbol{T}} - \widetilde{\boldsymbol{\omega}}\cdot\boldsymbol{T}\right)\cdot\Delta\boldsymbol{\varphi} + \boldsymbol{T}\cdot\Delta\dot{\boldsymbol{\varphi}}. \tag{4.2.1}$$

The derivative of (4.2.1),

$$\Delta\dot{\boldsymbol{\omega}} = \left(\ddot{\boldsymbol{T}} - \dot{\widetilde{\boldsymbol{\omega}}}\cdot\boldsymbol{T} - \widetilde{\boldsymbol{\omega}}\cdot\dot{\boldsymbol{T}}\right)\cdot\Delta\boldsymbol{\varphi} + \left(2\dot{\boldsymbol{T}} - \widetilde{\boldsymbol{\omega}}\cdot\boldsymbol{T}\right)\cdot\Delta\dot{\boldsymbol{\varphi}} + \boldsymbol{T}\cdot\Delta\ddot{\boldsymbol{\varphi}}. \tag{4.2.2}$$

4.3 Incremental curvature and strain

Analogous to (4.2.1) and utilizing (2.3.4), the increment in the axial vector $\boldsymbol{\kappa}$ of the curvature tensor is given by

$$\Delta\boldsymbol{\kappa} = \left(\boldsymbol{T}' - \widetilde{\boldsymbol{\kappa}}\cdot\boldsymbol{T}\right)\cdot\Delta\boldsymbol{\varphi} + \boldsymbol{T}\cdot\Delta\boldsymbol{\varphi}'. \tag{4.3.1}$$

The increment of the strain is obtained from (2.3.6):

$$\Delta\boldsymbol{\gamma} = \Delta\boldsymbol{x}_c' - \Delta\hat{\boldsymbol{d}}_1 = \Delta\boldsymbol{u}' - \widetilde{(\boldsymbol{T}\cdot\Delta\boldsymbol{\varphi})}\cdot\hat{\boldsymbol{d}}_1, \tag{4.3.2}$$

where the director $\hat{\boldsymbol{d}}_1$'s increment $\Delta\hat{\boldsymbol{d}}_1 = \widetilde{(\boldsymbol{T}\cdot\Delta\boldsymbol{\varphi})}\cdot\hat{\boldsymbol{d}}_1$ is found by using its derivative (2.3.3) and utilizing (2.3.4).

4.4 Incremental force vectors

Using the incremental forms of angular velocity (4.2.1), angular acceleration (4.2.2), and the strain measures (4.3.1) and (4.3.2), we now calculate the incremental force vectors.

4.4.1 Incremental inertial force vector $\Delta\mathtt{f}_{iner}$

The increment of the inertial force vector (2.5.1g),

$$\Delta\mathtt{f}_{\text{iner}} = \begin{bmatrix}\rho\Delta\ddot{\boldsymbol{u}}\\ \Delta\dot{\boldsymbol{h}}\end{bmatrix},$$

where the increment of the angular momentum rate is found from (2.2.5),

$$\Delta\dot{\boldsymbol{h}} = (\Delta\boldsymbol{\mathcal{J}})\cdot\dot{\boldsymbol{\omega}} + \boldsymbol{\mathcal{J}}\cdot\Delta\dot{\boldsymbol{\omega}} - \widetilde{\boldsymbol{h}}\cdot\Delta\boldsymbol{\omega} + \widetilde{\boldsymbol{\omega}}\cdot(\Delta\boldsymbol{\mathcal{J}})\cdot\boldsymbol{\omega} + \widetilde{\boldsymbol{\omega}}\cdot\boldsymbol{\mathcal{J}}\cdot\Delta\boldsymbol{\omega},$$

where we obtain

$$(\Delta\boldsymbol{\mathcal{J}})\cdot\boldsymbol{\omega} = (\boldsymbol{\mathcal{J}}\cdot\widetilde{\boldsymbol{\omega}} - \widetilde{\boldsymbol{h}})\cdot\boldsymbol{T}\cdot\Delta\boldsymbol{\varphi} \quad\text{and}\quad (\Delta\boldsymbol{\mathcal{J}})\cdot\dot{\boldsymbol{\omega}} = (\boldsymbol{\mathcal{J}}\cdot\dot{\widetilde{\boldsymbol{\omega}}} - \widetilde{\boldsymbol{\mathcal{J}}\cdot\dot{\boldsymbol{\omega}}})\cdot\boldsymbol{T}\cdot\Delta\boldsymbol{\varphi},$$

from (4.b.1d) and (4.b.1e), respectively, while $\Delta\boldsymbol{\omega}$ is given by (4.2.1), and $\Delta\dot{\boldsymbol{\omega}}$ is given by (4.2.2). Therefore,

$$\Delta \mathtt{f}_{\text{iner}} = \mathtt{M}\Delta\ddot{\mathtt{q}} + \mathtt{G}\Delta\dot{\mathtt{q}} + \mathtt{K}_{\text{iner}}\Delta\mathtt{q}, \tag{4.4.1a}$$

where $\Delta\mathtt{q}^{\mathsf{T}} = [\Delta\boldsymbol{u}\ \Delta\boldsymbol{\varphi}]$, $\Delta\dot{\mathtt{q}}^{\mathsf{T}} = [\Delta\dot{\boldsymbol{u}}\ \Delta\dot{\boldsymbol{\varphi}}]$ and $\Delta\ddot{\mathtt{q}}^{\mathsf{T}} = [\Delta\ddot{\boldsymbol{u}}\ \Delta\ddot{\boldsymbol{\varphi}}]$ are the increments in the state vectors $\mathtt{q}$, $\dot{\mathtt{q}}$ and $\ddot{\mathtt{q}}$, respectively, while

$$\mathtt{M} = \begin{bmatrix} \rho\mathbf{1} & \mathbf{O} \\ \mathbf{O} & \boldsymbol{\mathcal{J}}\cdot\boldsymbol{T} \end{bmatrix}, \quad \mathtt{G} = \begin{bmatrix} \mathbf{O} & \mathbf{O} \\ \mathbf{O} & 2\boldsymbol{\mathcal{J}}\cdot\dot{\boldsymbol{T}} + \dot{\boldsymbol{\mathcal{J}}}\cdot\boldsymbol{T} - \widetilde{\boldsymbol{h}}\cdot\boldsymbol{T} \end{bmatrix}, \tag{4.4.1b}$$

and $$\mathtt{K}_{\text{iner}} = \begin{bmatrix} \mathbf{O} & \mathbf{O} \\ \mathbf{O} & \boldsymbol{\mathcal{J}}\cdot\ddot{\boldsymbol{T}} + \dot{\boldsymbol{\mathcal{J}}}\cdot\dot{\boldsymbol{T}} - \widetilde{\boldsymbol{h}}\cdot\dot{\boldsymbol{T}} - \dot{\widetilde{\boldsymbol{h}}}\cdot\boldsymbol{T} \end{bmatrix},$$

are called the mass matrix, the gyroscopic matrix and the inertial tangent stiffness matrix, respectively, where $\mathbf{O}$ is the zero tensor, $\widetilde{\boldsymbol{h}} = \mathrm{sk}(\boldsymbol{h})$ and $\dot{\widetilde{\boldsymbol{h}}} = \mathrm{sk}(\dot{\boldsymbol{h}})$.

4.4.2 Incremental internal force vectors $\Delta\mathtt{f}^{I}_{int}$ and $\Delta\mathtt{f}^{II}_{int}$

The increment of the first internal force (2.5.1g) is

$$\Delta\mathtt{f}^{\mathrm{I}}_{\text{int}} = \begin{bmatrix} \Delta\boldsymbol{n} \\ \Delta\boldsymbol{m} \end{bmatrix} = \begin{bmatrix} (\Delta\boldsymbol{\mathcal{C}}_{\boldsymbol{n}})\cdot\boldsymbol{\gamma} \\ (\Delta\boldsymbol{\mathcal{C}}_{\boldsymbol{m}})\cdot\boldsymbol{\kappa} \end{bmatrix} + \begin{bmatrix} \boldsymbol{\mathcal{C}}_{\boldsymbol{n}}\cdot(\Delta\boldsymbol{\gamma}) \\ \boldsymbol{\mathcal{C}}_{\boldsymbol{m}}\cdot(\Delta\boldsymbol{\kappa}) \end{bmatrix},$$

where the incremental strain $\Delta\boldsymbol{\gamma}$ and incremental curvature $\Delta\boldsymbol{\kappa}$ are given by (4.3.2) and (4.3.1), respectively, while the increments in the elasticity tensors

$$(\Delta\boldsymbol{\mathcal{C}}_{\boldsymbol{n}})\cdot\boldsymbol{\gamma} = (\boldsymbol{\mathcal{C}}_{\boldsymbol{n}}\cdot\widetilde{\boldsymbol{\gamma}} - \widetilde{\boldsymbol{n}})\cdot\boldsymbol{T}\cdot\Delta\boldsymbol{\varphi} \ \text{ and } \ (\Delta\boldsymbol{\mathcal{C}}_{\boldsymbol{m}})\cdot\boldsymbol{\kappa} = (\boldsymbol{\mathcal{C}}_{\boldsymbol{m}}\cdot\widetilde{\boldsymbol{\kappa}} - \widetilde{\boldsymbol{m}})\cdot\boldsymbol{T}\cdot\Delta\boldsymbol{\varphi},$$

are given in Appendix 4.b.1. Therefore,

$$\Delta\mathtt{f}^{\mathrm{I}}_{\text{int}} = \mathtt{K}^{\mathrm{I}}_{\mathtt{q}}\Delta\mathtt{q} + \mathtt{K}^{\mathrm{I}}_{\mathtt{q}'}\Delta\mathtt{q}', \tag{4.4.2a}$$

where $\Delta\mathtt{q}^{\mathsf{T}} = [\Delta\boldsymbol{u}\ \Delta\boldsymbol{\varphi}]$, $\Delta\mathtt{q}'^{\mathsf{T}} = [\Delta\boldsymbol{u}'\ \Delta\boldsymbol{\varphi}']$, while

$$\mathtt{K}^{\mathrm{I}}_{\mathtt{q}} = \begin{bmatrix} \mathbf{O} & (\boldsymbol{\mathcal{C}}_{\boldsymbol{n}}\cdot\widetilde{\boldsymbol{x}}'_{\mathrm{c}} - \widetilde{\boldsymbol{n}})\cdot\boldsymbol{T} \\ \mathbf{O} & \boldsymbol{\mathcal{C}}_{\boldsymbol{m}}\cdot\boldsymbol{T}' - \widetilde{\boldsymbol{m}}\cdot\boldsymbol{T} \end{bmatrix} \ \text{ and } \ \mathtt{K}^{\mathrm{I}}_{\mathtt{q}'} = \begin{bmatrix} \boldsymbol{\mathcal{C}}_{\boldsymbol{n}} & \mathbf{O} \\ \mathbf{O} & \boldsymbol{\mathcal{C}}_{\boldsymbol{m}}\cdot\boldsymbol{T} \end{bmatrix}, \tag{4.4.2b}$$

where $\mathbf{O}$ is three dimensional zero tensor.

Similarly, the increment of the second internal force vector (2.5.1g),

$$\Delta\mathtt{f}^{\mathrm{II}}_{\text{int}} = -\begin{bmatrix} \mathbf{0} \\ \Delta\widetilde{\boldsymbol{x}}'_{\mathrm{c}}\cdot\boldsymbol{n} + \widetilde{\boldsymbol{x}}'_{\mathrm{c}}\cdot\Delta\boldsymbol{n} \end{bmatrix} = \begin{bmatrix} \mathbf{O} & \mathbf{O} \\ \widetilde{\boldsymbol{n}} & \mathbf{O} \end{bmatrix}\begin{bmatrix} \Delta\boldsymbol{u}' \\ \Delta\boldsymbol{\varphi}' \end{bmatrix} - \begin{bmatrix} \mathbf{O} & \mathbf{O} \\ \widetilde{\boldsymbol{x}}'_{\mathrm{c}} & \mathbf{O} \end{bmatrix}\Delta\mathtt{f}^{\mathrm{I}}_{\text{int}}$$

$$= \mathtt{K}^{\mathrm{II}}_{\mathtt{q}}\Delta\mathtt{q} + \mathtt{K}^{\mathrm{II}}_{\mathtt{q}'}\Delta\mathtt{q}' \tag{4.4.3a}$$

where

$$\mathtt{K}^{\mathrm{II}}_{\mathtt{q}} = \begin{bmatrix} \mathbf{O} & \mathbf{O} \\ \mathbf{O} & \widetilde{\boldsymbol{x}}'_{\mathrm{c}} \cdot (\widetilde{\boldsymbol{n}} - \boldsymbol{\mathcal{C}}_{\boldsymbol{n}} \cdot \widetilde{\boldsymbol{x}}'_{\mathrm{c}}) \cdot \boldsymbol{T} \end{bmatrix} \quad \text{and} \quad \mathtt{K}^{\mathrm{II}}_{\mathtt{q}'} = \begin{bmatrix} \mathbf{O} & \mathbf{O} \\ \widetilde{\boldsymbol{n}} - \widetilde{\boldsymbol{x}}'_{\mathrm{c}} \cdot \boldsymbol{\mathcal{C}}_{\boldsymbol{n}} & \mathbf{O} \end{bmatrix}. \tag{4.4.3b}$$

4.4.3 Incremental external force vector $\Delta\mathtt{f}_{ext}$

The incremental form of the external force vector (Sec. 2.6) is

$$\Delta\mathtt{f}_{\mathrm{ext}} = \begin{bmatrix} \Delta\bar{\boldsymbol{n}} \\ \Delta\bar{\boldsymbol{m}} \end{bmatrix} = \Delta\mathtt{f}_{\mathrm{grav}} + \Delta\mathtt{f}_{\mathrm{aero}} = \Delta\mathtt{f}_{\mathrm{aero}}, \tag{4.4.4a}$$

where the incremental external gravitational force is *zero* because the direction and magnitude of the gravitational force remain unchanged, while the incremental aerodynamic force is calculated next.

The incremental aerodynamic force

$$\Delta\mathtt{f}_{\mathrm{aero}} = \begin{bmatrix} \Delta\bar{\boldsymbol{n}}^{\mathrm{cyl}}_{\mathrm{aero}} \\ \mathbf{0} \end{bmatrix} \tag{4.4.4b}$$

where the increment of (2.6.5) is

$$\begin{aligned} \Delta\bar{\boldsymbol{n}}^{\mathrm{cyl}}_{\mathrm{aero}} = {} & \mathrm{c}_t\rho_{\mathrm{air}}\pi r v_t \left(2\Delta v_t\hat{\boldsymbol{e}}_t + v_t\Delta\hat{\boldsymbol{e}}_t\right) + \mathrm{c}_n\rho_{\mathrm{air}} r v_n \left(2\Delta v_n\hat{\boldsymbol{e}}_n + v_n\Delta\hat{\boldsymbol{e}}_n\right) \\ & + \mathrm{c}_\kappa\rho_{\mathrm{air}} r \sin(\omega_\kappa t)\, v_n \left(2\Delta v_n\hat{\boldsymbol{e}}_b + v_n\Delta\hat{\boldsymbol{e}}_b\right), \end{aligned} \tag{4.4.4c}$$

while we compute the following quantities by linearizing (2.6.3), (2.1.4b) and (2.6.4):

$$\Delta v_t = \Delta\boldsymbol{v}\cdot\hat{\boldsymbol{e}}_t + \boldsymbol{v}\cdot\Delta\hat{\boldsymbol{e}}_t, \quad \Delta v_n = \Delta\boldsymbol{v}\cdot\hat{\boldsymbol{e}}_n + \boldsymbol{v}\cdot\Delta\hat{\boldsymbol{e}}_n, \quad \Delta\boldsymbol{v} = -\Delta\dot{\boldsymbol{u}},$$

$$\Delta\hat{\boldsymbol{e}}_t = \begin{cases} -\Delta\hat{\boldsymbol{x}}'_c & \text{if } \boldsymbol{v}\cdot\hat{\boldsymbol{x}}'_c < 0 \\ \Delta\hat{\boldsymbol{x}}'_c & \text{if } \boldsymbol{v}\cdot\hat{\boldsymbol{x}}'_c \geq 0 \end{cases}, \quad \Delta\hat{\boldsymbol{x}}'_c = \frac{|\boldsymbol{x}'_c|\Delta\boldsymbol{x}'_c - \boldsymbol{x}'_c\Delta|\boldsymbol{x}'_c|}{|\boldsymbol{x}'_c|^2},$$

$$\Delta\boldsymbol{x}'_c = \Delta\boldsymbol{u}', \quad \Delta|\boldsymbol{x}'_c| = \frac{\boldsymbol{x}'_c\cdot\Delta\boldsymbol{x}'_c}{|\boldsymbol{x}'_c|} = \hat{\boldsymbol{x}}'_c\cdot\Delta\boldsymbol{u}',$$

$$\Delta\hat{\boldsymbol{e}}_b = \Delta\frac{\hat{\boldsymbol{e}}_t\times\boldsymbol{v}}{|\hat{\boldsymbol{e}}_t\times\boldsymbol{v}|} = \frac{\left(\Delta\hat{\boldsymbol{e}}_t\times\boldsymbol{v} + \hat{\boldsymbol{e}}_t\times\Delta\boldsymbol{v}\right)|\hat{\boldsymbol{e}}_t\times\boldsymbol{v}| - (\hat{\boldsymbol{e}}_t\times\boldsymbol{v})\,\Delta|\hat{\boldsymbol{e}}_t\times\boldsymbol{v}|}{|\hat{\boldsymbol{e}}_t\times\boldsymbol{v}|^2},$$

$$\Delta|\hat{\boldsymbol{e}}_t\times\boldsymbol{v}| = \frac{(\hat{\boldsymbol{e}}_t\times\boldsymbol{v})\cdot\Delta\left(\hat{\boldsymbol{e}}_t\times\boldsymbol{v}\right)}{|\hat{\boldsymbol{e}}_t\times\boldsymbol{v}|} = \hat{\boldsymbol{e}}_{\mathrm{b}}\cdot\left(\Delta\hat{\boldsymbol{e}}_t\times\boldsymbol{v} + \hat{\boldsymbol{e}}_t\times\Delta\boldsymbol{v}\right),$$

and $$\Delta\hat{\boldsymbol{e}}_n = \Delta\left(\hat{\boldsymbol{e}}_b\times\hat{\boldsymbol{e}}_t\right) = \Delta\hat{\boldsymbol{e}}_b\times\hat{\boldsymbol{e}}_t + \hat{\boldsymbol{e}}_b\times\Delta\hat{\boldsymbol{e}}_t.$$

Simplifying the algebra, we obtain

$$\Delta\bar{\boldsymbol{n}}^{\mathrm{cyl}}_{\mathrm{aero}} = \boldsymbol{G}^{\mathrm{cyl}}_{\mathrm{aero}}\cdot\Delta\dot{\boldsymbol{u}} + \boldsymbol{K}^{\mathrm{cyl}}_{\mathrm{aero}}\cdot\Delta\boldsymbol{u}',$$

where

$$\boldsymbol{G}^{\text{cyl}}_{\text{aero}} = \mathsf{c}_n \rho_{\text{air}} r v_n \left(\widetilde{\hat{\boldsymbol{x}}}'_c - \hat{\boldsymbol{e}}_n \otimes \hat{\boldsymbol{e}}_b \right) \cdot \widetilde{\hat{\boldsymbol{x}}}'_c - 2\, \mathsf{c}_t \rho_{\text{air}} \pi r v_t \left(\hat{\boldsymbol{x}}'_c \otimes \hat{\boldsymbol{x}}'_c \right) - \mathsf{c}_\kappa \rho_{\text{air}} r \sin(\omega_\kappa t)\, v_n \left(\mathbf{1} + \hat{\boldsymbol{e}}_b \otimes \hat{\boldsymbol{e}}_b \right) \cdot \widetilde{\hat{\boldsymbol{x}}}'_c$$

and

$$\boldsymbol{K}^{\text{cyl}}_{\text{aero}} = \mathsf{c}_n \rho_{\text{air}} r v_n \left[(\hat{\boldsymbol{e}}_n \otimes \hat{\boldsymbol{e}}_b)\, \widetilde{\boldsymbol{v}} + \hat{\boldsymbol{x}}'_c \otimes \boldsymbol{v} + (\boldsymbol{v} \cdot \hat{\boldsymbol{x}}'_c)\mathbf{1} \right] \cdot \frac{\widetilde{\hat{\boldsymbol{x}}}'_c \cdot \widetilde{\hat{\boldsymbol{x}}}'_c}{|\boldsymbol{x}'_c|} - \mathsf{c}_t \rho_{\text{air}} \pi r v_t \left[2\, \hat{\boldsymbol{x}}'_c \otimes \boldsymbol{v} + (\boldsymbol{v} \cdot \hat{\boldsymbol{x}}'_c)\mathbf{1} \right] \cdot \frac{\widetilde{\hat{\boldsymbol{x}}}'_c \cdot \widetilde{\hat{\boldsymbol{x}}}'_c}{|\boldsymbol{x}'_c|} + \mathsf{c}_\kappa \rho_{\text{air}} r \rho_{\text{air}} r \sin(\omega_\kappa t)\, v_n \left(\mathbf{1} + \hat{\boldsymbol{e}}_b \otimes \hat{\boldsymbol{e}}_b \right) \cdot \widetilde{\boldsymbol{v}} \cdot \frac{\widetilde{\hat{\boldsymbol{x}}}'_c \cdot \widetilde{\hat{\boldsymbol{x}}}'_c}{|\boldsymbol{x}'_c|}.$$

Finally, the incremental external force vector

$$\Delta \mathtt{f}_{\text{ext}} = \Delta \mathtt{f}_{\text{aero}} = \mathtt{K}_{\text{aero}} \Delta \mathtt{q}' + \mathtt{G}_{\text{aero}} \Delta \dot{\mathtt{q}}, \tag{4.4.4d}$$

where the aerodynamic stiffness and damping matrices are, respectively,

$$\mathtt{K}_{\text{aero}} = \begin{bmatrix} \boldsymbol{K}^{\text{cyl}}_{\text{aero}} & \mathbf{O} \\ \mathbf{O} & \mathbf{O} \end{bmatrix} \quad \text{and} \quad \mathtt{G}_{\text{aero}} = \begin{bmatrix} \boldsymbol{G}^{\text{cyl}}_{\text{aero}} & \mathbf{O} \\ \mathbf{O} & \mathbf{O} \end{bmatrix}$$

4.5 Linearized form of slung-load's equations

The slung load's governing equations (3.1.1) appear as the natural boundary conditions to the cable's equations at $s = \ell$, given by (3.3.1). Being nonlinear in state vectors at $s = \ell$, they are linearized about the base state resulting in the following incremental form:

$$\Delta \mathtt{f}_\ell = -\Delta \mathtt{f}^*_{\text{iner}} + \Delta \mathtt{f}^*_{\text{grav}} + \Delta \mathtt{f}^*_{\text{aero}}, \tag{4.5.1a}$$

where

$$\Delta \mathtt{f}^*_{\text{iner}} = \begin{bmatrix} \mathsf{m}^* \Delta \ddot{\boldsymbol{u}}^* \\ \Delta \left(\boldsymbol{\mathcal{J}}^* \cdot \dot{\boldsymbol{\omega}}^* + \boldsymbol{\omega}^* \times \boldsymbol{\mathcal{J}}^* \cdot \boldsymbol{\omega}^* \right) + \Delta \left(\boldsymbol{\ell}^* \times \mathsf{m}^* \ddot{\boldsymbol{u}}^* \right) \end{bmatrix}, \tag{4.5.1b}$$

$$\Delta \mathtt{f}^*_{\text{grav}} = \begin{bmatrix} \mathbf{0} \\ \Delta \boldsymbol{\ell}^* \times \mathsf{m}^* \boldsymbol{g} \end{bmatrix} \tag{4.5.1c}$$

and

$$\Delta \mathtt{f}^*_{\text{aero}} = \int_0^{2\pi} \begin{bmatrix} \Delta \bar{\boldsymbol{n}}^{*\text{cyl}}_{\text{aero}}(\theta, t) \\ \Delta \left\{ (\boldsymbol{r}^* + \boldsymbol{\ell}^*) \times \bar{\boldsymbol{n}}^{*\text{cyl}}_{\text{aero}}(\theta, t) \right\} \end{bmatrix} r^* d\theta. \tag{4.5.1d}$$

The increments of the various quantities appearing above are now discussed.

The increments in velocity, angular velocity, angular acceleration are obtained using (3.1.2):

$$\Delta \boldsymbol{\omega}^* = \Delta \boldsymbol{\omega}(\ell, t),\ \Delta \dot{\boldsymbol{\omega}}^* = \Delta \dot{\boldsymbol{\omega}}(\ell, t),\ \Delta \ddot{\boldsymbol{u}}^* = \Delta \ddot{\boldsymbol{u}}(\ell, t) + \Delta \left(\boldsymbol{\omega}^* \times \boldsymbol{\ell}^* \right),\ \Delta \boldsymbol{\ell}^* = \ell^* \Delta \hat{\boldsymbol{d}}^*_1,$$

$$\Delta \boldsymbol{r}^* = r^* \Delta \hat{\boldsymbol{e}}_r^* \quad \text{and} \quad \Delta \ddot{\boldsymbol{u}}^* = \Delta \ddot{\boldsymbol{u}}(\ell, t) + \Delta \left[\boldsymbol{\omega}^* \times (\boldsymbol{\omega}^* \times \boldsymbol{\ell}^*) + \dot{\boldsymbol{\omega}}^* \times \boldsymbol{\ell}^* \right],$$

where $\Delta\boldsymbol{\omega}(\ell, t)$ and $\Delta\dot{\boldsymbol{\omega}}(\ell, t)$ are, respectively, the quantities (4.2.1) and (4.2.2) evaluated at the boundary $s = \ell$ while, as noted in Sec. 4.3, the directors' increments

$$\Delta \hat{\boldsymbol{d}}_i^* = (\widetilde{\boldsymbol{T}^* \cdot \Delta \boldsymbol{\varphi}^*}) \cdot \hat{\boldsymbol{d}}_i^*, \quad \text{where} \quad \boldsymbol{\varphi}^* = \boldsymbol{\varphi}(\ell, t) \quad \text{and} \quad \boldsymbol{T}^* = \boldsymbol{T}(\boldsymbol{\varphi}^*).$$

The increment in the drag force (3.2.4) acting on a cylindrical element of the ring is

$$\begin{aligned} \Delta \bar{\boldsymbol{n}}_{\text{aero}}^{*\text{cyl}}(\theta, t) = {} & c_t \rho_{\text{air}} \pi r_{\text{cs}}^* \left(\boldsymbol{v}^* \cdot \hat{\boldsymbol{e}}_t^* \right) \left\{ 2\Delta \left(\boldsymbol{v}^* \cdot \hat{\boldsymbol{e}}_t^* \right) \hat{\boldsymbol{e}}_t^* + \left(\boldsymbol{v}^* \cdot \hat{\boldsymbol{e}}_t^* \right) \Delta \hat{\boldsymbol{e}}_t^* \right\} \\ & + c_n \rho_{\text{air}} r_{\text{cs}}^* \left(\boldsymbol{v}^* \cdot \hat{\boldsymbol{e}}_n^* \right) \left\{ 2\Delta \left(\boldsymbol{v}^* \cdot \hat{\boldsymbol{e}}_n^* \right) \hat{\boldsymbol{e}}_n^* + \left(\boldsymbol{v}^* \cdot \hat{\boldsymbol{e}}_n^* \right) \Delta \hat{\boldsymbol{e}}_n^* \right\}, \end{aligned} \tag{4.5.2}$$

where, from (3.2.1), (3.2.2), and (3.2.3), we compute

$$\begin{aligned} \Delta \boldsymbol{v}^* &= -\Delta \dot{\boldsymbol{u}}^* - \Delta \left(\boldsymbol{\omega}^* \times \boldsymbol{r}^* \right), \\ \Delta \hat{\boldsymbol{e}}_r^* &= \cos\theta \Delta \hat{\boldsymbol{d}}_2^* + \sin\theta \Delta \hat{\boldsymbol{d}}_3^* \\ \Delta \hat{\boldsymbol{e}}_t^* &= \begin{cases} -\Delta \hat{\boldsymbol{e}}_\theta^* & \text{if } \boldsymbol{v}^* \cdot \hat{\boldsymbol{e}}_\theta^* < 0 \\ \Delta \hat{\boldsymbol{e}}_\theta^* & \text{if } \boldsymbol{v}^* \cdot \hat{\boldsymbol{e}}_\theta^* \geq 0 \end{cases}, \\ \Delta \hat{\boldsymbol{e}}_\theta^* &= -\sin\theta \Delta \hat{\boldsymbol{d}}_2^* + \cos\theta \Delta \hat{\boldsymbol{d}}_3^*, \\ \Delta \hat{\boldsymbol{e}}_n^* &= \Delta \hat{\boldsymbol{e}}_b^* \times \hat{\boldsymbol{e}}_t^* + \hat{\boldsymbol{e}}_b^* \times \Delta \hat{\boldsymbol{e}}_t^*, \\ \Delta \hat{\boldsymbol{e}}_b^* &= \frac{\Delta \left(\hat{\boldsymbol{e}}_t^* \times \boldsymbol{v}^* \right) |\hat{\boldsymbol{e}}_t^* \times \boldsymbol{v}^*| - \left(\hat{\boldsymbol{e}}_t^* \times \boldsymbol{v}^* \right) \Delta |\hat{\boldsymbol{e}}_t^* \times \boldsymbol{v}^*|}{|\hat{\boldsymbol{e}}_t^* \times \boldsymbol{v}^*|^2}, \end{aligned}$$

and

$$\Delta |\hat{\boldsymbol{e}}_t^* \times \boldsymbol{v}^*| = \frac{(\hat{\boldsymbol{e}}_t^* \times \boldsymbol{v}^*) \cdot \Delta \left(\hat{\boldsymbol{e}}_t^* \times \boldsymbol{v}^* \right)}{|\hat{\boldsymbol{e}}_t^* \times \boldsymbol{v}^*|} = \hat{\boldsymbol{e}}_b^* \cdot \left(\Delta \hat{\boldsymbol{e}}_t^* \times \boldsymbol{v}^* + \hat{\boldsymbol{e}}_t^* \times \Delta \boldsymbol{v}^* \right),$$

Finally, simplifying (4.5.1), we obtain

$$\Delta \mathtt{f}_{\text{iner}}^* = \mathtt{M}^* \Delta \ddot{\mathtt{q}} + \mathtt{G}^* \Delta \dot{\mathtt{q}} + \mathtt{K}_{\text{iner}}^* \Delta \mathtt{q}, \tag{4.5.3a}$$

$$\Delta \mathtt{f}_{\text{grav}}^* = \mathtt{K}_{\text{grav}}^* \Delta \mathtt{q} \tag{4.5.3b}$$

and

$$\Delta \mathtt{f}_{\text{aero}}^* = \mathtt{G}_{\text{aero}}^* \Delta \dot{\mathtt{q}} + \mathtt{K}_{\text{aero}}^* \Delta \mathtt{q}, \tag{4.5.3c}$$

where the column vectors $\Delta \mathtt{q}^{\mathsf{T}} = [\Delta \boldsymbol{u} \quad \Delta \boldsymbol{\varphi}]$, $\Delta \dot{\mathtt{q}}^{\mathsf{T}} = [\Delta \dot{\boldsymbol{u}} \quad \Delta \dot{\boldsymbol{\varphi}}]$ and $\Delta \ddot{\mathtt{q}}^{\mathsf{T}} = [\Delta \ddot{\boldsymbol{u}} \quad \Delta \ddot{\boldsymbol{\varphi}}]$, while the matrices

$$\mathtt{M}^* = \begin{bmatrix} m^* \mathbf{1} & -m^* \widetilde{\boldsymbol{\ell}^*} \cdot \boldsymbol{T}^* \\ m^* \widetilde{\boldsymbol{\ell}^*} & \boldsymbol{\mathcal{J}}^* \cdot \boldsymbol{T}^* - m^* \widetilde{\boldsymbol{\ell}^*}^2 \cdot \boldsymbol{T}^* \end{bmatrix},$$

$$\mathtt{G}^* = \begin{bmatrix} \mathbf{O} & \boldsymbol{G}_{12}^* \\ \mathbf{O} & 2\boldsymbol{\mathcal{J}}^* \cdot \dot{\boldsymbol{T}}^* + \left(\dot{\boldsymbol{\mathcal{J}}}^* - \widetilde{\boldsymbol{h}^*} \right) \cdot \boldsymbol{T}^* + \widetilde{\boldsymbol{\ell}^*} \cdot \boldsymbol{G}_{12}^* \end{bmatrix},$$

$$\mathsf{K}^*_{\text{iner}} = \begin{bmatrix} \mathbf{O} & \boldsymbol{K}^*_{12} \\ \mathbf{O} & \boldsymbol{\mathcal{J}}^* \cdot \ddot{\boldsymbol{T}}^* + \left(\dot{\boldsymbol{\mathcal{J}}}^* - \widetilde{\boldsymbol{h}}^*\right) \cdot \dot{\boldsymbol{T}}^* - \dot{\widetilde{\boldsymbol{h}}}^* \cdot \boldsymbol{T}^* + \boldsymbol{K}^*_{22} \end{bmatrix},$$

$$\mathsf{K}^*_{\text{grav}} = \begin{bmatrix} \boldsymbol{O} & \boldsymbol{O} \\ \boldsymbol{O} & -(\widetilde{\mathsf{m}^* \boldsymbol{g}}) \cdot \widetilde{\boldsymbol{\ell}}^* \cdot \boldsymbol{T}^* \end{bmatrix},$$

$$\mathsf{G}^*_{\text{aero}} = \int_0^{2\pi} \begin{bmatrix} -\boldsymbol{G}^{*\text{cyl}}_{\text{aero}} & \boldsymbol{G}^{*\text{cyl}}_{\text{aero}} \cdot \widetilde{\boldsymbol{\ell}}^*_r \cdot \boldsymbol{T}^* \\ -\widetilde{\boldsymbol{\ell}}^*_r \cdot \boldsymbol{G}^{*\text{cyl}}_{\text{aero}} & \widetilde{\boldsymbol{\ell}}^*_r \cdot \boldsymbol{G}^{*\text{cyl}}_{\text{aero}} \cdot \widetilde{\boldsymbol{\ell}}^*_r \cdot \boldsymbol{T}^* \end{bmatrix} r^* d\theta$$

and

$$\mathsf{K}^*_{\text{aero}} = \int_0^{2\pi} \begin{bmatrix} \mathbf{O} & \boldsymbol{K}^{*\text{cyl}}_{\text{aero}} \\ \mathbf{O} & \text{sk}\left(\bar{\boldsymbol{n}}^{*\text{cyl}}_{\text{aero}}\right) \cdot \widetilde{\boldsymbol{\ell}}^*_r \cdot \boldsymbol{T}^* + \widetilde{\boldsymbol{\ell}}^*_r \cdot \boldsymbol{K}^{*\text{cyl}}_{\text{aero}} \end{bmatrix} r^* d\theta,$$

where we denote

$$\boldsymbol{G}^*_{12} = -\mathsf{m}^* \left\{ \widetilde{\boldsymbol{\ell}}^* \cdot \left(2\dot{\boldsymbol{T}}^* - \widetilde{\boldsymbol{\omega}}^* \cdot \boldsymbol{T}^*\right) + \left(\widetilde{\widetilde{\boldsymbol{\omega}}^* \cdot \boldsymbol{\ell}^*} + \widetilde{\boldsymbol{\omega}}^* \cdot \widetilde{\boldsymbol{\ell}}^*\right) \cdot \boldsymbol{T}^* \right\},$$

$$\begin{aligned} \boldsymbol{K}^*_{12} = -\mathsf{m}^* \Bigg\{ & \widetilde{\boldsymbol{\ell}}^* \cdot \left(\ddot{\boldsymbol{T}}^* - \widetilde{\boldsymbol{\omega}}^* \cdot \dot{\boldsymbol{T}}^* - \dot{\widetilde{\boldsymbol{\omega}}}^* \cdot \boldsymbol{T}^*\right) + \left(\dot{\widetilde{\boldsymbol{\omega}}}^* + \widetilde{\boldsymbol{\omega}}^{*2}\right) \cdot \widetilde{\boldsymbol{\ell}}^* \cdot \boldsymbol{T}^* \\ & + \left(\widetilde{\widetilde{\boldsymbol{\omega}}^* \cdot \boldsymbol{\ell}^*} + \widetilde{\boldsymbol{\omega}}^* \cdot \widetilde{\boldsymbol{\ell}}^*\right) \cdot \left(\dot{\boldsymbol{T}}^* - \widetilde{\boldsymbol{\omega}}^* \cdot \boldsymbol{T}^*\right) \Bigg\}, \end{aligned}$$

$$\boldsymbol{K}^*_{22} = \mathsf{m}^* \ddot{\widetilde{\boldsymbol{u}}}^* \cdot \widetilde{\boldsymbol{\ell}}^* \cdot \boldsymbol{T}^* + \widetilde{\boldsymbol{\ell}}^* \cdot \boldsymbol{K}^*_{12},$$

$$\boldsymbol{\ell}^*_r = \boldsymbol{r}^* + \boldsymbol{\ell}^*, \quad \widetilde{\boldsymbol{\ell}}^*_r = \text{sk}\left(\boldsymbol{\ell}^*_r\right),$$

$$\begin{aligned} \boldsymbol{G}^{*\text{cyl}}_{\text{aero}} = {} & \mathsf{c}_n \rho_{\text{air}} r^*_{\text{cs}} \left(\boldsymbol{v}^* \cdot \hat{\boldsymbol{e}}^*_n\right) \left(\hat{\boldsymbol{e}}^*_n \otimes \hat{\boldsymbol{e}}^*_n + \hat{\boldsymbol{d}}^*_1 \otimes \hat{\boldsymbol{d}}^*_1 + \hat{\boldsymbol{e}}^*_r \otimes \hat{\boldsymbol{e}}^*_r\right) \\ & + 2\, \mathsf{c}_t \rho_{\text{air}} \pi r^*_{\text{cs}} \left(\boldsymbol{v}^* \cdot \hat{\boldsymbol{e}}^*_t\right) \left(\hat{\boldsymbol{e}}^*_t \otimes \hat{\boldsymbol{e}}^*_t\right), \end{aligned}$$

and

$$\begin{aligned} \boldsymbol{K}^{*\text{cyl}}_{\text{aero}} = {} & \boldsymbol{G}^{*\text{cyl}}_{\text{aero}} \cdot \left(\widetilde{\boldsymbol{\ell}}^*_r \cdot \dot{\boldsymbol{T}}^* + \widetilde{\widetilde{\boldsymbol{\omega}}^* \cdot \boldsymbol{\ell}^*_r} \cdot \boldsymbol{T}^*\right) - \mathsf{c}_n \rho_{\text{air}} r^*_{\text{cs}} \left(\boldsymbol{v}^* \cdot \hat{\boldsymbol{e}}^*_n\right) \Big[\left(\hat{\boldsymbol{d}}^*_1 \otimes \boldsymbol{v}^*\right) \cdot \widetilde{\hat{\boldsymbol{d}}^*_1} \\ & + \left(\hat{\boldsymbol{e}}^*_r \otimes \boldsymbol{v}^*\right) \cdot \widetilde{\hat{\boldsymbol{e}}^*_r} + \left\{\left(\hat{\boldsymbol{e}}^*_n \otimes \boldsymbol{v}^*\right) + \left(\boldsymbol{v}^* \cdot \hat{\boldsymbol{e}}^*_n\right) \mathbf{1}\right\} \cdot \widetilde{\hat{\boldsymbol{e}}^*_n} \Big] \cdot \boldsymbol{T}^* \\ & - \mathsf{c}_t \rho_{\text{air}} \pi r^*_{\text{cs}} \left(\boldsymbol{v}^* \cdot \hat{\boldsymbol{e}}^*_t\right) \left\{2 \left(\hat{\boldsymbol{e}}^*_t \otimes \boldsymbol{v}^*\right) + \left(\boldsymbol{v}^* \cdot \hat{\boldsymbol{e}}^*_t\right) \mathbf{1}\right\} \cdot \widetilde{\hat{\boldsymbol{e}}^*_t} \cdot \boldsymbol{T}^*. \end{aligned}$$

Using these definition we now formulate the finite element equation.

4.6 Linearized Finite Element (FE) Equation

The geometrically exact beam equations (2.2.7a) and (2.2.7b) and its weak form (2.5.1a) are formulated in terms of the state vector $\mathsf{q}^{\mathsf{T}}(s,t) = [\boldsymbol{u}^{\mathsf{T}}(s,t)\ \boldsymbol{\varphi}^{\mathsf{T}}(s,t)]$, which comprises of the displacement $\boldsymbol{u}(s,t)$ of the centroidal line and rotation $\boldsymbol{\varphi}(s,t)$ of the rigid cross-sections, both of

which are functions of material arc-length parameter s and time t. The method of finite elements is implemented to solve the linearised weak form (4.1.1) by discretizing the cable of initial length ℓ into N elements, where each element has an initial length h. Then, the elemental state vector is approximated as

$$\mathtt{q}_e(s,t) = \mathtt{N}(s)\mathtt{p}_e(t),$$

where the 6×12 linear interpolation matrix

$$\mathtt{N}(s) = \begin{bmatrix} N_a(s)\mathbf{1} & \mathbf{O} & N_b(s)\mathbf{1} & \mathbf{O} \\ \mathbf{O} & N_a(s)\mathbf{1} & \mathbf{O} & N_b(s)\mathbf{1} \end{bmatrix}$$

stores the shape functions, $N_a(s) = 1 - s/h$ and $N_b(s) = s/h$, for a two-node element of length h and nodes a and b, while $\mathtt{p}_e^{\mathsf{T}}(t) = [\mathtt{p}_a^{\mathsf{T}}(t) \quad \mathtt{p}_b^{\mathsf{T}}(t)]$ is a 12×1 vector of time varying values at each node identified by the subscripts. Note that for a choice of element with more nodes the order of the shape function polynomial and the size of $\mathtt{N}$ and $\mathtt{p}_e$ are accordingly higher; see for example [Bathe, 2006, Chap. 5]. We use the two-node element with linear shape functions defined above.

The derivatives of $\mathtt{q}_e$ assume the forms:

$$\mathtt{q}_e' = \mathtt{N}'(s)\mathtt{p}_e(t), \quad \dot{\mathtt{q}}_e = \mathtt{N}(s)\dot{\mathtt{p}}_e(t), \quad \text{and} \quad \ddot{\mathtt{q}}_e = \mathtt{N}(s)\ddot{\mathtt{p}}_e(t),$$

while their increments are represented as

$$\begin{aligned} \Delta\mathtt{q}_e &= \mathtt{N}(s)\Delta\mathtt{p}_e(t), \quad \Delta\mathtt{q}_e' = \mathtt{N}'(s)\Delta\mathtt{p}_e(t), \\ \Delta\dot{\mathtt{q}}_e &= \mathtt{N}(s)\Delta\dot{\mathtt{p}}_e(t), \quad \text{and} \quad \Delta\ddot{\mathtt{q}}_e = \mathtt{N}(s)\Delta\ddot{\mathtt{p}}_e(t), \end{aligned} \tag{4.6.1}$$

where $\square'$ denotes the derivative with respect to s, while $\dot{\square}$ and $\ddot{\square}$ represents the first and the second time derivatives, respectively. Similarly, the admissible weight functions that appear in the weak formulation are interpolated as follows:

$$\eta_e(s) = \mathtt{N}(s)\xi_e, \text{ and } \eta_e'(s) = \mathtt{N}'(s)\xi_e.$$

Using the above interpolation in the linearized weak formulation (4.1.1), we assemble all the elemental forms of the force vectors given in (2.5.1g) and their increments given in Sec. 4.4 as follows:

$$\sum_{e=1}^{\mathsf{N}} \xi_e^{\mathsf{T}} \left\{ \int_0^h \mathtt{N}^{\mathsf{T}} \left(\mathtt{f}_{\mathsf{iner}} + \Delta\mathtt{f}_{\mathsf{iner}}\right)_e ds + \int_0^h \mathtt{N}'^{\mathsf{T}} \left(\mathtt{f}_{\mathsf{int}}^{\mathsf{I}} + \Delta\mathtt{f}_{\mathsf{int}}^{\mathsf{I}}\right)_e + \mathtt{N}^{\mathsf{T}} \left(\mathtt{f}_{\mathsf{int}}^{\mathsf{II}} + \Delta\mathtt{f}_{\mathsf{int}}^{\mathsf{II}}\right)_e ds \right.$$

$$-\int_0^h \mathtt{N}^{\mathsf{T}}\left(\mathtt{f}_{\text{ext}}+\Delta\mathtt{f}_{\text{ext}}\right)_e ds\Bigg\} - \xi_{\mathtt{N}}^{\mathsf{T}}\mathtt{N}^{\mathsf{T}}(h)\left(\mathtt{f}_\ell+\Delta\mathtt{f}_\ell\right)=0.$$

For arbitrary/nontrivial values of the weights ξ_e, we have for each element

$$\begin{aligned}
0 &= \int_0^h \mathtt{N}^{\mathsf{T}}\left(\mathtt{f}_{\text{iner}}+\Delta\mathtt{f}_{\text{iner}}\right)_e ds + \int_0^h \mathtt{N}'^{\mathsf{T}}\left(\mathtt{f}^{\mathsf{I}}_{\text{int}}+\Delta\mathtt{f}^{\mathsf{I}}_{\text{int}}\right)_e + \mathtt{N}^{\mathsf{T}}\left(\mathtt{f}^{\mathsf{II}}_{\text{int}}+\Delta\mathtt{f}^{\mathsf{II}}_{\text{int}}\right)_e ds \\
&\quad - \int_0^h \mathtt{N}^{\mathsf{T}}\left(\mathtt{f}_{\text{ext}}+\Delta\mathtt{f}_{\text{ext}}\right)_e ds \\
&= \left[\int_0^h \left(\mathtt{N}^{\mathsf{T}}\mathtt{f}_{\text{iner}}+\mathtt{N}'^{\mathsf{T}}\mathtt{f}^{\mathsf{I}}_{\text{int}}+\mathtt{N}^{\mathsf{T}}\mathtt{f}^{\mathsf{II}}_{\text{int}}\right)_e ds - \int_0^h \mathtt{N}^{\mathsf{T}}\left(\mathtt{f}_{\text{ext}}\right)_e\, ds\right] + \left[\int_0^h \Big\{\mathtt{N}^{\mathsf{T}}\mathtt{K}_{\text{iner}}\mathtt{N}\right. \\
&\quad \left. + \mathtt{N}'^{\mathsf{T}}\mathtt{K}^{\mathsf{I}}_q\mathtt{N} + \mathtt{N}'^{\mathsf{T}}\mathtt{K}^{\mathsf{I}}_{q'}\mathtt{N}' + \mathtt{N}^{\mathsf{T}}\mathtt{K}^{\mathsf{II}}_q\mathtt{N} + \mathtt{N}^{\mathsf{T}}\left(\mathtt{K}^{\mathsf{II}}_{q'} - \mathtt{K}_{\text{aero}}\right)\mathtt{N}'\Big\}_e ds\right]\Delta\mathtt{p}_e \\
&\quad + \left[\int_0^h \mathtt{N}^{\mathsf{T}}\left(\mathtt{G}-\mathtt{G}_{\text{aero}}\right)_e \mathtt{N}\, ds\right]\Delta\dot{\mathtt{p}}_e + \left[\int_0^h \mathtt{N}^{\mathsf{T}}\left(\mathtt{M}\right)_e \mathtt{N}\, ds\right]\Delta\ddot{\mathtt{p}}_e,
\end{aligned}$$

which can be rewritten as the matrix equation

$$\mathtt{M}_e\Delta\ddot{\mathtt{p}}_e + \mathtt{G}_e\Delta\dot{\mathtt{p}}_e + \mathtt{K}_e\Delta\mathtt{p}_e = \mathtt{f}_{\text{ext},e} - \mathtt{f}_e, \tag{4.6.2}$$

where

$$\begin{aligned}
\mathtt{M}_e &= \int_0^h \mathtt{N}^{\mathsf{T}}\left(\mathtt{M}\right)_e \mathtt{N}\, ds, \quad \mathtt{G}_e = \int_0^h \mathtt{N}^{\mathsf{T}}\left(\mathtt{G}-\mathtt{G}_{\text{aero}}\right)_e \mathtt{N}\, ds, \\
\mathtt{K}_e &= \int_0^h \left\{\mathtt{N}'^{\mathsf{T}}\mathtt{K}^{\mathsf{I}}_q\mathtt{N} + \mathtt{N}'^{\mathsf{T}}\mathtt{K}^{\mathsf{I}}_{q'}\mathtt{N}' + \mathtt{N}^{\mathsf{T}}\mathtt{K}^{\mathsf{II}}_q\mathtt{N} + \mathtt{N}^{\mathsf{T}}\left(\mathtt{K}^{\mathsf{II}}_{q'} - \mathtt{K}_{\text{aero}}\right)\mathtt{N}'\right\}_e ds, \\
\mathtt{f}_{\text{ext},e} &= \int_0^h \mathtt{N}^{\mathsf{T}}\left(\mathtt{f}_{\text{ext}}\right)_e\, ds, \quad \text{and} \quad \mathtt{f}_e = \int_0^h \left(\mathtt{N}^{\mathsf{T}}\mathtt{f}_{\text{iner}} + \mathtt{N}'^{\mathsf{T}}\mathtt{f}^{\mathsf{I}}_{\text{int}} + \mathtt{N}^{\mathsf{T}}\mathtt{f}^{\mathsf{II}}_{\text{int}}\right)_e ds,
\end{aligned}$$

are the elemental mass matrix, damping matrix, tangent stiffness matrix, external force vector and unbalanced force vector, respectively. For each element e, the forces $\mathtt{f}_{\text{iner}}$, $\mathtt{f}^{\mathsf{I}}_{\text{int}}$, and $\mathtt{f}^{\mathsf{II}}_{\text{int}}$ are given by (2.5.1g); the external force $\mathtt{f}_{\text{ext}}$ is given by (2.6.1); the inertial matrices $\mathtt{K}_{\text{iner}}$, $\mathtt{G}$ and $\mathtt{M}$ are given by (4.4.1); the internal stiffness matrices $\mathtt{K}^{\mathsf{I}}_q$ and $\mathtt{K}^{\mathsf{I}}_{q'}$ are given by (4.4.2b), $\mathtt{K}^{\mathsf{II}}_q$ and $\mathtt{K}^{\mathsf{II}}_{q'}$ are given by (4.4.3b); the aerodynamic damping $\mathtt{G}_{\text{aero}}$ and stiffness $\mathtt{K}_{\text{aero}}$ are provided by (4.4.4).

Additionally, for nontrivial value of the weight $\xi_{\mathtt{N}}$, we have the following boundary condition at the last node, i.e. node-b of the $\mathtt{N}^{\text{th}}$ element:

$$\mathtt{f}_\ell(t) + \Delta\mathtt{f}_\ell(t) = 0 \tag{4.6.3}$$

where the reaction/impedance from the slung load $\mathtt{f}_\ell$ is given by (3.3.1) and its increment $\Delta\mathtt{f}_\ell$ given by (4.5.1). Using (4.5.3) we can now rewrite $\Delta\mathtt{f}_\ell$ as:

$$\Delta\mathtt{f}_\ell = -\mathtt{M}^*\Delta\ddot{\mathtt{p}}_{N,b} - (\mathtt{G}^* - \mathtt{G}^*_{\text{aero}})\,\Delta\dot{\mathtt{p}}_{N,b} - \left(\mathtt{K}^*_{\text{iner}} - \mathtt{K}^*_{\text{grav}} - \mathtt{K}^*_{\text{aero}}\right)\Delta\mathtt{p}_{N,b}.$$

Finally, we assemble the elemental equations (4.6.2) and the boundary conditions (4.6.3) into the following *global* form:

$$\mathsf{M}\Delta\ddot{\mathsf{p}} + \mathsf{G}\Delta\dot{\mathsf{p}} + \mathsf{K}\Delta\mathsf{p} = \mathsf{f}_{\text{ext}} - \mathsf{f}. \tag{4.6.4}$$

The FE equation (4.6.4) is then solved for the incremental nodal quantities $\Delta\mathsf{p}$, $\Delta\dot{\mathsf{p}}$ and $\Delta\ddot{\mathsf{p}}$ at each time-step by employing the *Newmark-β* time integration technique, which we now discuss.

4.6.1 Numerical integration of FE equations: Newmark-β method

The Newmark-β method, [Bathe, 2006; Mäkinen, 2008; Newmark, 1959; Simo & Vu-Quoc, 1986b, 1988], is an implicit time-integration scheme for solving the transient equations of motion of the form (4.6.4). We begin by evaluating (4.6.4) at a future time step $t + \Delta t$:

$$\mathsf{M}\Delta\ddot{\mathsf{p}}(t+\Delta t) + \mathsf{G}\Delta\dot{\mathsf{p}}(t+\Delta t) + \mathsf{K}\Delta\mathsf{p}(t+\Delta t) = \mathsf{f}_{\text{ext}}(t+\Delta t) - \mathsf{f}(t+\Delta t), \tag{4.6.5}$$

where Δt is the increment in time t. In the Newmark-β method, we employ truncated Taylor series expansion of $\mathsf{p}(t+\Delta t)$ and $\dot{\mathsf{p}}(t+\Delta t)$ about the current time t, while assuming linear $\ddot{\mathsf{p}}$ within the time increment Δt:

$$\mathsf{p}(t+\Delta t) = \mathsf{p}(t) + (\Delta t)\,\dot{\mathsf{p}}(t) + \frac{(\Delta t)^2}{2}\,\ddot{\mathsf{p}}(t) + \beta(\Delta t)^3\,\frac{\ddot{\mathsf{p}}(t+\Delta t) - \ddot{\mathsf{p}}(t)}{(\Delta t)}$$

and

$$\dot{\mathsf{p}}(t+\Delta t) = \dot{\mathsf{p}}(t) + (\Delta t)\,\ddot{\mathsf{p}}(t) + \tau(\Delta t)^2\,\frac{\ddot{\mathsf{p}}(t+\Delta t) - \ddot{\mathsf{p}}(t)}{(\Delta t)},$$

where β and τ are Newmark's parameters, generally taken as $\beta = 0.25$ and $\tau = 0.5$.
When these are linearized and then replaced in (4.6.5) we obtain

$$\left[\frac{1}{\beta(\Delta t)^2}\,\mathsf{M}(t+\Delta t) + \frac{\tau}{\beta\Delta t}\,\mathsf{G}(t+\Delta t) + \mathsf{K}(t+\Delta t)\right]\Delta\mathsf{p}(t+\Delta t)$$
$$= \mathsf{f}_{\text{ext}}(t+\Delta t) - \mathsf{f}(t+\Delta t). \tag{4.6.6}$$

To add numerical damping of (say) $\zeta\%$, which is common for structural dynamics problems, we set $\tau = 0.5 + \zeta/100$ and $\beta = 0.25(1+\zeta/100)^2$ [Hilber et al., 1977].

Equation (4.6.6) is solved for $\Delta\mathsf{p}$ at time $t+\Delta t$ by calculating M, G, K, f_{ext} and f at the *predicted* state vectors. Using $\Delta\mathsf{p}$, the predictions are then *corrected*, and the convergence is checked. If

the convergence criterion is satisfied then we repeat the above procedure to compute the state vectors at the next time step. However, if the convergence criterion is *not* satisfied then we recompute $\Delta \mathrm{p}$ from (4.6.6) by recalculating M, G, K, $\mathrm{f}_{\mathrm{ext}}$ and f at the *corrected* state vectors. This process is repeated until converged solution is obtained for that time step. The entire procedure is summarized in Algorithm 4.1.

Algorithm 4.1: The Newmark-β numerical time-integration algorithm

Input: Initial conditions at $t = 0$: $\mathrm{p}(0)$, $\dot{\mathrm{p}}(0)$ and $\ddot{\mathrm{p}}(0)$.

while $t + \Delta t \leq t_{max}$ **do** *%Time marching loop*

Predictions at $t + \Delta t$:

$$\ddot{\mathrm{p}}(t+\Delta t) = \left(1 - \frac{1}{2\beta}\right) \ddot{\mathrm{p}}(t) - \frac{1}{\beta(\Delta t)} \dot{\mathrm{p}}(t)$$

$$\dot{\mathrm{p}}(t+\Delta t) = \dot{\mathrm{p}}(t) + (\Delta t)\left\{(1-\tau)\,\ddot{\mathrm{p}}(t) + \tau\,\ddot{\mathrm{p}}(t+\Delta t)\right\}$$

$$\mathrm{p}(t+\Delta t) = \mathrm{p}(t)$$

repeat *%Newton-Raphson loop*

Compute M, G, K, $\mathrm{f}_{\mathrm{ext}}$ and f using $\ddot{\mathrm{p}}(t+\Delta t)$, $\dot{\mathrm{p}}(t+\Delta t)$ and $\mathrm{p}(t+\Delta t)$.

Compute $\Delta \mathrm{p}(t+\Delta t)$ from (4.6.6).

Corrections at $t + \Delta t$:

$$\ddot{\mathrm{p}}(t+\Delta t) \longleftarrow \ddot{\mathrm{p}}(t+\Delta t) + \frac{1}{\beta(\Delta t)^2}\,\Delta \mathrm{p}(t+\Delta t)$$

$$\dot{\mathrm{p}}(t+\Delta t) \longleftarrow \dot{\mathrm{p}}(t+\Delta t) + \frac{\tau}{\beta(\Delta t)}\,\Delta \mathrm{p}(t+\Delta t)$$

$$\mathrm{p}(t+\Delta t) \longleftarrow \mathrm{p}(t+\Delta t) + \Delta \mathrm{p}(t+\Delta t)$$

Re-compute $\mathrm{f}_{\mathrm{ext}}$ and f using the corrected $\ddot{\mathrm{p}}(t+\Delta t)$, $\dot{\mathrm{p}}(t+\Delta t)$ and $\mathrm{p}(t+\Delta t)$.

Check for convergence.

until $max\{abs\,(\mathrm{f}_{ext} - \mathrm{f})\} < 10^{-8}$ *% Convergence criterion*

Update time: $t \longleftarrow t + \Delta t$

Appendix

4.a The tangent tensor, its derivative and angular velocity

In this Appendix, we derive a useful relationship between $\boldsymbol{T}$, $\dot{\boldsymbol{T}}$ and $\widetilde{\boldsymbol{\omega}}$ given by

$$\dot{\boldsymbol{T}} = \frac{\partial \boldsymbol{\omega}}{\partial \boldsymbol{\varphi}} + \widetilde{\boldsymbol{\omega}} \cdot \boldsymbol{T}. \tag{4.a.1a}$$

First, we define the basis vectors $\boldsymbol{t}_i$ of the tangent tensor $\boldsymbol{T}$ by $\boldsymbol{t}_i = \boldsymbol{T} \cdot \hat{\boldsymbol{e}}_i,$ for $i = 1, 2, 3$. We may thus express $\boldsymbol{T}$ as

$$\boldsymbol{T} = \boldsymbol{t}_i \otimes \hat{\boldsymbol{e}}_i.$$

Then the definition of angular velocity (2.c.6) can be written as

$$\boldsymbol{\omega} = \boldsymbol{T} \cdot \dot{\boldsymbol{\varphi}} = \boldsymbol{t}_i \otimes \hat{\boldsymbol{e}}_i \cdot \dot{\boldsymbol{\varphi}} = \dot{\varphi}_i \boldsymbol{t}_i, \tag{4.a.1b}$$

where $\dot{\varphi}_i$ are components of $\dot{\boldsymbol{\varphi}}$ along $\hat{\boldsymbol{e}}_i$.

Alternatively, the definition (2.c.3) can be modified using the notation $\boldsymbol{R}_{,i} \equiv \dfrac{\partial \boldsymbol{R}}{\partial \varphi_i}$, for brevity,

$$\boldsymbol{\omega} = \operatorname{ax}(\dot{\boldsymbol{R}} \cdot \boldsymbol{R}^{\mathsf{T}}) = \dot{\varphi}_i \operatorname{ax}(\boldsymbol{R}_{,i} \cdot \boldsymbol{R}^{\mathsf{T}}). \tag{4.a.1c}$$

Now, comparing (4.a.1b) and (4.a.1c) we deduce that

$$\boldsymbol{t}_i = \operatorname{ax}(\boldsymbol{R}_{,i} \cdot \boldsymbol{R}^{\mathsf{T}}), \quad \text{or} \quad \widetilde{\boldsymbol{t}_i} = \boldsymbol{R}_{,i} \cdot \boldsymbol{R}^{\mathsf{T}}, \tag{4.a.1d}$$

where $\widetilde{\boldsymbol{t}_i}$ is the skew-symmetric tensors corresponding to $\boldsymbol{t}_i$.

Second, using (4.a.1d) in (2.a.3) we obtain

$$\begin{aligned}
\widetilde{\widetilde{\boldsymbol{t}_i} \cdot \boldsymbol{t}_j} &= \widetilde{\boldsymbol{t}_i} \cdot \widetilde{\boldsymbol{t}_j} - \widetilde{\boldsymbol{t}_j} \cdot \widetilde{\boldsymbol{t}_i} = \widetilde{\boldsymbol{t}_j} \cdot \widetilde{\boldsymbol{t}_i}^{\mathsf{T}} - \widetilde{\boldsymbol{t}_i} \cdot \widetilde{\boldsymbol{t}_j}^{\mathsf{T}} \\
&= (\boldsymbol{R}_{,j} \cdot \boldsymbol{R}^{\mathsf{T}}) \cdot (\boldsymbol{R}_{,i} \cdot \boldsymbol{R}^{\mathsf{T}})^{\mathsf{T}} - (\boldsymbol{R}_{,i} \cdot \boldsymbol{R}^{\mathsf{T}}) \cdot (\boldsymbol{R}_{,j} \cdot \boldsymbol{R}^{\mathsf{T}})^{\mathsf{T}} \\
&= \boldsymbol{R}_{,j} \cdot \boldsymbol{R}_{,i}^{\mathsf{T}} - \boldsymbol{R}_{,i} \cdot \boldsymbol{R}_{,j}^{\mathsf{T}} \\
&= (\boldsymbol{R}_{,ji} \cdot \boldsymbol{R}^{\mathsf{T}} + \boldsymbol{R}_{,j} \cdot \boldsymbol{R}_{,i}^{\mathsf{T}}) - (\boldsymbol{R}_{,ij} \cdot \boldsymbol{R}^{\mathsf{T}} + \boldsymbol{R}_{,i} \cdot \boldsymbol{R}_{,j}^{\mathsf{T}}) \\
&= \frac{\partial (\boldsymbol{R}_{,j} \cdot \boldsymbol{R}^{\mathsf{T}})}{\partial \varphi_i} - \frac{\partial (\boldsymbol{R}_{,i} \cdot \boldsymbol{R}^{\mathsf{T}})}{\partial \varphi_j},
\end{aligned} \tag{4.a.1e}$$

where $\boldsymbol{R}_{,ij} = \boldsymbol{R}_{,ji} = \partial^2 \boldsymbol{R} / \partial \varphi_i \partial \varphi_j$. The axial vector of (4.a.1e) is extracted using (4.a.1d):

$$\widetilde{\boldsymbol{t}_i} \cdot \boldsymbol{t}_j = \frac{\partial \boldsymbol{t}_j}{\partial \varphi_i} - \frac{\partial \boldsymbol{t}_i}{\partial \varphi_j}. \tag{4.a.1f}$$

Further, the tensor product of (4.a.1f) with the reference basis $\hat{\boldsymbol{e}}_j$,

$$\widetilde{\boldsymbol{t}_i} \cdot \boldsymbol{t}_j \otimes \hat{\boldsymbol{e}}_j = \frac{\partial (\boldsymbol{t}_j \otimes \hat{\boldsymbol{e}}_j)}{\partial \varphi_i} - \frac{\partial \boldsymbol{t}_i}{\partial \varphi_j} \otimes \hat{\boldsymbol{e}}_j,$$

results in the relation

$$\widetilde{\boldsymbol{t}_i} \cdot \boldsymbol{T} = \frac{\partial \boldsymbol{T}}{\partial \varphi_i} - \frac{\partial \boldsymbol{t}_i}{\partial \boldsymbol{\varphi}}. \tag{4.a.1g}$$

Finally, the product of (4.a.1g) with $\dot{\boldsymbol{\varphi}}$ gives the following relation

$$\widetilde{\boldsymbol{t}_i} \cdot \boldsymbol{T} \cdot \dot{\boldsymbol{\varphi}} = \widetilde{\boldsymbol{t}_i} \cdot \boldsymbol{\omega} = \frac{\partial \boldsymbol{T}}{\partial \varphi_i} \cdot \dot{\boldsymbol{\varphi}} - \frac{\partial \boldsymbol{t}_i}{\partial \boldsymbol{\varphi}} \cdot \dot{\boldsymbol{\varphi}} = \frac{\partial \boldsymbol{\omega}}{\partial \varphi_i} - \frac{d\boldsymbol{t}_i}{dt},$$

whose tensor product with $\hat{\boldsymbol{e}}_i$ results in the desired identity:

$$\widetilde{\boldsymbol{\omega}} \cdot \boldsymbol{t}_i \otimes \hat{\boldsymbol{e}}_i = \widetilde{\boldsymbol{\omega}} \cdot \boldsymbol{T} = \frac{d\boldsymbol{t}_i}{dt} \otimes \hat{\boldsymbol{e}}_i - \frac{\partial \boldsymbol{\omega}}{\partial \varphi_i} \otimes \hat{\boldsymbol{e}}_i = \dot{\boldsymbol{T}} - \frac{\partial \boldsymbol{\omega}}{\partial \boldsymbol{\varphi}}. \tag{4.a.1h}$$

4.b Incremental inertia and elasticity tensors

In this Appendix, we derive the incremental forms of the spatial inertia tensor $\boldsymbol{\mathcal{J}}$ and the spatial elasticity tensors $\boldsymbol{\mathcal{C}_n}$ and $\boldsymbol{\mathcal{C}_m}$. The product of the rate of inertia tensor (2.d.1g) with an arbitrary vector $\boldsymbol{v}$ is

$$\begin{aligned}
\dot{\boldsymbol{\mathcal{J}}} \cdot \boldsymbol{v} &= (\widetilde{\boldsymbol{\omega}} \cdot \boldsymbol{\mathcal{J}} - \boldsymbol{\mathcal{J}} \cdot \widetilde{\boldsymbol{\omega}}) \cdot \boldsymbol{v} = \widetilde{\boldsymbol{\omega}} \cdot \boldsymbol{\mathcal{J}} \cdot \boldsymbol{v} - \boldsymbol{\mathcal{J}} \cdot \widetilde{\boldsymbol{\omega}} \cdot \boldsymbol{v} \\
&= -(\widetilde{\boldsymbol{\mathcal{J}} \cdot \boldsymbol{v}}) \cdot \boldsymbol{\omega} + \boldsymbol{\mathcal{J}} \cdot (\widetilde{\boldsymbol{v}} \cdot \boldsymbol{\omega}) = (\boldsymbol{\mathcal{J}} \cdot \widetilde{\boldsymbol{v}} - \widetilde{\boldsymbol{\mathcal{J}} \cdot \boldsymbol{v}}) \cdot \boldsymbol{\omega} \\
&= (\boldsymbol{\mathcal{J}} \cdot \widetilde{\boldsymbol{v}} - \widetilde{\boldsymbol{\mathcal{J}} \cdot \boldsymbol{v}}) \cdot \boldsymbol{T} \cdot \dot{\boldsymbol{\varphi}}.
\end{aligned} \tag{4.b.1a}$$

Since $\dot{\boldsymbol{\mathcal{J}}} = \lim_{\Delta t \to 0} \Delta \boldsymbol{\mathcal{J}} / \Delta t$ and $\dot{\boldsymbol{\varphi}} = \lim_{\Delta t \to 0} \Delta \boldsymbol{\varphi} / \Delta t$, we can deduce the incremental form

$$(\Delta \boldsymbol{\mathcal{J}}) \cdot \boldsymbol{v} = (\boldsymbol{\mathcal{J}} \cdot \widetilde{\boldsymbol{v}} - \widetilde{\boldsymbol{\mathcal{J}} \cdot \boldsymbol{v}}) \cdot \boldsymbol{T} \cdot (\Delta \boldsymbol{\varphi}), \tag{4.b.1b}$$

so that when $\boldsymbol{v} = \boldsymbol{\omega}$, we have

$$(\Delta \boldsymbol{\mathcal{J}}) \cdot \boldsymbol{\omega} = (\boldsymbol{\mathcal{J}} \cdot \widetilde{\boldsymbol{\omega}} - \widetilde{\boldsymbol{\mathcal{J}} \cdot \boldsymbol{\omega}}) \cdot \boldsymbol{T} \cdot (\Delta \boldsymbol{\varphi}), \tag{4.b.1c}$$

and when $\boldsymbol{v} = \dot{\boldsymbol{\omega}}$ we obtain

$$(\Delta \boldsymbol{\mathcal{J}}) \cdot \dot{\boldsymbol{\omega}} = (\boldsymbol{\mathcal{J}} \cdot \widetilde{\dot{\boldsymbol{\omega}}} - \widetilde{\boldsymbol{\mathcal{J}} \cdot \dot{\boldsymbol{\omega}}}) \cdot \boldsymbol{T} \cdot (\Delta \boldsymbol{\varphi}). \tag{4.b.1d}$$

Furthermore, as the material elasticity tensors (2.4.3) are diagonal in the reference basis $\hat{\boldsymbol{e}}_i$, the incremental forms of the spatial elasticity tensors (2.4.2) are analogous to the incremental spatial inertia tensor (4.b.1c):

$$(\Delta \boldsymbol{\mathcal{C}_n}) \cdot \boldsymbol{\gamma} = (\boldsymbol{\mathcal{C}_n} \cdot \widetilde{\boldsymbol{\gamma}} - \widetilde{\boldsymbol{\mathcal{C}_n} \cdot \boldsymbol{\gamma}}) \cdot \boldsymbol{T} \cdot (\Delta \boldsymbol{\varphi}), \tag{4.b.1e}$$

and

$$(\Delta \boldsymbol{\mathcal{C}_m}) \cdot \boldsymbol{\kappa} = (\boldsymbol{\mathcal{C}_m} \cdot \widetilde{\boldsymbol{\kappa}} - \widetilde{\boldsymbol{\mathcal{C}_m} \cdot \boldsymbol{\kappa}}) \cdot \boldsymbol{T} \cdot (\Delta \boldsymbol{\varphi}). \tag{4.b.1f}$$

Chapter 5

Results and Discussions

In this chapter, we discuss the dynamics of our cable-towed underslung load system by simulating various practical situations with our FE solver. We begin by comparing and validating our GE beam solutions with those given in the literature. For all the computations we use the Newmark parameters $\beta = 0.25$ and $\tau = 0.5$, unless otherwise specified.

5.1 Comparison of GE beam results

Reliability of our GE beam solver is checked by comparing our results with some common examples given in the existing literature, as well as by verifying the conservation of total energy and global angular momentum at every time step.

5.1.1 Pure bending of cantilevered beam

In this example [Simo & Vu-Quoc, 1986b], a planar cantilever beam of unit length and bending rigidity $EI = 2$ (dimensionless) rolls up into a circle when a bending moment $\boldsymbol{m}_3 = 2\pi EI = 4\pi$ is applied at the free end as shown in Fig. 5.1. The same figure also shows two different deformed shapes of the beam's centroidal axis which are obtained from the FE computations using 10 and 100 two-node elements, respectively. According to the classical Euler's beam bending theory, the radius of curvature of the beam under pure bending is $EI/\boldsymbol{m}_3 = 1/\pi$. The FE solution using 100 elements is closest to the exact circle when the convergence criterion in Algorithm 4.1 is tightened to 10^{-14}. The moment of 4π was applied directly in the first iteration while the converged solution was obtained within four iterations.

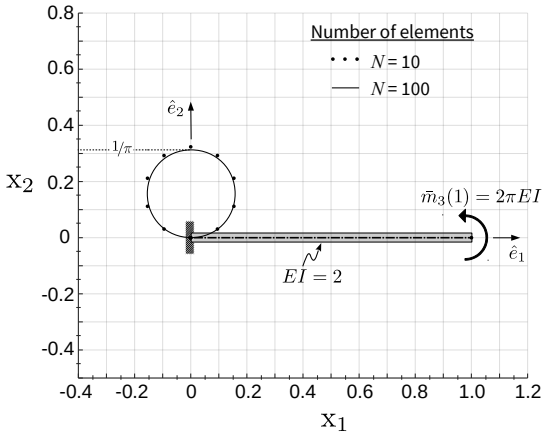

Figure 5.1: *Pure bending of a cantilever beam.*

5.1.2 Damped oscillation of cantilevered beam

This example [Simo & Vu-Quoc, 1986a] demonstrates the vibration of a planar cantilever beam which is initially excited by a concentrated end force as shown in the inset of Fig. 5.2. The free oscillations of the planar beam are damped (see Fig. 5.2) due to the inclusion of velocity proportional viscous damping.

The properties of the beam are: $\ell = 10$ m, $EI = 10^3$ Nm^2, $kGA = EA = 10^6$ N, $\rho = 1$ kg/m and $\mathcal{J} = \rho I = 10$ kg-m^3, while the viscosity of damping is 0.1ρ, i.e. the damping matrix G $= 0.1$M in (4.6.4). The end force $\bar{n}_2 = 37.5$ N is applied initially for 1.5 s, where the amplitude of $\bar{n}_2$ grows linearly from 0 to 37.5 N in the first 0.75 s and then reduces to 0 over the next 0.75 s.

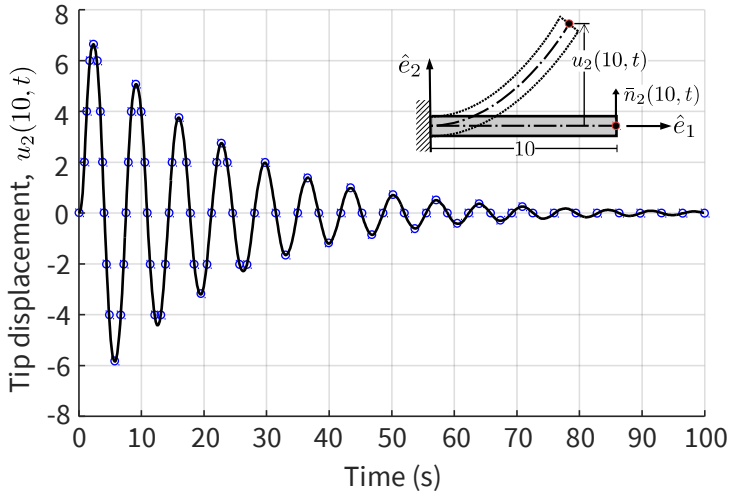

Figure 5.2: *Top inset shows the schematic of a cantilevered beam subjected to vertical force at the tip/free end. The damped free oscillations of the tip, represented by solid line, for a period of* 100 *s (with* Δt*) match well with those from [Simo & Vu-Quoc, 1986a, Ex. 2.5], represented by small circles. In this reference the beam was meshed with* 4 *quadratic elements in contrast to* 10 *linear elements in our simulation.*

5.1.3 Flying spaghetti

A free-ended planar beam, shown at the top of Fig. 5.3, is subjected to an end moment about the negative $\hat{\boldsymbol{e}}_3$ direction and a planar force which is inclined at $\tan^{-1}(8/6)$ rad to the $\hat{\boldsymbol{e}}_1$ axis for a period of 2.5s. This example should be compared with [Simo & Vu-Quoc, 1986a, Ex. 2.2.1] where the beam was initially inclined instead of the force. As expected, the beam goes 'flying' along a direction which is at $\tan^{-1}(8/6)$ rad to the $\hat{\boldsymbol{e}}_1$ axis. The deformed shapes of the beam's centroidal axis at various time steps during the first 15 s of free flight are shown in Fig. 5.3. In these 15 s the beam undergoes two complete revolutions.

The properties of the beam are: $\ell = 10$ m, $EI = 500$ Nm^2, $kGA = EA = 10^4$ N, $\rho = 1$ kg/m and $\mathcal{J} = \rho I = 10$ kg-m^3. The end moment $\bar{\boldsymbol{m}}(0, t \leq 2.5) = -80\hat{\boldsymbol{e}}_3$ Nm and the inclined end force $\bar{\boldsymbol{n}}(0, t \leq 2.5) = -8\cos\{\tan^{-1}(8/6)\}\hat{\boldsymbol{e}}_1 - 8\sin\{\tan^{-1}(8/6)\}\hat{\boldsymbol{e}}_2$ N is applied for the initial 2.5 s, and then removed suddenly.

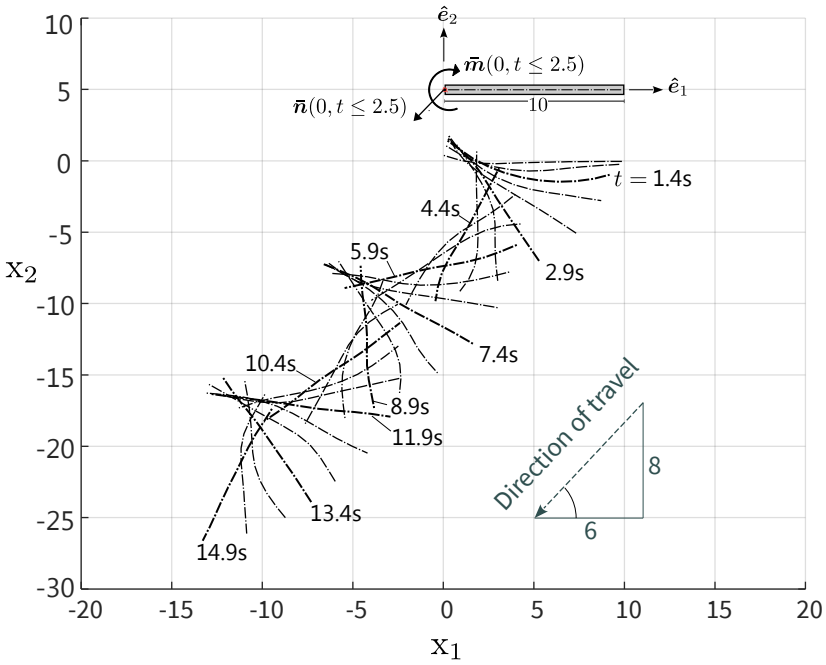

Figure 5.3: *Motion of a free beam due to combined load of force and moment at one end. For FE simulation the number of elements was* 10 *with the time-stepping of* $\Delta t = 0.1$ *s.*

5.1.4 Single blade rotor

In this example, a beam with one end free and other end fixed to a rotor that is free to rotate about the $\hat{\boldsymbol{e}}_3$ axis is shown at the top of Fig. 5.4. The properties of the beam are: $\ell = 10$ m, $EI = 1.4 \times 10^4$ Nm^2, $kGA = 10^7$ N, $EA = 2.8kGA$ N, $\rho = 1.2$ kg/m and $\mathcal{J} = \rho I = 6 \times 10^{-4}$ kg-m^3. The rotor is prescribed the following rotation [Simo & Vu-Quoc, 1988]:

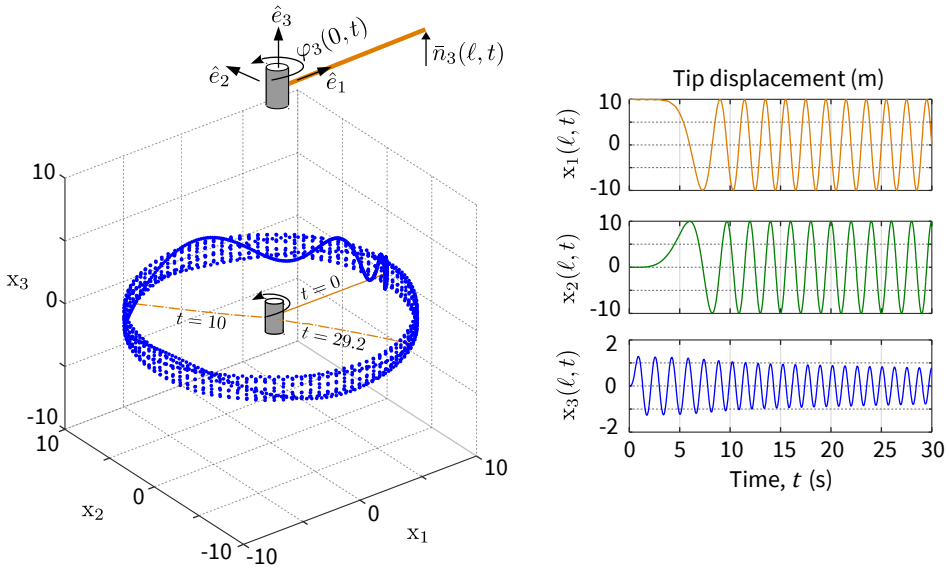

Figure 5.4: *Top figure is a schematic of the clamped rotating beam with an end-force that is applied initially for* 1 *s. Left figure is a 3D plot showing the tip displacement of the rotating beam along with configuration of the beam at arbitrary chosen time steps. Right figure shows all three components of tip displacement as functions of time.*

$$\boldsymbol{\varphi}(0,t) = \begin{cases} \dfrac{\pi}{15}\left\{\dfrac{t^2}{2} - \left(\dfrac{15}{2\pi}\right)^2\left(1-\cos\dfrac{2\pi t}{15}\right)\right\}\hat{\boldsymbol{e}}_3 \text{ rad} & \text{if } 0 \le t \le 15 \text{ s}, \\ \pi(t-7.5)\hat{\boldsymbol{e}}_3 \text{ rad} & \text{if } t > 15 \text{ s}, \end{cases} \tag{5.1.1}$$

which is also plotted in the Fig. 5.5(a). The rotor is smoothly accelerated and decelerated within

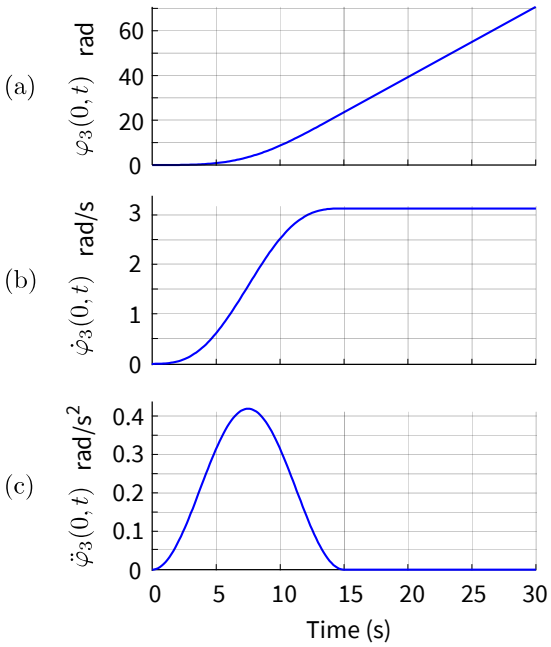

Figure 5.5: *(a) Angular rotation* (5.1.1)*, (b) angular velocity and (c) angular acceleration prescribed to the rotor over a period of* 30 *s.*

the initial 15 s as shown in Fig. 5.5(c), so that a constant angular velocity of π rad/s is maintained

for the remaining period as shown in Fig. 5.5(b). Additionally, the free end of the beam is initially subjected to a force:

$$\bar{\boldsymbol{n}}(\ell,t) = \begin{cases} 80t \text{ N} & \text{if } 0 \leq t \leq 0.5 \text{ s}, \\ 80(1-t)\hat{\boldsymbol{e}}_3 \text{ N} & \text{if } 0.5 < t \leq 1 \text{ s}, \\ 0\hat{\boldsymbol{e}}_3 \text{ N} & \text{if } t \geq 1 \text{ s}, \end{cases} \tag{5.1.2}$$

which displaces the tip of the beam normal to the plane of rotation as shown in Fig. 5.4. The magnitude of force (5.1.2) grows linearly till 0.5 s and then reduces to zero over the next 0.5 s. After $\bar{\boldsymbol{n}}(\ell,t)$ vanishes, only the external moment which is supplied to the rotor for controlling $\boldsymbol{\varphi}(0,t)$ (5.1.1) governs the motion of the beam. Thus, the beam oscillates freely in the $\hat{\boldsymbol{e}}_3$ direction for $t > 1$ s, as shown by the time history of $\mathrm{x}_3(\ell,t)$ in Fig. 5.4, while rotating in the $\hat{\boldsymbol{e}}_1$-$\hat{\boldsymbol{e}}_2$ plane as shown by the periodic oscillations of $\mathrm{x}_1(\ell,t)$ and $\mathrm{x}_2(\ell,t)$ in Fig. 5.4. The total energy of the

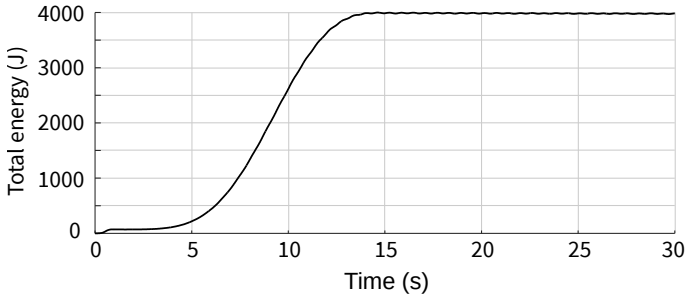

Figure 5.6: *Evolution of total energy of the rotating beam.*

beam shown in Fig. 5.6 grows smoothly for the first 15 s before attaining a constant value. The 's'-shaped curve of total energy in Fig. 5.6 is similar to, and a signature of, the prescribed angular velocity shown in Fig. 5.5(b). Further, the rate of angular momentum about the rotating center matches well with the total torque supplied to the rotor, as shown in Fig. 5.7. In the same figure, the $\hat{\boldsymbol{e}}_3$ components $\dot{h}_{03}$ and $\bar{m}_{03}$ of the angular momentum rate and the total external moment, respectively, grow and diminish in the initial 15 s. This phenomenon captures the profile of the prescribed angular acceleration shown in Fig. 5.5(b). Also, the small inertial oscillations of $\dot{h}_{03}$ in Fig. 5.7 are a signature of the beam's out-of-plane oscillations $\mathrm{x}_3(\ell,t)$ shown in Fig. 5.4. Thus, the energy and angular momentum rate in Figs. 5.6 and 5.7, respectively, capture the effects of the beam's rotational motion, and this demonstrates the accuracy of our computations.

5.1.5 Cable towing a lumped mass in 2D cross-flow

In this example, we compute the equilibrium solution of massless GE beam towing a lumped mass in cross-flow. Figure 5.8 shows the equilibrium shapes of massless beams of different diameters

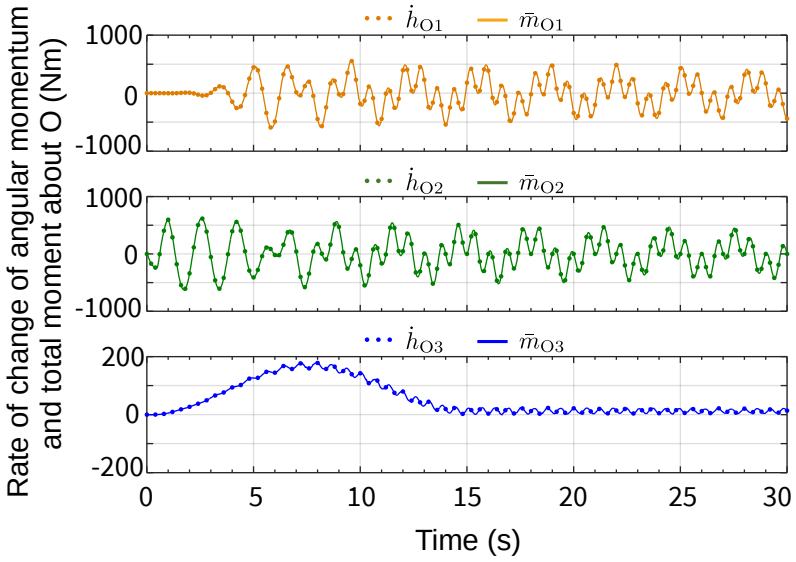

Figure 5.7: *Evolution of net rate of angular momentum $\dot{\boldsymbol{h}}_O$ and net external moment $\bar{\boldsymbol{m}}_O$ about O shows a decent match confirming that angular momentum is conserved.*

compared with the shape of a massless string by Glauert [1930], when these are subjected to a normal drag of 10 N/m in their reference states while towing a lumped mass of 20 kg which itself is subjected to a horizontal drag force of 10 N. The other properties of the beams are: $\ell = 1$ m and $E = G = 4 \times 10^9$ N/m^2. We note that as the diameter of the beam reduces the equilibrium shape approaches to that of the string. Figure 5.9 compares the equilibrium shapes of the 6 mm diameter beams with that of the string – all of which are subjected to same drag as above but tow a different lumped mass. We observe that the match between the beam and the string is best when the shapes have shallow curvatures, i.e. when the lumped mass is low (< 5 kg) or high (> 40 kg), while for other cases the match is good. The little difference in the curvatures is because the string doesn't resist bending moment.

5.2 Simulations with ring-shaped underslung load

In this section, we simulate some common hover conditions and flight maneuvers of cables towing ring-shaped underslung loads. Unlike the lumped mass model of underslung loads discussed in previous section, the complete 3D rigid-body model (Chap. 3) is considered in this section. However, the examples discussed here are only for the purpose of demonstrating: the steady state shapes of a cable while towing a lighter and a heavier mass, the time taken to achieve steady state in the cases of steady and accelerated flights at different speeds, the trajectory followed by the underslung load during maneuvers, and the optimum trajectory for keeping the ring as parallel to the ground as possible. Therefore, the physical parameters of the cable,

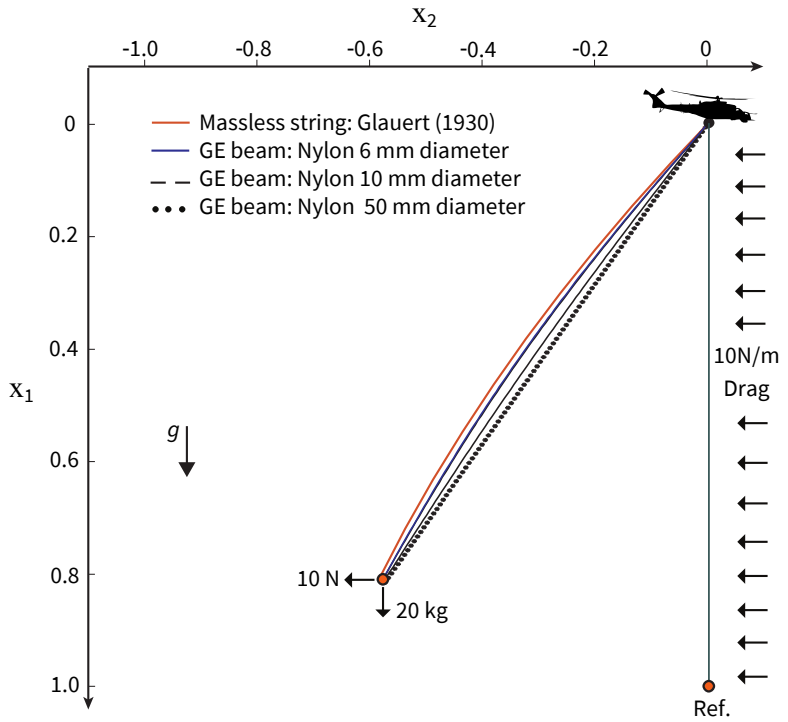

Figure 5.8: *Equilibrium shapes of massless nylon GE beams of different diameters towing a* 20 *kg mass and subjected to the same aerodynamic pressure (normal) drag are shown. They are compared with Glauert's solution for a massless-string which bears only tension. We find that the GE beam of* 6 *mm diameter is the best approximation to a string. Length of cable is* 1 *m. Nylon's elastic and shear moduli are* $E = G = 4$ *GPa.*

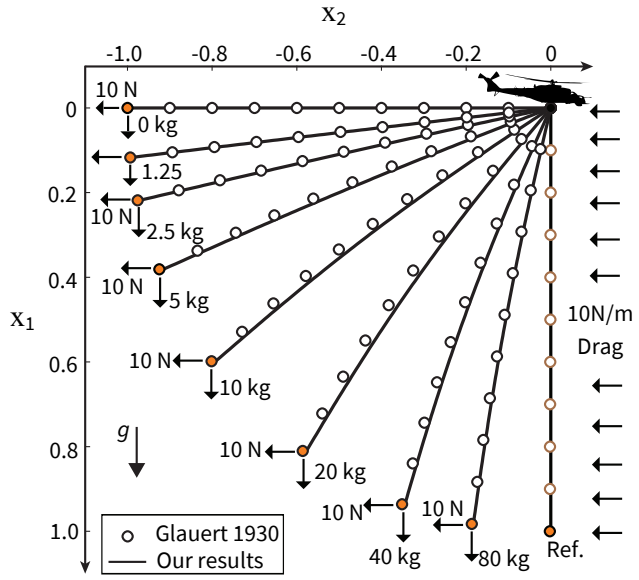

Figure 5.9: *Equilibrium shapes of massless GEBT (—) nylon cables towing various lumped masses, subjected to aerodynamic pressure (normal) drag are shown. They are compared with Glauert's (∘) massless-string which bears only tension. Length and diameter of cable are* 1 *m and* 6 *mm respectively. The normal drag on a vertical hanging (reference) cable is taken as* 10 *N/m, while that on the hanging mass is* 10 *N. Nylon's elastic and shear moduli are* $E = G = 4$ *GPa.*

underslung load, wind, helicopter motion, etc., are taken only for the purpose of illustrating these objectives. An example with much more practical values of physical parameters will be

discussed in Sec. 5.3.

For all the FE simulations considered here, the cable is discretized/meshed into $\mathrm{N} = 100$ linear elements and a time step of $\Delta t = 0.01$ s along with a numerical damping $\zeta = 10\text{-}20\%$, which is common for structural dynamics problems, is employed.

5.2.1 Hovering

We simulate a situation when the helicopter hovers at a fixed location, while the wind drags the cable and the underslung load as shown in Fig. 5.10. Following conditions are set for the simulation. Wind direction is 45^o in the X_2-X_3 plane and has a speed of 40 m/s. The Nylon Cable is 10 m long with circular cross-section of radius $r = 1$ cm, while the underslung load of 10 kg is smaller in dimension, as shown in the inset (zoomed-in view) of Fig. 5.10. It has a mean radius $r^* = 8$ cm, sectional radius $r^*_{\mathrm{cs}} = 0.25$ cm and the distance between its center and the point of attachment $\ell^* = 0.8$ m. The von Karman coefficient $\mathrm{c_K} = 0.6$, while the drag coefficients $\mathrm{c}_n = 1.3$ and $\mathrm{c}_t = 0$ (all dimensionless). The steady state is achieved in the underslung load's displacement and angular displacement after aerodynamically damped oscillations for 50 s, as shown in Fig. 5.11. The x^*_2 and x^*_3 components of displacement $\boldsymbol{x}^*$ in Fig. 5.11(a) are equal because the direction of wind is 45^{o} in X_2-X_3 plane, as shown in Fig. 5.10. For the same reason the φ^*_2 and φ^*_3 components of angular displacement $\boldsymbol{\varphi}^*$ in Fig. 5.11(b) are equal and opposite, which can also be verified from the orientation of the ring in the inset of Fig. 5.10. The steady state shape of the cable is significantly curved, as shown in Fig. 5.10, due to the aerodynamic drag, as well as the weight of the underslung load.

5.2.2 Steady forward flight

The steady flight may be simulated as a special case of hover (Sec. 5.2.1) by taking the relative wind velocity as $\boldsymbol{v}_{\mathrm{air}} - \dot{\boldsymbol{u}}_0$. We will discuss a more general forward flight that starts from rest in the next section.

In contrast to the previous example, we consider a low relative wind velocity of $\boldsymbol{v}_{\mathrm{air}} - \dot{\boldsymbol{u}}_0 = -5\hat{\boldsymbol{e}}_2 - 20\hat{\boldsymbol{e}}_2 = -25\hat{\boldsymbol{e}}_2$ m/s acting on the towed system, where the wind velocity $\boldsymbol{v}_{\mathrm{air}}$ is purely along the $-\hat{\boldsymbol{e}}_2$ direction unlike oriented 45^{o} to it. Moreover, the underslung load of 50 kg is heavier and the ring of $r^*_{\mathrm{cs}} = 0.05$ m and $r^* = \ell^* = 1$ m is larger, while the 10 m long nylon cable with cross-sectional radius $r = 0.5$ cm is thinner than earlier. Thus, we may expect more aerodynamic drag on the ring and less on the cable in comparison to the previous example. Figures 5.12 and 5.13, respectively, show the steady state of the cable and the evolution of linear

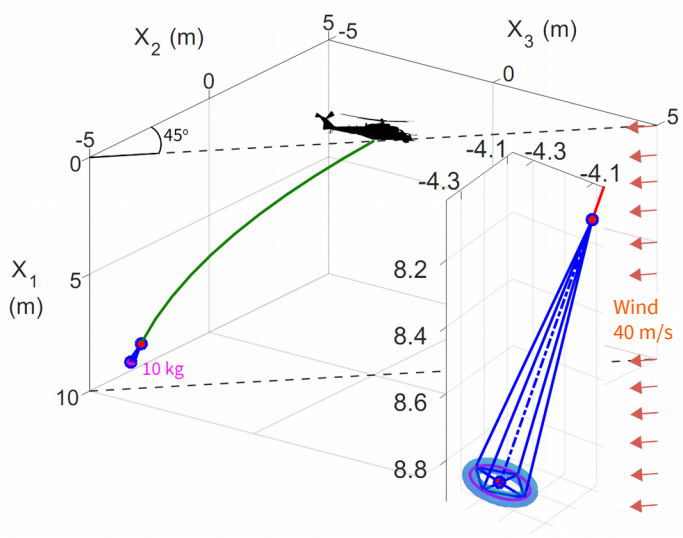

Figure 5.10: *FE solution at the end of* 50 *s when steady state is achieved. The orientation of the ring (detector) at steady state is shown in the right inset zoomed-in view of the underslung load. Note that, although a detailed structure of the underslung load is shown with the ring detector connected to the cable via rigid links, the FE model of the underslung load assumes no contribution from links, as discussed in Chap. 3.*

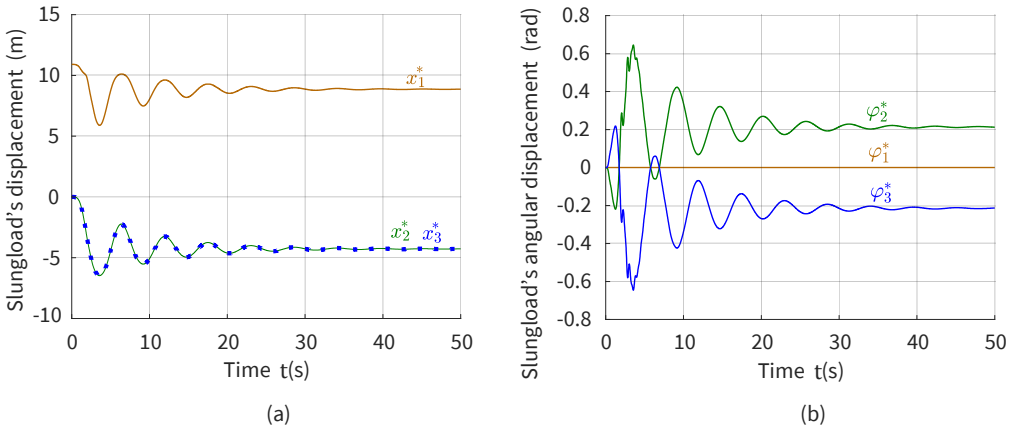

Figure 5.11: *Time evolution of* $(\mathbf{a})$ *displacement and* $(\mathbf{b})$ *angular displacement of the small underslung load during hover.*

($\boldsymbol{x}^*$) and angular ($\boldsymbol{\varphi}^*$) displacements of the underslung load. Contrasting Fig. 5.13 with Fig. 5.11, we note that since the drag on the underslung load is more due to its large size, the underslung load displaces (x_1^* and x_2^*) farther, and tilts (φ_3^*) more, than before despite being subjected to a lower wind velocity. However, the initial oscillations damp out quickly and the steady state is achieved faster in Fig. 5.13 than in Fig. 5.11. This is also because the weight and the aerodynamic damping of the underslung load are more. Thus, the resulting shape of the cable is less curved (almost straight) in Fig. 5.12 than in Fig. 5.10.

When the wind velocity is increased to 40 m/s in $-\hat{e}_2$ direction, the same underslung load displaces even farther and almost aligns with the wind direction as shown in Figs. 5.14 and

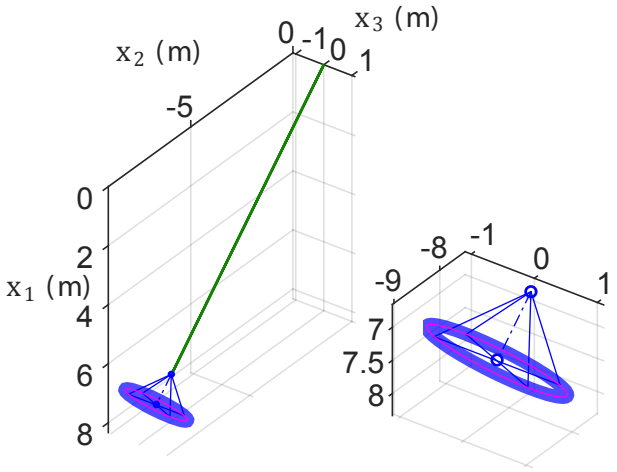

Figure 5.12: *FE solution at the end of* 100 *s when steady state has already been achieved is shown on the left, while the underslung load's orientation is shown by a zoomed-in view on the right.*

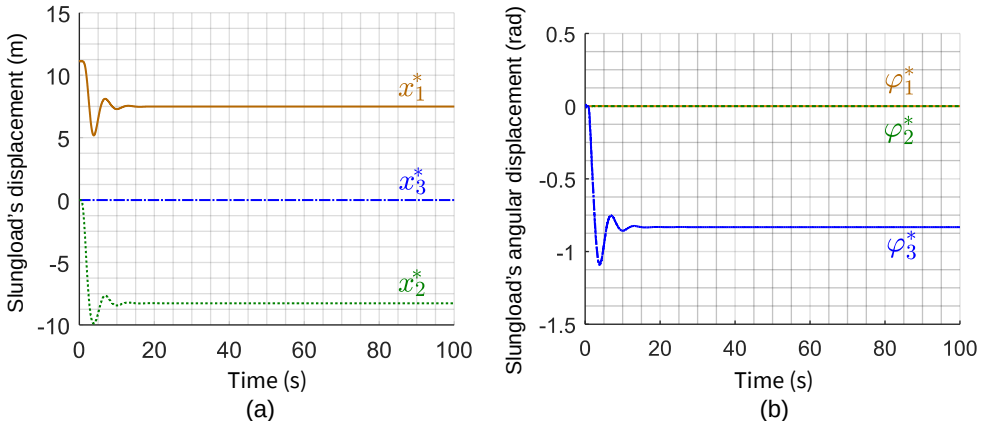

Figure 5.13: *Time evolution of* $(\mathbf{a})$ *displacement and* $(\mathbf{b})$ *angular displacement of the underslung load during* $-25\hat{e}_2$ *m/s steady forward flight.*

5.15, while the shape of the cable is nearly straight. The evolution of displacements is shown in Fig. 5.15. Note that since the higher wind velocity causes more damping, the displacements Fig. 5.15(a) and angular displacements Fig. 5.15(b) achieve steady state much faster in this case. It is clear from the above two examples that the given velocities of steady forward flight are not helpful in keeping the given ring detector (underslung load) parallel to the ground as desired for surveying. Perhaps a much smooth transition from zero to slightly lower velocity than considered above is better for keeping the same ring parallel to ground. To investigate this speculation, we simulate a forward flight that slowly accelerates from rest and gradually attains a lower constant velocity.

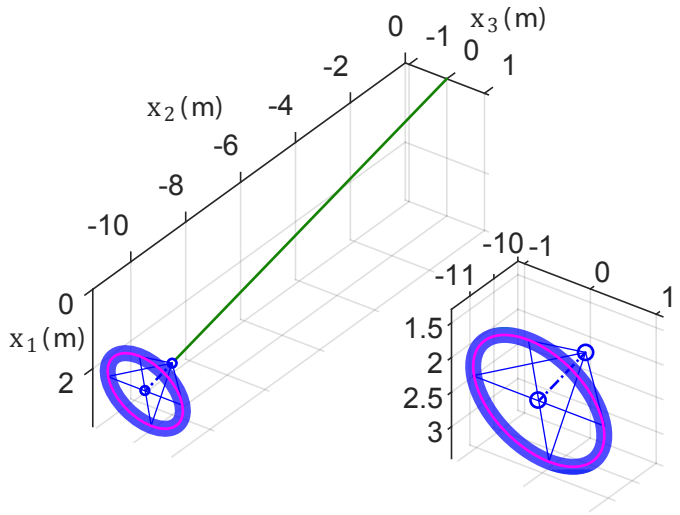

Figure 5.14: *FE solution for relative wind speed* 40 *m/s at the end of* 100 *s when steady state has already been achieved is shown on the left, while the underslung load's orientation is shown by a zoomed-in view on the right.*

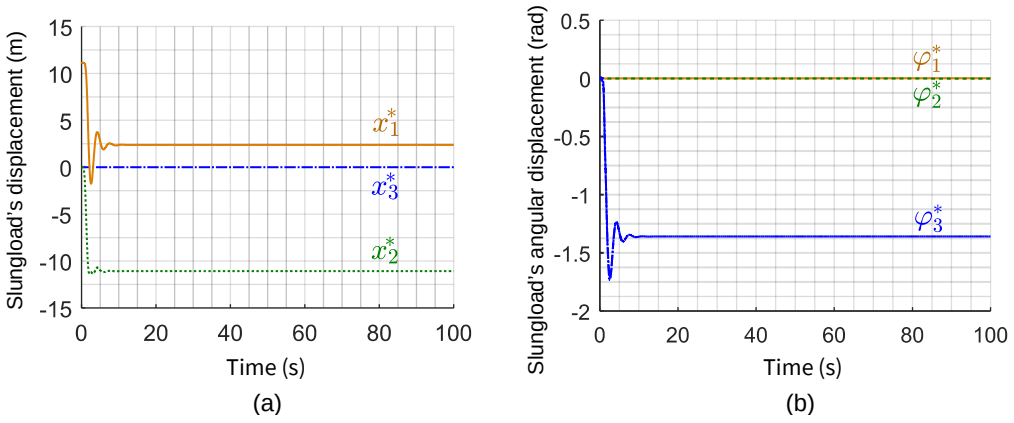

Figure 5.15: *Time evolution of* $(\mathbf{a})$ *displacement and* $(\mathbf{b})$ *angular displacement of the underslung load during* $-40\hat{\boldsymbol{e}}_2$ *m/s steady forward flight.*

5.2.3 General forward flight

In this section, we simulate the dynamics of towed system during a general forward flight that starts from rest and attains a constant velocity after a desired time. The helicopter towed detector often needs to survey a long patch of area while maintaining a desired velocity. We expect to maintain a lower constant velocity for the same cable-underslung load system discussed in the previous section. For example, the helicopter starts from rest at $t = 0$ s and then travels after 20 s at a velocity of (say) 8 m/s in the $\hat{\boldsymbol{e}}_2$ direction when the wind blows at $-5\hat{\boldsymbol{e}}_2$ m/s. So the relative wind velocity on the system after achieving this constant speed is $-13\hat{\boldsymbol{e}}_2$ m/s, which is nearly half of that considered in the first example of Sec. 5.2.2. To this end, we prescribe the

following condition on the velocity:

$$\dot{\boldsymbol{u}}_0(t) = \begin{cases} \mathbf{0} \text{ m/s} & \text{if } t = 0 \text{ s}, \\ 8\,\hat{\boldsymbol{e}}_2 \text{ m/s} & \text{if } t > 20 \text{ s}. \end{cases} \tag{5.2.1}$$

To satisfy the above conditions while ensuring that the motion is smooth until the desired velocity is attained, we approximate the velocity

$$\dot{\boldsymbol{u}}_0(t) = \frac{\operatorname{erf}(12) - \operatorname{erf}(6 - 1.5\,t^{0.6})}{2}\, 8\,\hat{\boldsymbol{e}}_2 \text{ m/s}, \tag{5.2.2}$$

where Abramowitz et al. [1964] define the function

$$\operatorname{erf}(z) := \frac{2}{\sqrt{\pi}} \int_0^z \exp(-\tau^2)\, d\tau.$$

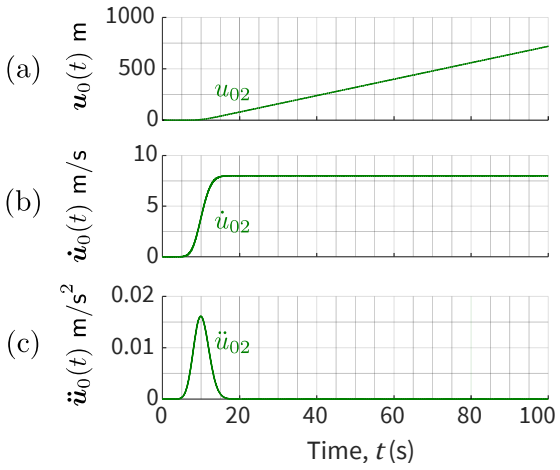

Figure 5.16: (**a**) *Displacement,* (**b**) *velocity and* (**c**) *acceleration of the surveying helicopter for the proposed forward flight in the* $\hat{\boldsymbol{e}}_2$ *direction is shown. The constant velocity of* 8 *m/s is achieved after* 40 *s starting from rest.*

Figure 5.16 plots the desired displacement, velocity and acceleration for the forward flight as functions of time using (5.2.2). Note that when the velocity $\dot{\boldsymbol{u}}_0(t) = 8\,\hat{\boldsymbol{e}}_2$ m/s is constant for $t > 20$s, the displacement $\boldsymbol{u}_0(t) = 8t\,\hat{\boldsymbol{e}}_2$ m grows linearly and the acceleration $\ddot{\boldsymbol{u}}_0(t)$ vanishes, as desired. Also note that, there is no special reason for choosing (5.2.2) than to have a smoothly rising and settling function, commonly known as *sigmoid* function. However, instead of one sigmoid function we may simply choose piecewise smooth polynomials, and this will be demonstrated in the next section where we design trajectories for maneuvers.

For now, we simulate the flight conditions (5.2.2) on the cable and underslung load system of Sec. 5.2.2, subjected to a $-5\hat{\boldsymbol{e}}_2$ m/s wind. The steady state of the system is shown in Fig. 5.17. In

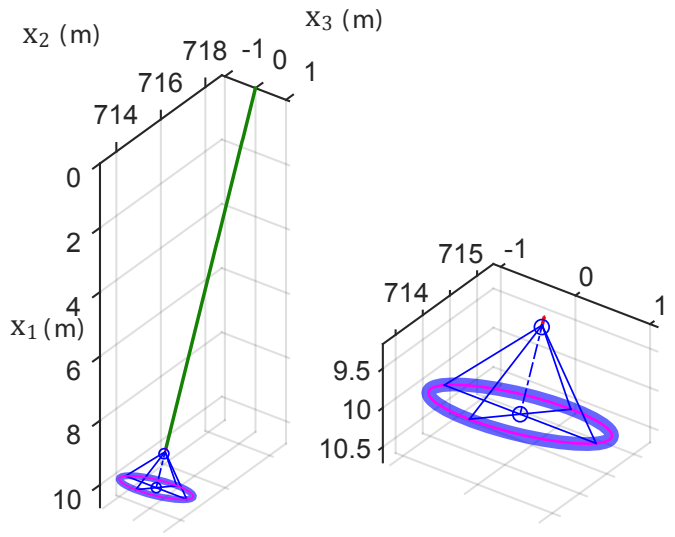

Figure 5.17: *FE solution of forward flight at the end of* 100 *s, when steady state has already been achieved. The inset zoomed-in view of the underslung load is shown on the right.*

contrast to Sec. 5.2.2, the relative wind velocity of $-13\hat{e}_2$ m/s experienced by the system is lower, which causes the underslung load to displace less.

Contrasting the actual displacement of the underslung load with the helicopter's trajectory in Fig. 5.18, we note that the underslung load follows the trajectory of the helicopter closely with negligible variation. The small initial oscillations of x_3^* in Fig. 5.18(c) are due to the von Karman effect, and it damps out when the steady velocity is achieved.

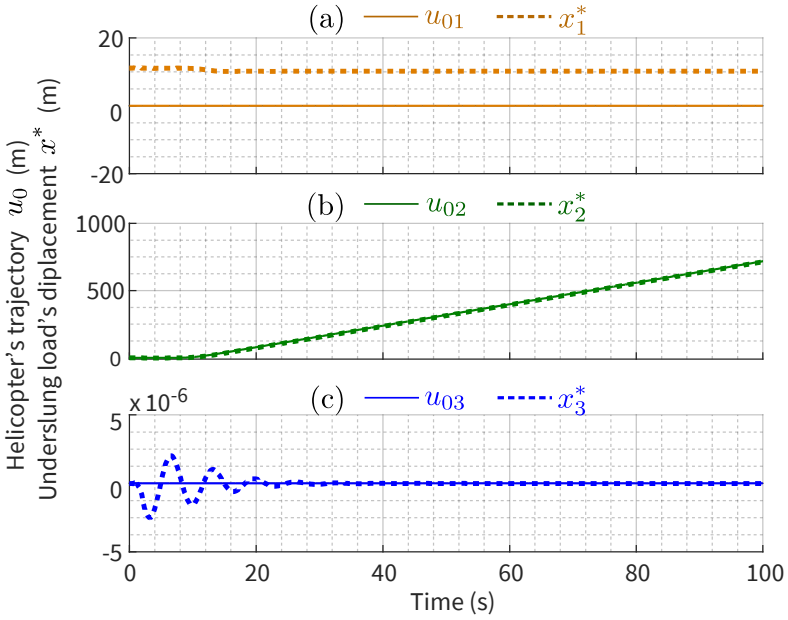

Figure 5.18: *Displacement of the underslung load contrasted with the helicopter's trajectory during a forward flight of* 8 *m/s.*

Further, the steady state angular displacement of the underslung load is small ($\varphi_3^* \approx -0.4$ rad) in Fig. 5.19 in contrast to Fig. 5.13(b), which implies that the ring detector remains less tilted to the ground/surveying plane. This facilitates better operation for a long period of time at this cruising speed.

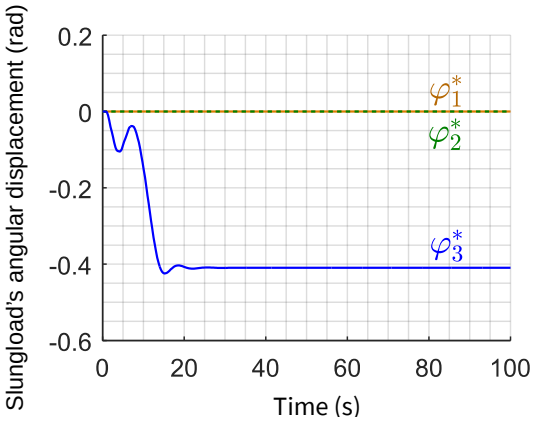

Figure 5.19: *Time evolution of angular displacement of the underslung load during a forward flight of* 8 *m/s that starts from rest.*

5.2.4 U-turn maneuver

In this section, we simulate the dynamics of towed system during a 'U' turn maneuver. Such a maneuver may be undertaken by the surveying helicopter for changing to a parallel lane. In

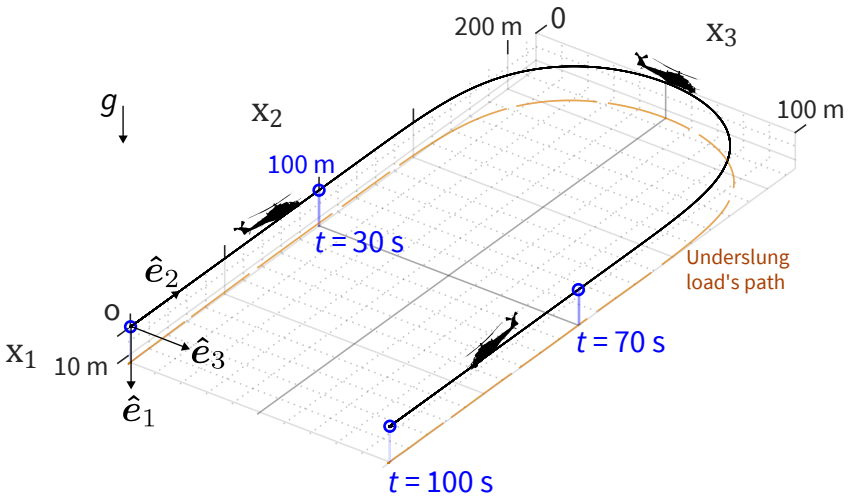

Figure 5.20: *Trajectory of the surveying helicopter for the proposed U-turn maneuver is shown. The actual path of the underslung load is shown with broken line.*

the following example, we expect the helicopter to start from rest at $t = 0$ s and then follow a

trajectory (Fig. 5.20) which obeys the following conditions at various times:

$$\boldsymbol{u}_0(t) = \begin{cases} \mathbf{0} & \text{if } t = 0 \text{ s}, \\ 100\hat{\boldsymbol{e}}_2 \text{ m} & \text{if } t = 30 \text{ s}, \\ 100\,(\hat{\boldsymbol{e}}_2 + \hat{\boldsymbol{e}}_3) \text{ m} & \text{if } t = 70 \text{ s}, \\ 100\hat{\boldsymbol{e}}_3 \text{ m} & \text{if } t = 100 \text{ s}, \end{cases}, \; \dot{\boldsymbol{u}}_0(t) = \begin{cases} \mathbf{0} \text{ m/s} & \text{if } t = 0 \text{ s}, \\ 6\hat{\boldsymbol{e}}_2 \text{ m/s} & \text{if } t = 30 \text{ s}, \\ -6\hat{\boldsymbol{e}}_2 \text{ m/s} & \text{if } t = 70 \text{ s}, \\ \mathbf{0} \text{ m/s} & \text{if } t = 100 \text{ s} \end{cases} \tag{5.2.3}$$

and

$$\ddot{\boldsymbol{u}}_0(t) = \mathbf{0} \;\; \text{if } t = 0, 30, 70 \text{ and } 100 \text{ s}.$$

To satisfy (5.2.3), the entire trajectory $\boldsymbol{u}_0(t)$ is then approximated by the following combination of smooth polynomials:

$$\boldsymbol{u}_0(t) = \begin{cases} \left(\dfrac{7\,t^3}{675} - \dfrac{t^4}{3375} + \dfrac{t^5}{405000}\right)\hat{\boldsymbol{e}}_2 & \text{if } 0 \le t \le 30 \text{ s}, \\ \left(\dfrac{9703589}{236} - \dfrac{1020973\,t}{84} + \dfrac{2330461\,t^2}{1439} - \dfrac{406546\,t^3}{3163} \right. \\ \quad + \dfrac{69323\,t^4}{10250} - \dfrac{24350\,t^5}{98059} + \dfrac{1909\,t^6}{292879} - \dfrac{88\,t^7}{714447} \\ \quad \left. + \dfrac{27\,t^8}{16237985}\right)\hat{\boldsymbol{e}}_2 + \left(-\dfrac{31791879}{65} + \dfrac{19035877\,t}{124} \right. \\ \quad - \dfrac{2719411\,t^2}{124} + \dfrac{839599\,t^3}{445} - \dfrac{290133\,t^4}{2662} + \dfrac{119078\,t^5}{26689} \\ \quad \left. - \dfrac{5991\,t^6}{45011} + \dfrac{1243\,t^7}{424393} - \dfrac{215\,t^8}{4522888}\right)\hat{\boldsymbol{e}}_3 & \text{if } 30 \text{ s} < t \le 70 \text{ s}, \\ \left(\dfrac{440000}{81} - \dfrac{29200\,t}{81} + \dfrac{812\,t^2}{81} - \dfrac{281\,t^3}{2025} \right. \\ \quad \left. + \dfrac{19\,t^4}{20250} - \dfrac{t^5}{405000}\right)\hat{\boldsymbol{e}}_2 + 100\hat{\boldsymbol{e}}_3 & \text{if } 70 \text{ s} < t \le 100 \text{ s}, \end{cases} \tag{5.2.4}$$

where we have also assumed that the helicopter comes to a halt at the four intermediate time junctions, i.e. the higher derivatives of acceleration $d\ddot{\boldsymbol{u}}_0/dt$ (jerk) and $d^2\ddot{\boldsymbol{u}}_0/dt^2$ (snap) are also zero at these times. This assumption, in addition to (5.2.3), provided the necessary number of conditions for computing all the coefficients of the polynomials finally arrived at in (5.2.4).

We investigate the same cable and underslung load system of Sec. 5.2.3 for this maneuver. Comparing underslung load's displacements with the helicopter's trajectory (5.2.4) in Fig. 5.21, we note that the underslung load closely follows the desired trajectory.

Figure 5.22 plots the evolution of the underslung load's angular displacement in time. Note that the system here is subjected to slightly lesser relative wind speed ($\le$ 12 m/s) than the

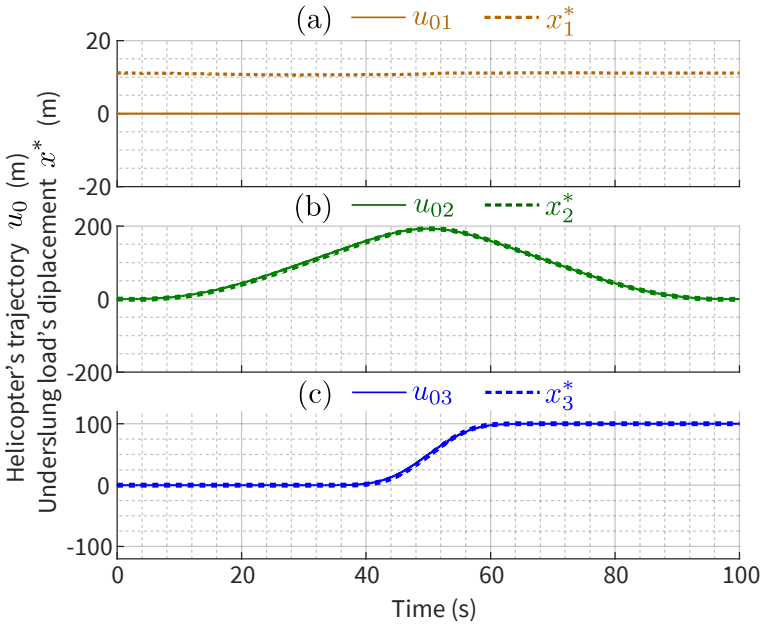

Figure 5.21: *Displacement of the underslung load contrasted with the helicopter's trajectory during a U-turn maneuver of* 6 *m/s initial turn velocity.*

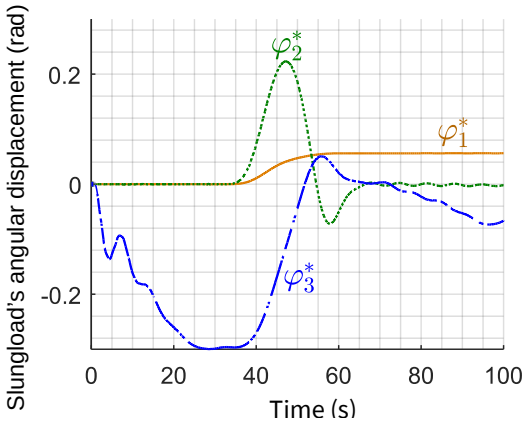

Figure 5.22: *Time evolution of angular displacement of the underslung load during U-turn maneuver of* 6 *m/s initial turn velocity.*

forward flight (13 m/s) simulation of previous section. Therefore, the angular displacement of the mineral detector is lower ($< \pm 0.3$ rad), keeping it nearly parallel to the ground for most of the time. When the helicopter finally stops at $t = 100$ s, the underslung load is parallel to the ground as shown by the zoomed-in view (inset) of Fig. 5.23.

5.2.5 U-turn maneuver without intermediate halts

As discussed in the previous section, the assumption of zero derivatives of acceleration in the above method required the helicopter to come to halt at each intermediate time junction; see

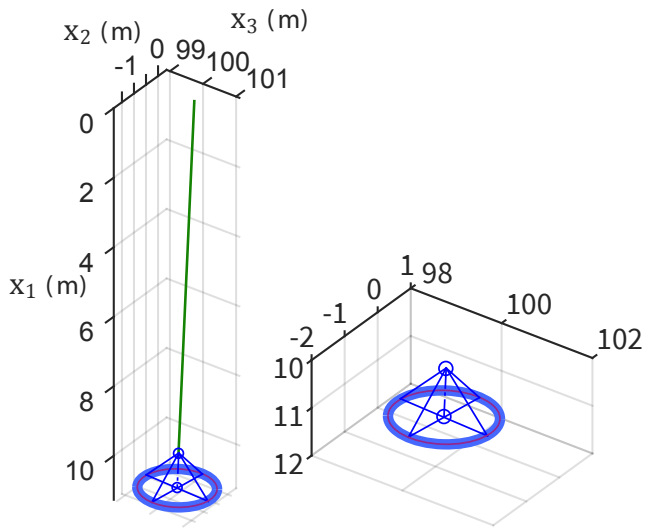

Figure 5.23: *FE solution at the end of* 100 *s when the helicopter has come to rest. The underslung load is almost parallel to the ground, i.e. the* $\hat{\boldsymbol{e}}_2$*-*$\hat{\boldsymbol{e}}_3$ *plane, as shown in the zoomed view (right).*

(5.2.3) and Fig. 5.20. Such a trajectory is inefficient for practical maneuvering situations. It is often desired to have a trajectory with smooth transitions through the intermediate junctions.

To this end, we set up the following minimization problem to obtain a trajectory that starts from rest, passes through the desired junctions (5.2.3) and has minimum snap (second derivative of acceleration) throughout the journey:

$$\min \int_0^{100\text{ s}} \frac{d^2\ddot{\boldsymbol{u}}_0}{dt^2} \cdot \frac{d^2\ddot{\boldsymbol{u}}_0}{dt^2}\, dt, \tag{5.2.5a}$$

subject to

$$\boldsymbol{u}_0(t) = \begin{cases} \boldsymbol{0}\text{ m} & \text{if } t = 0\text{ s}, \\ 100\hat{\boldsymbol{e}}_2\text{ m} & \text{if } t = 30\text{ s}, \\ 100\,(\hat{\boldsymbol{e}}_2 + \hat{\boldsymbol{e}}_3)\text{ m} & \text{if } t = 70\text{ s}, \\ 100\hat{\boldsymbol{e}}_3\text{ m} & \text{if } t = 100\text{ s}, \end{cases}, \tag{5.2.5b}$$

and

$$\dot{\boldsymbol{u}}_0 = \ddot{\boldsymbol{u}}_0 = \boldsymbol{0} \;\text{ if } t = 0 \text{ or } 100\text{ s}. \tag{5.2.5c}$$

The resulting trajectory of the helicopter, along with its velocity and acceleration, is plotted in Fig. 5.24.

The angular displacement of the underslung load during this maneuver is shown in Fig. 5.25. These grow initially, then drop down and remain small within ± 0.1 rad. Thus, the underslung load remains nearly parallel to the ground in the later half of the journey, i.e. for $t > 50$ s.

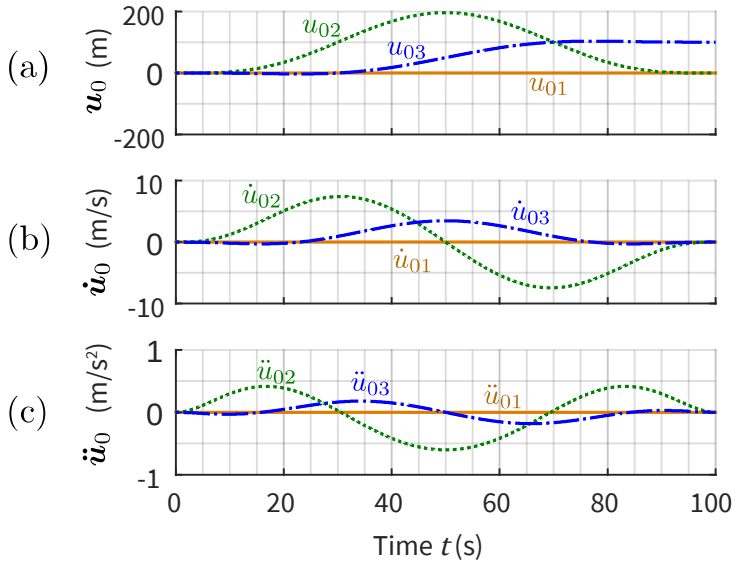

Figure 5.24: *Time evolution of* (a) *displacement,* (b) *velocity and* (c) *acceleration of the helicopter during minimum snap U-turn maneuver.*

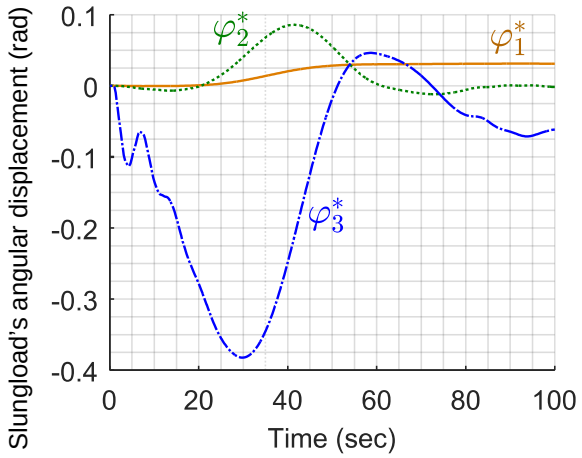

Figure 5.25: *Time evolution of angular displacement of the underslung load, when the trajectory which has minimum snap is chosen. The velocity before turning is* 7.423 *m/s.*

The actual path (displacement) of the underslung load is contrasted with the helicopter's trajectory in Fig. 5.26, and we note that these nearly coincide.

In contrast to the low initial turning speed of 6 m/s in the previous U-turn trajectory (Fig. 5.21), we require a higher speed of 7.423 m/s for this maneuver.

Further, for a different trajectory with the same turning speed of 7.423 m/s, but assuming intermediate stoppage conditions (5.2.3) instead of minimum snap condition (5.2.5), results in the underslung load taking a slightly longer U-turn — compare x_2^* in Figs. 5.27 and 5.26 — with

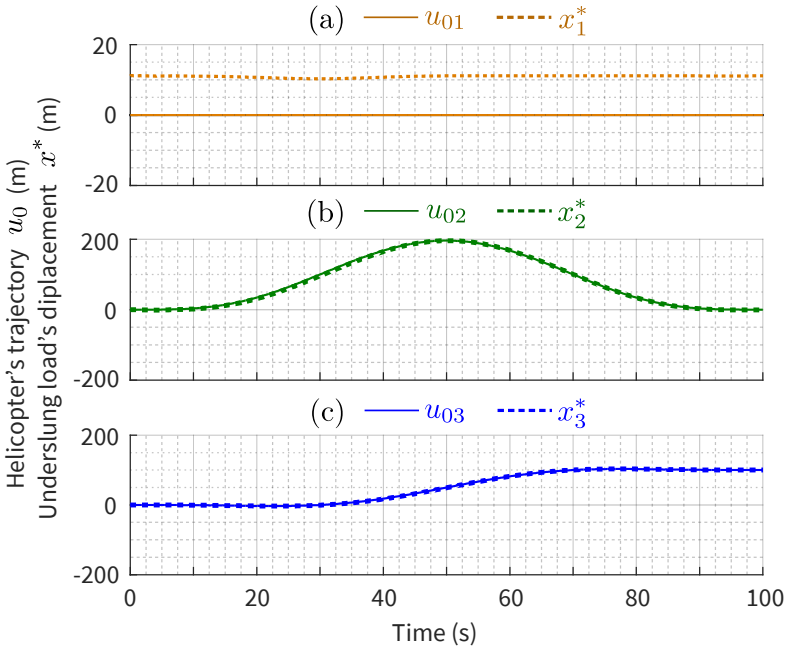

Figure 5.26: *Displacement of the underslung load contrasted with the helicopter's trajectory during a minimum snap U-turn maneuver.*

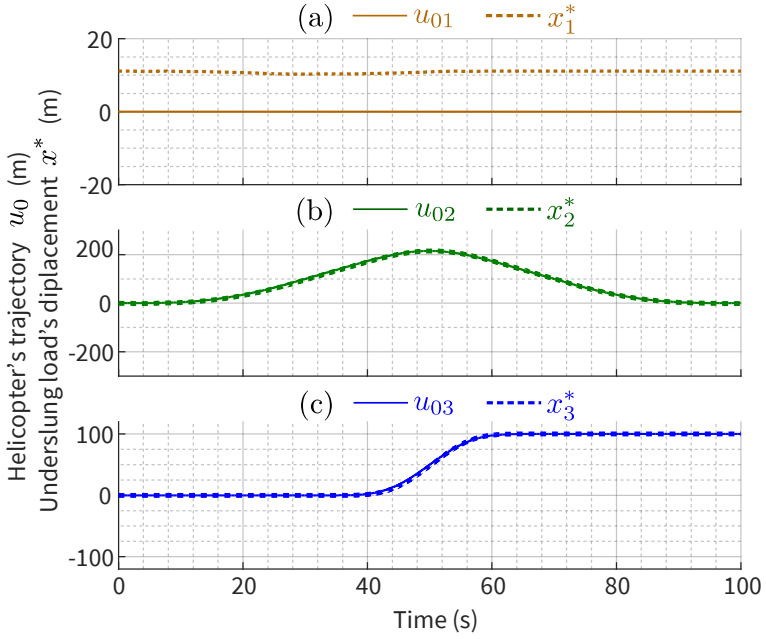

Figure 5.27: *Displacement of the underslung load contrasted with the helicopter's trajectory during a U-turn maneuver of* 7.423 *m/s initial turn velocity.*

larger angular displacement — compare φ_2^* in Figs. 5.28 and 5.25.

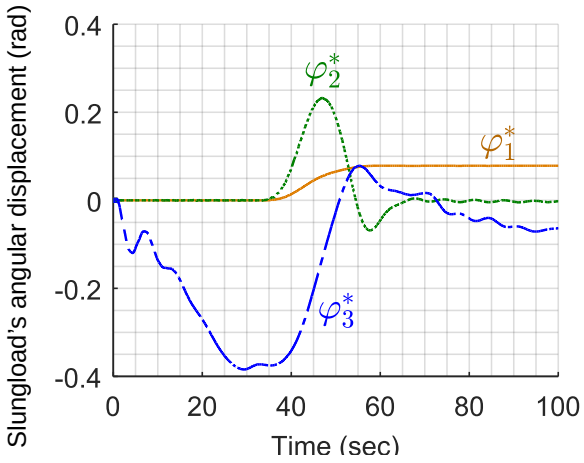

Figure 5.28: *Time evolution of angular displacement of the underslung load, for the case when the velocity before turning is* 7.423 *m/s.*

5.2.6 Round maneuver

In this section, we simulate the dynamics of towed system during a 'round' turn maneuver. Such a maneuver may be undertaken by the helicopter for surveying a circular patch and returning to the starting point.

In the following example, we expect the helicopter to start from rest at $t = 0$ s and then follow a trajectory (Fig. 5.31) which obeys the following conditions at various times:

$$\boldsymbol{u}_0(t) = \begin{cases} \mathbf{0} & \text{if } t = 0 \text{ s}, \\ 100\,(\hat{\boldsymbol{e}}_2 - \hat{\boldsymbol{e}}_3) & \text{if } t = 30 \text{ s}, \\ 100\,(\hat{\boldsymbol{e}}_2 + \hat{\boldsymbol{e}}_3) & \text{if } t = 70 \text{ s}, \\ \mathbf{0} & \text{if } t = 100 \text{ s} \end{cases} \tag{5.2.6a}$$

and

$$\dot{\boldsymbol{u}}_0 = \ddot{\boldsymbol{u}}_0 = \mathbf{0} \;\text{ if } t = 0 \text{ or } 100 \text{ s}. \tag{5.2.6b}$$

Using the conditions (5.2.6) along with (5.2.5a) we design a minimum snap trajectory. The motion starts from rest with zero velocity and zero acceleration as shown in Fig. 5.29, passing smoothly through the desired intermediate time junctions.

In Fig. 5.30, we plot the angular displacement of the underslung load during the round maneuver. These are smooth and small ($\leq \pm 0.4$ rad) as shown in Fig. 5.30, thus, keeping the underslung load (mineral detector) almost parallel to the ground ($\hat{\boldsymbol{e}}_2$-$\hat{\boldsymbol{e}}_3$ plane) as desired for proper surveying.

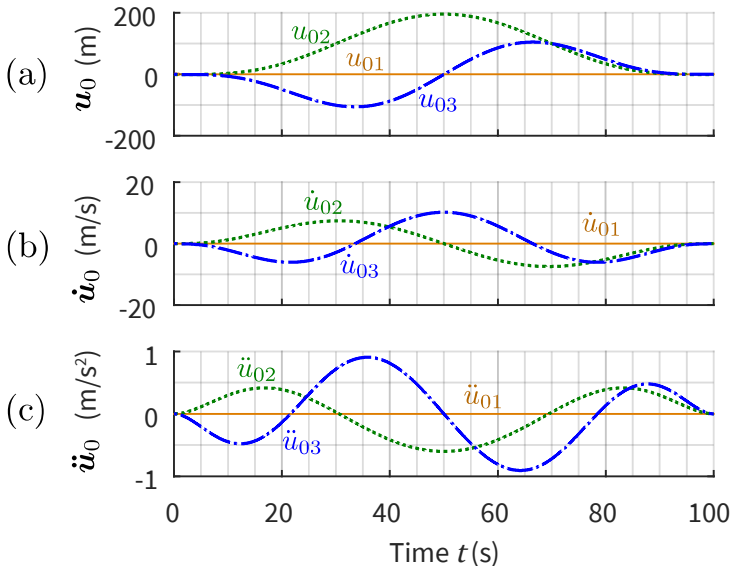

Figure 5.29: *Time evolution of* (a) *displacement,* (b) *velocity and* (c) *acceleration of the helicopter for the round maneuver.*

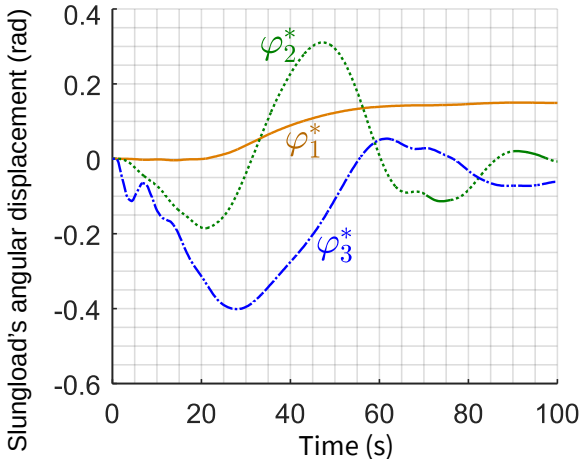

Figure 5.30: *Time evolution of angular displacement of the underslung load during round maneuver.*

The resulting in trajectory of the helicopter and the underslung load are shown in Fig. 5.31.

The displacements of the underslung load shown in Fig. 5.32 are smooth. We also note that the underslung load starts and comes to a halt together with the helicopter while closely following its trajectory.

5.3 Realistic cable-underslung load system

In this section, we simulate using values that are representative of an actual TDEM system. For the forward flight, the cruising speed of 27.8 m/s ($\approx$ 50 knots) is used [Lahiri et al., 2012]. For the U-turn and round maneuvers, we employ the flight trajectories and conditions computed

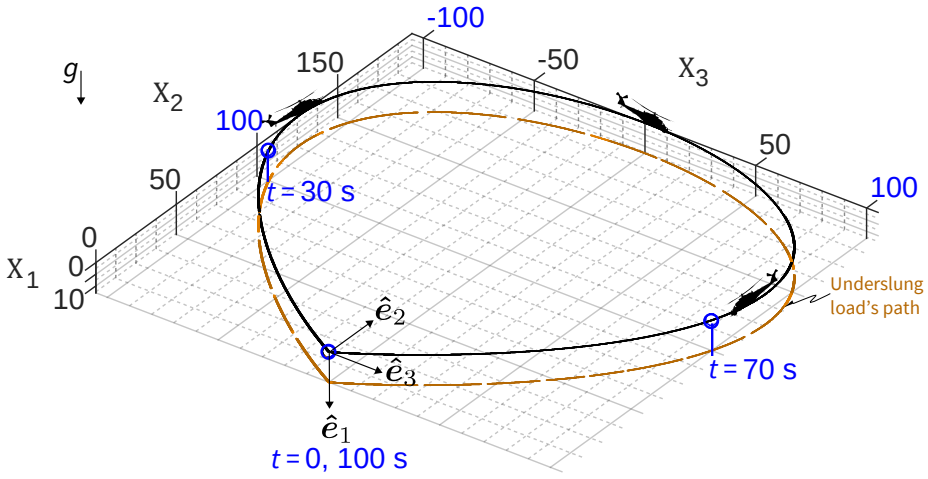

Figure 5.31: *Trajectory of the surveying helicopter for the proposed 'round' maneuver is shown. The actual path of the underslung load is shown with broken line.*

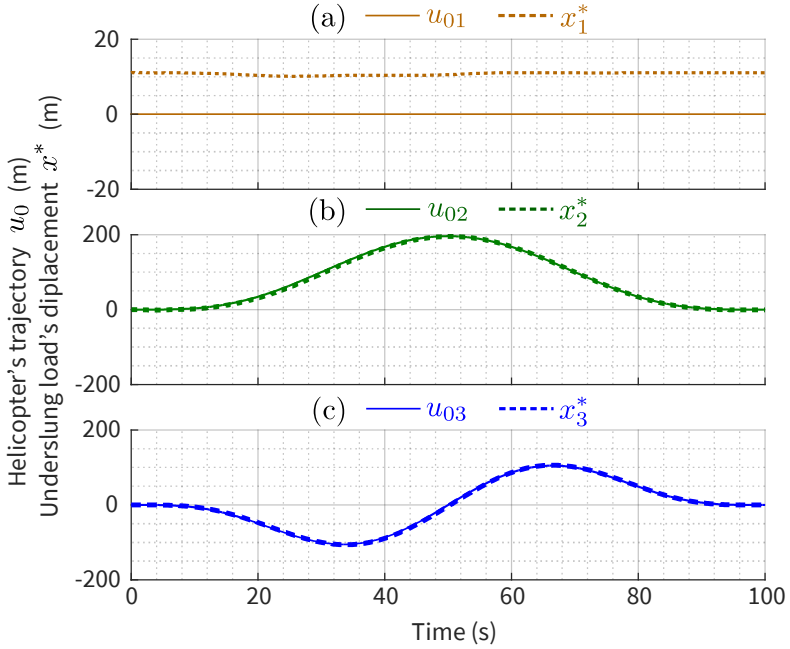

Figure 5.32: *Displacement of the underslung load contrasted with the helicopter's trajectory during a minimum snap round maneuver.*

in Secs. 5.2.5 and 5.2.6 by using the minimum snap criterion (5.2.5a). The following system configuration is obtained from Lahiri et al. [2012] and then projected on/recomputed for our model.

A $\ell = 14$ m long cable with cross-sectional radius $r = 0.004$ m is towing a 435 kg underslung load as shown in Fig. 1.7. Their underslung load is a complex structure with three concentric rings (polygon housings) connected by several links. The vertical distance from the

ring's center to the point of attachment on the cable is given as $\ell^* = 16$ m. Lahiri et al. [2012] modeled the cable and the links as massless members which bear only tension. The links are of different lengths to provide an initial tilt to the underslung load.

Here, we assume that the underslung load is a simple ring-like structure as shown in Fig. 3.2, while the cable is a flexible GE beam made of nylon as discussed in Chap. 2. Note from Chap. 3 that our model assumes that the massless links bear no drag and are of the same length, which keeps the ring initially parallel to the ground. Since Lahiri et al. [2012] do not provide the thickness/cross-sectional radius of the ring, we estimate it as follows. The total drag acting on their structure with outermost ring's radius 11 m for a 25.74 m/s downwash (downward airflow from the helicopter rotor) was reported as 5051.74 N in the case of hover. Assuming that the same total drag force acts normally on a single ring (our model) with radius $r^* = 11$ m and drag coefficient $c_n \approx 1.2$, without affecting the links, we deduce the ring's cross-sectional radius to be $r^*_{cs} \approx 0.07$ m.

A general forward flight with cruise velocity $\dot{u}_{02}(t > 20\text{ s}) = 27.8$ m/s instead of 6 m/s in (5.2.2) is simulated with the above data: (1) under no wind conditions and ignoring the von Karman effect as in Lahiri et al. [2012], and (2) under a more realistic situation with $\boldsymbol{v}_{air} = -5\hat{\boldsymbol{e}}_2$ m/s and von Karman coefficient $c_K = 0.6$. Additionally, we assume no downwash from the helicopter on the ring as our underslung load is a large ring, whereas the downwash will only be effective over a small central part, as its diameter decreases away from the rotor [Venkatesan, 2014]. The steady state configuration at the end of 100 s for (1) no wind condition is shown in Fig. 5.33(a), where the cable is nearly straight and the underslung load is inclined to the ground.

The angular displacement at $t = 100$ s is $\varphi^*_3 \approx -0.75$ rad (-43^o) as shown in Fig. 5.33(b).

The trajectory followed by the underslung load is contrasted with that of the helicopter in Fig. 5.34.

The steady state configuration at the end of 100 s for case (2) when there is a wind with velocity $-5\hat{\boldsymbol{e}}_2$ m/s is shown in Fig. 5.35(a).

The cable is nearly straight and the underslung load is inclined to the ground at an angle $\varphi^*_3 \approx -0.9$ rad (-51^o) as shown in Fig. 5.35(b).

The trajectory followed by the underslung load in this case is contrasted with that of the helicopter in Fig. 5.36.

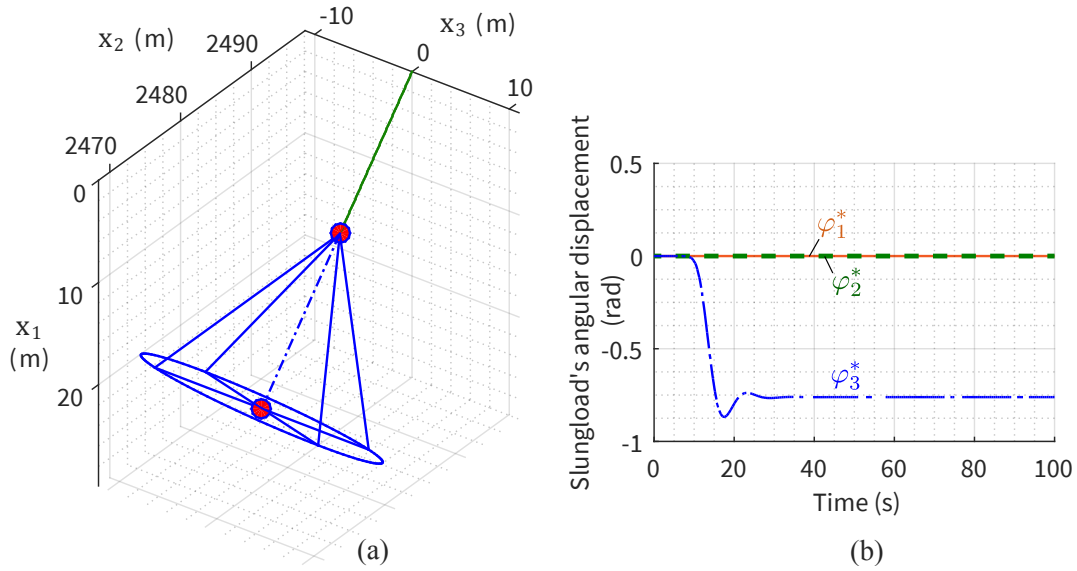

Figure 5.33: (**a**) *Steady state at the end of* 100 *s and* (**b**) *angular displacement of the underslung load for* 27.8 *m/s forward flight under no wind condition.*

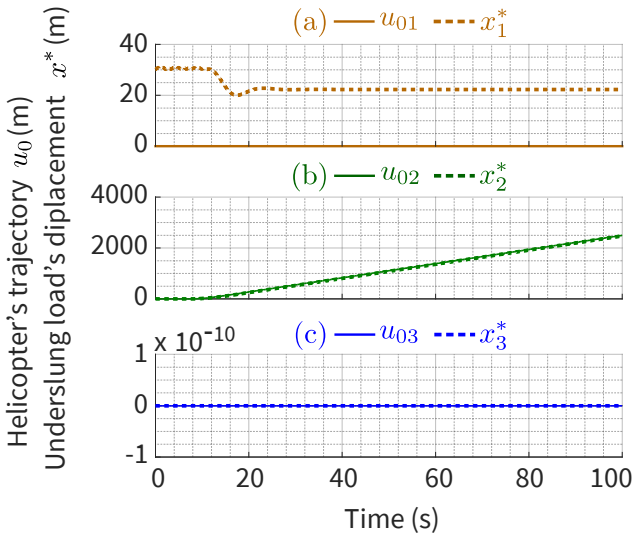

Figure 5.34: *Displacement of the underslung load contrasted with the helicopter's trajectory during* 27.8 *m/s forward flight under no wind condition.*

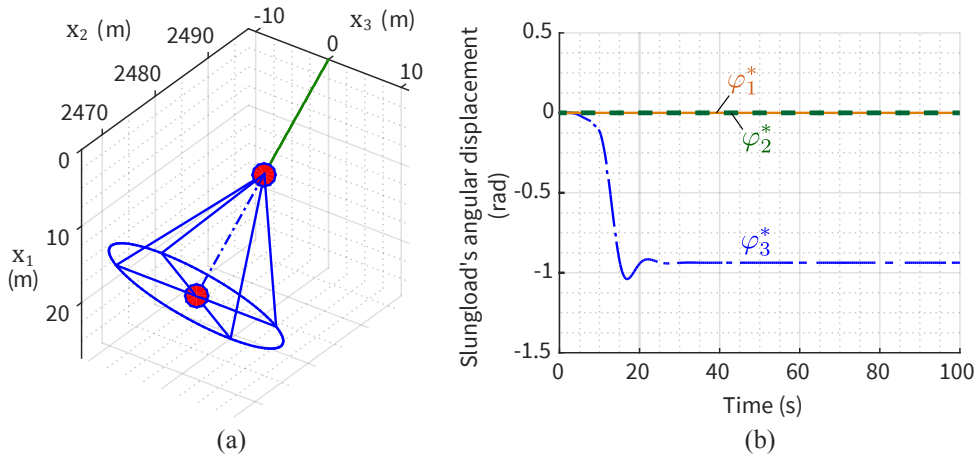

Figure 5.35: (**a**) *Steady state at the end of* 100 *s and* (**b**) *evolution of angular displacement of the underslung load for* 27.8 *m/s forward flight under* 5 *m/s wind.*

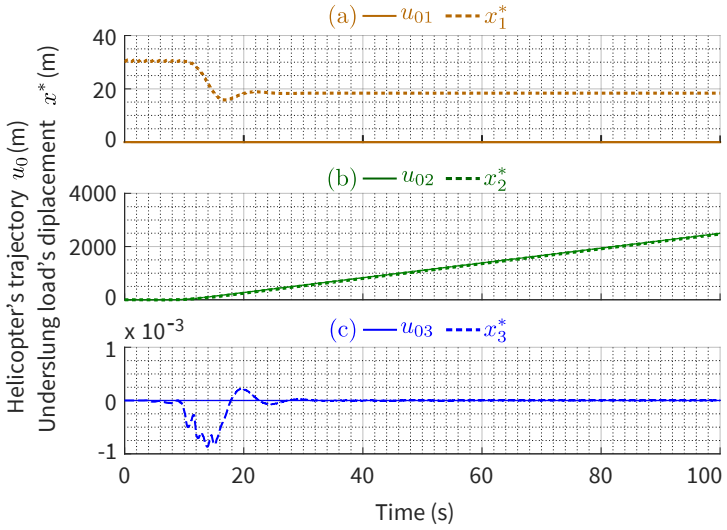

Figure 5.36: *Displacement of the underslung load contrasted with the helicopter's trajectory during* 27.8 *m/s forward flight and under* 5 *m/s wind.*

Note that the small initial oscillations of x_3^* – in the direction normal to wind – are due to the von Karman effect, which was absent in case (1). These oscillations damp out with increase in the forward velocity.

Finally, we simulate the above cable-underslung load system for the minimum snap U-turn (5.2.5) and round (5.2.6) maneuvers. The configurations of cable-underslung load system at the end of the U-turn and round maneuvers are shown in Fig. 5.37. The cables in both these cases is straight while the ring in parallel to the ground when the helicopter stops.

The evolution of underslung load's displacement contrasted with the helicopter's trajectory in the case of U-turn and round maneuvers are, respectively, shown in Figs. 5.38(a) and 5.39(a). We

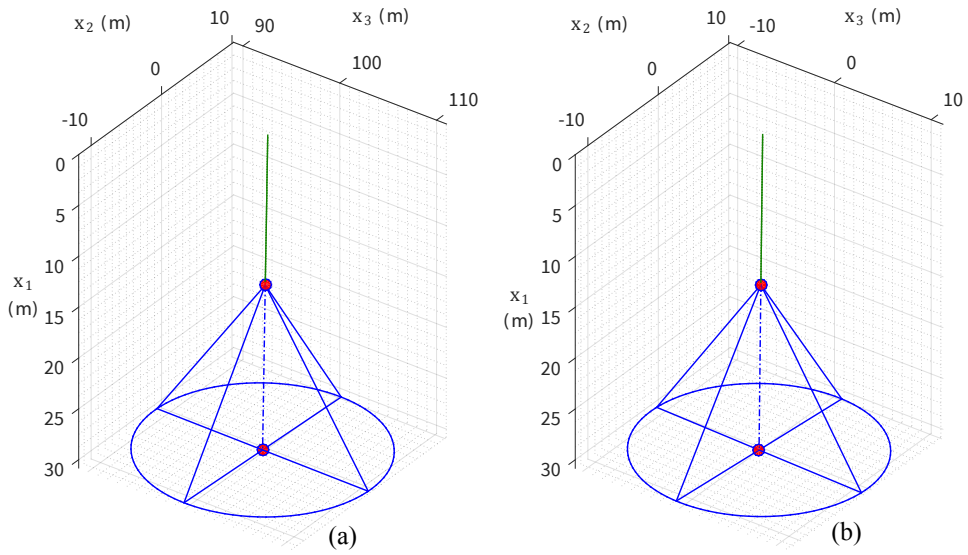

Figure 5.37: *FE solutions are identical when the helicopter finishes, respectively, the minimum snap* $(\mathbf{a})$ *U-turn and* $(\mathbf{b})$ *round maneuvers.*

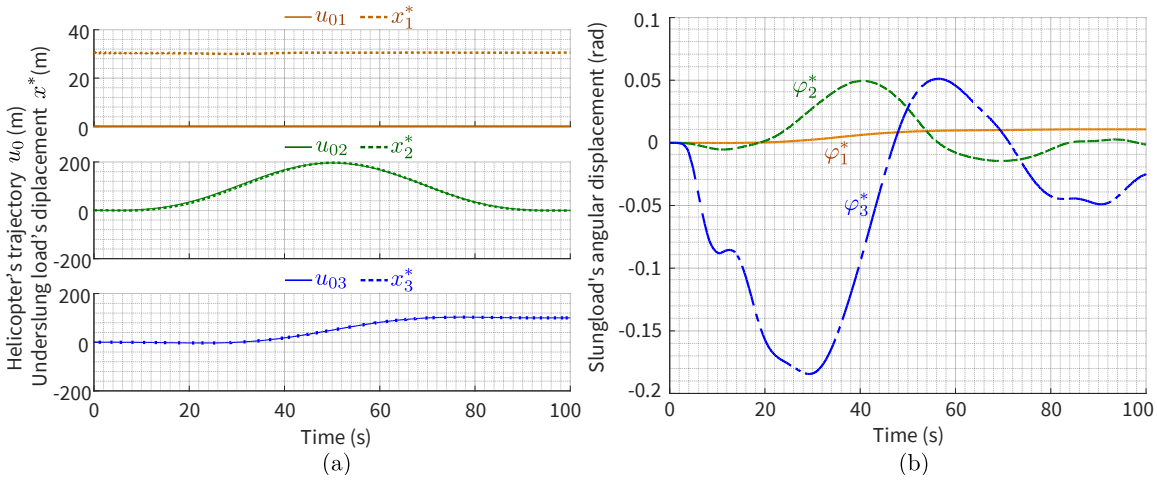

Figure 5.38: *Evolution of* $(\mathbf{a})$ *underslung load's displacements contrasted with helicopter's trajectory and* $(\mathbf{b})$ *evolution of angular displacement of the underslung load, during minimum snap U-turn maneuver under* 5 *m/s wind.*

note that in both these cases the underslung load closely follows the helicopter with negligible deviation. Similarly, the evolution of underslung load's angular displacements are shown in Figs. 5.38(b) and 5.39(b). We observe that these are far less ($< \pm 0.05$ rad) than previous examples for $t > 50$ s. The reason for this is that the heavy weight of the ring brings in a stabilizing effect in this example.

Other than that, the above observations are similar to those in Secs. 5.2.5 and 5.2.6, where comparatively much smaller and lighter underslung load was employed. This tells us that with optimum trajectory design (passive control), we can keep the ring detector at the ideal inclination

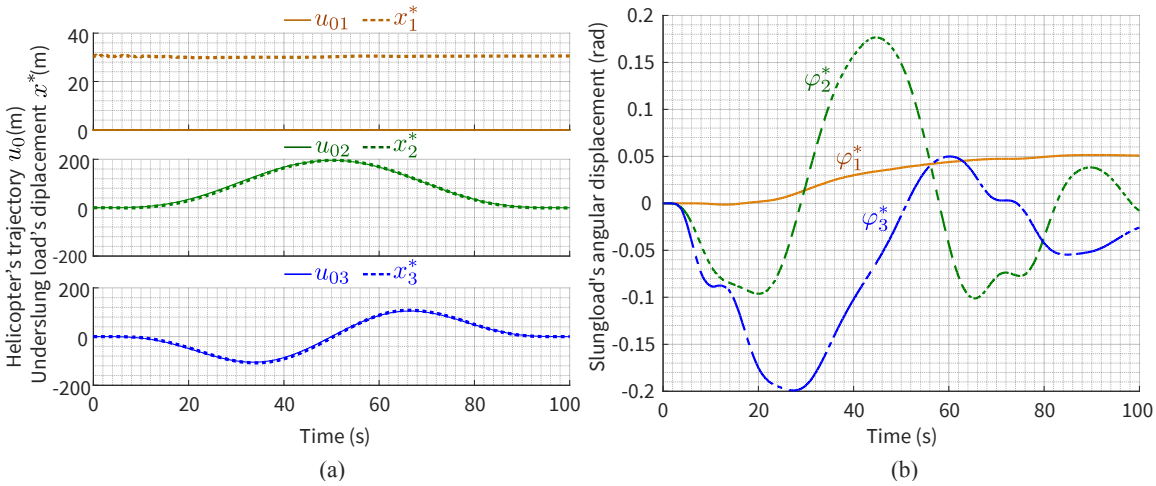

Figure 5.39: *Evolution of* (**a**) *underslung load's displacements contrasted with helicopter's trajectory and* (**b**) *evolution of angular displacement of the underslung load, during minimum snap round maneuver under* 5 *m/s wind.*

to the ground. The speed and time of cruising, as shown in Secs. 5.2.5 and 5.2.6, were determined by the trajectory.

Chapter 6

Conclusions and future work

In this chapter, we summarize some significant outcomes of the present work and then discuss the scope of further research.

We studied the dynamics of a ring-shaped underslung load towed from a helicopter via heavy cable. The cable was modeled as a three-dimensional geometrically exact (GE) beam, in which the effects of large rotation and large displacement are incorporated. It is a considerable improvement over the existing string models for towing cables, especially when the underslung load is large and may undergo complex 3D motion due to aerodynamic drag and helicopter's trajectory. The cable elements were modeled as cylinders inclined in 3D cross-flow when computing the aerodynamic loads. The underslung load was modeled as a rigid body, where the links connecting the large ring-shaped detector to the cable's end were assumed massless and bore negligible aerodynamic drag in contrast to the ring. The drag on the ring was calculated by assuming the ring is made of several rigidly connected cylinders which are inclined in 3D cross-flow. Effects of von Karman vortex shedding were incorporated in the drag model of the cable, while they were neglected in the case of the ring. The equations of motion of the underslung load entered as a boundary condition to that of the cable. The helicopter (top) end of the cable was prescribed to move on given trajectories. In the translating frame of reference, the top end – similar to a hinge – only allowed the cable to rotate about it. The weak form of the cable's equations is nonlinear in displacements and angular displacements of the cable's material points. To set these in the finite element (FE) frameworks required linearization about a base configuration. The linearized weak form was then discretized/meshed into several two-noded elements, and the FE model of the system was obtained. Finally, we simulated various practical conditions of hover, forward flight, U-turn maneuver and round/circular maneuver using this FE model. The response of the system in terms of displacements and angular displacements was studied. We identified

the conditions when the ring detector remained nearly parallel to the ground. During forward flights, we noticed small initial von Karman vibrations in the direction normal to the flow. These eventually damp out when max cruising speed is achieved. We also observed that for flight trajectories which are designed by minimizing higher derivatives of acceleration, such as the snap, the actual path cruised by underslung load had negligible deviations from the desired path. Also, the ring detector in these cases remained parallel to the ground for maximum duration.

Future research

The following avenues offer scope for immediately extending the present research.

1. Detailed modeling of more realistic shapes of the mineral detector, e.g., including the several concentric rings, as shown by Lahiri et al. [2012]'s underslung load can be done to upgrade the present simple ring model. By analyzing the forces in each member, we may be in a better position to investigate the dynamics of the detector.

2. Designing a variety of maneuvers and actively controlling the helicopter's motion for keeping the ring detector parallel to the ground.

3. Setting up and implementing a coupled fluid-structure interaction problem, where the challenge is to compute the fluid forces by solving the Navier-Stokes equations of fluid (wind) in tandem with the nonlinear elastodynamic equations of the cable-underslung load system. This setup can then be used to understand the effect of the air flow close to the helicopter's body, and its effects on the cable.

Apart from the above cases, there are a variety of other challenging engineering applications in which a cable-connected multibody system undergoes complex 3D motion when subjected to aero/hydrodynamic forces. The broader framework presented in this thesis allows us to build similar computational models for enhancing the existing research on the following problems. For example:

1. Aerial refueling of an aircraft requires it to be connected to a source aircraft as shown in Fig. 6.1(a). Both the aircraft are required to maintain certain velocity during this process while flying in different lanes. The fuel hose connected between their respective fuel-tanks undergoes complex 3D motion due to heavy wind loading.

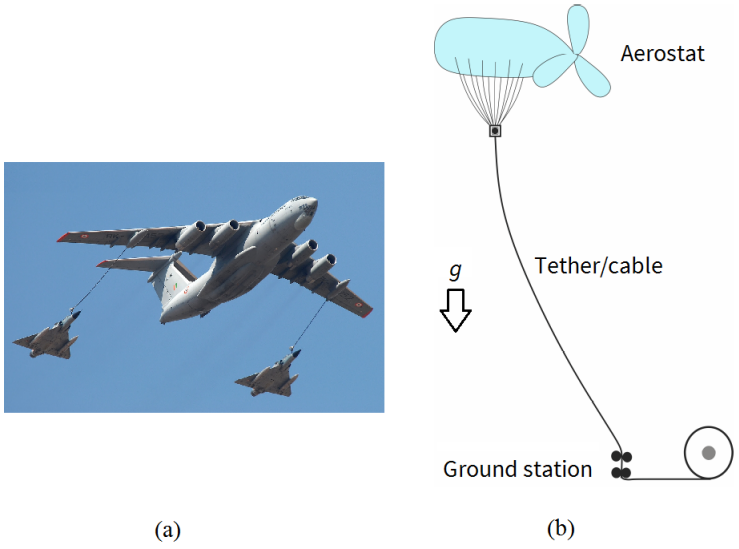

Figure 6.1: (**a**) *A source aircraft is shown refueling two smaller planes via hoses connected between them. Photograph courtesy: The Tribune News Service (dt. 7 Feb 2018), India.* (**b**) *A schematic of an aerostat tethered to the ground station via cable. The figure is taken from Mukherjee [2016].*

2. Aerostat system comprising of a huge balloon that floats at higher altitudes while being tethered to the ground station by a heavy cable is shown in Fig. 6.1(b). They carry instruments for carrying out static aerial surveillance and atmospheric studies. The entire system experiences aerodynamic forces that vary with the altitude, while the balloon is additionally subjected to buoyancy. This system is an inverted case of a hovering cable-underslung load system, where instead of a downward hanging slung load there is a balloon floating vertically upwards.

3. Space tethered systems are instruments, such as telescopes, attached to a satellite via tethers. They undergo complex 3D motions in the space while orbiting around the planet at high velocities. Therefore, modeling the dynamics of such systems is important to avoid entanglement and other issues while controlling the attitude of the instrument.

Finally, problems related to lengthening cables in above applications is another exciting avenue where the research presented in this (Problem A) and the next part (Problem B) have a common scope for future research. In the three applications above, the cable lengthens/extends longitudinally for (1) deploying the fuel hose from source to the receiver aircraft, (2) launching the aerostat from ground to the desired altitude, or (3) relocating the tethered instrument. In lengthening or traveling cables, gyroscopic forces enter into the cable's equation and play a significant role in governing their dynamics; see Problem B.

Problem B

Cable Traveling Against Gravity

Nomenclature

The following list describes the notations that will be used in this part of the thesis.

1. L Initial cable length or the distance between top and bottom roller supports.
2. $x, \bar{x}$ Dimensional and nondimensional coordinates along L.
3. $t, \bar{t}$ Dimensional and nondimensional time.
4. $y(x,t), \bar{y}(\bar{x},\bar{t})$ Dimensional and nondimensional transverse displacement of cable.
5. g Acceleration due to gravity.
6. ρ_0, ρ, w Cable's mass densities in dimensional and nondimensional form, and weight density
7. A_c, I, E Cable's cross-sectional area, area moment of inertia and Young's modulus.
8. $v, \bar{v}$ Dimensional and nondimensional traveling speed.
9. $\bar{v}_{\text{crit}}, \bar{v}_{\text{sub}}, \bar{v}_{\text{sup}}, \bar{v}_{\text{bif}}$ Nondimensional critical, sub-critical, super-critical and bifurcation speeds of the traveling cable.
10. $F(x,t), V, M$ Transversely distributed load, Shear force and Bending Moment, respectively.
11. ζ, c Dimensional and nondimensional coefficient of viscous damping.
12. $T(x,t), \bar{T}(\bar{x},\bar{t})$ Dimensional and nondimensional tension in the cable.
13. μ, μ_s Nondimensional end tension, i.e. at $x = L$, in beam and string, respectively.
14. $\theta = \mu^{-2}$ Nondimensional bending rigidity.
15. $\partial_x^n = \partial^n/\partial x^n, \bar{\partial}_x^n = \partial^n/\partial \bar{x}^n$ The n^{th} order partial derivatives w.r.t. x and $\bar{x}$.
16. $\partial_t^n = \partial^n/\partial t^n, \bar{\partial}_t^n = \partial^n/\partial \bar{t}^n$ The n^{th} order partial derivatives w.r.t. t and $\bar{t}$.
17. $\dot{\square} = d\square/dt = \partial\square/\partial t + v\partial\square/\partial x, \dot{\bar{\square}} = d\square/d\bar{t}$ Total time derivatives in dimensional and nondimensional forms. The respective second derivatives are $\ddot{\square}$ and $\ddot{\bar{\square}}$.
18. S_R Slenderness ratio (nondimensional).
19. $\omega, \text{Re}(\omega), \text{Im}(\omega)$ First mode's nondimensional eigenvalue, with its real and imaginary parts.
20. N Number of sinusoidal shape functions or finite elements.
21. $\bar{E}, \bar{E}_K, \bar{E}_P$ Nondimensional total mechanical, kinetic and potential energy densities.
22. $\dot{\bar{E}}$ Rate of change of the nondimensional total mechanical energy.
23. Matrix notation: all column vectors are in lowercase boldfaced letters: $\mathbf{s}$, $\mathbf{b}$, $\mathbf{q}$, $\mathbf{h}$, $\mathbf{1}$ and $\mathbf{0}$, while all matrices are in uppercase boldfaced letters: $\mathbf{M}$, $\mathbf{A}$, $\mathbf{C}$ and $\mathbf{K}$.

Chapter 7

Introduction

Traveling cables are fundamental driving mechanisms in elevators, conveyor belts, automobile chain-drives, cableways, etc. In these, all or part of the cable is inclined to gravity. During operations the cable tends to oscillate transversely as it travels longitudinally [Barakat, 1968; Miranker, 1960; Mote, 1965, 1966; Rogge, 1972; Sack, 1954; Swope & Ames, 1963; Thurman & Mote, 1969; Wickert, 1992; Wickert & Mote, 1990; Wickert & Mote Jr, 1989]. To prevent breakdown due to fatigue these oscillations need to remain within some design limits. In these studies, cables are modeled either as an elastic beam or as a string.

The dynamics of *horizontally* traveling (traveling direction normal to gravity) beams and strings is well studied [Barakat, 1968; Miranker, 1960; Mote, 1965, 1966; Rogge, 1972; Sack, 1954; Swope & Ames, 1963; Thurman & Mote, 1969; Wickert, 1992; Wickert & Mote, 1990; Wickert & Mote Jr, 1989]. Most work has focused on modal analysis to obtain natural frequencies (eigenvalues) at different operating speeds. Eigenvalues appear as complex conjugates, in which the imaginary part contributes to oscillations while the real part controls the amplitude. During stable operations the real part is absent. Therefore, the *critical speed* at which the eigenvalue first appears as a conjugate pair is of special interest. At this speed the amplitude may grow with time by virtue of the positive real part, leading to instability. For a pre-tensioned strings traveling horizontally in between simple roller supports, Miranker [1960] found that the rate of change of energy of the material between the supports is generally nonzero due to a continuous energy influx from the material outside the supports (boundary), which makes it a nonconservative system. Response to harmonic support excitation was also studied by Miranker [1960], and the instability was identified with the resonance frequency, as the amplitude of the vibration grew with time. Discussions on dissipation and stability of general dynamical systems are found in [Ziegler, 2013].

The critical speed of a traveling cable varies with the type of supports and the distance between them. The arc-length based model of a spatially traveling string proposed by Rogge [1972] generalized all its preceding models. The calculations in [Barakat, 1968; Miranker, 1960] of the energy flow in a dissipation-free model were later improved when an additional energy influx from the supports was identified by Wickert & Mote Jr [1989]. However, it was noted that the total energy during steady horizontal travel was not constant in spite of zero damping. Thus, the system was nonconservative whether or not the modal analysis predicted instability.

Apart from the above studies which focus on linear beam/string models, several others [Farokhi et al., 2013a,b, 2016; Ghayesh et al., 2013a,b; Ghayesh & Farokhi, 2015; Ghayesh et al., 2013; Mockensturm & Guo, 2005; Öz et al., 2001; Pakdemirli & Ulsoy, 1997] have studied the effects of geometric and/or material nonlinearities on the stability of the beams which are either accelerating or moving with a constant speed in between *horizontally* aligned supports. Most results on the horizontally traveling beams and strings have been compiled by Hagedorn & DasGupta [2007] and Banichuk et al. [2013]. They include discussions on modal, transient and energy analyses. We restrict ourselves from visiting them individually, due to constraint of space, and focus primarily on linear beam and string models for the cables traveling vertically, against gravity.

For a vertically traveling heavy cable the tension varies along its length. This leads to the governing equation of motion with a spatially varying coefficient, which makes the equation *non* self-adjoint which cannot be solved exactly. Traveling against gravity, in turn, affects the critical speed at which instability sets in. To the best of our knowledge this case, which has practical importance, has not yet been investigated. The work presented in this part of the thesis has now been published [Dehadrai et al., 2018] in the Journal of Computational & Nonlinear Dynamics.

This part is organized as follows. We begin from Chapter 8 by modeling the cable as a beam traveling vertically (against gravity) with constant speed, while resting upon small and smooth rollers; see Fig. 8.1. A string model, useful for very flexible cables, is obtained as a special case in Sec. 8.2. Then a modal analysis is done in Sec. 9.1 of Chapter 9 to identify the relation between speed, inclination (horizontal and vertical), tension, bending rigidity, slenderness ratio and the conditions of instability. In Sec. 9.5 of Chapter 9, we verify the instability from evolution of both the energy and the amplitude of oscillations obtained after direct time-integration of the model. The concluding Chapter 10 summarizes the implications on cable design of our analyses, and discusses future scope of research.

Chapter 8

Governing Equations

A heavy cable traveling vertically, against gravity, between two pairs of small rollers is shown in Fig. 8.1. The $x-$ axis is aligned with the cable, and has its origin in between the bottom rollers. The distance between the top and bottom rollers is L and the acceleration due to gravity g acts vertically downwards. The cable has uniform mass density ρ_0, cross-section A_c, Young's modulus E, and cross-sectional area moment of inertia I. The speed v of each material particle along the length of the cable is constant. The transverse displacement $y = y(x,t)$ of a material point located at x is measured from the vertical axis (broken line), and it is assumed to be small. To account for presence of fluid drag, a transversely distributed loading $F(x,t) = \zeta\,\dot{y}$, with damping coefficient ζ, is applied. For small transverse deflection, the weight $w = \rho_0 A_c g$ per unit length

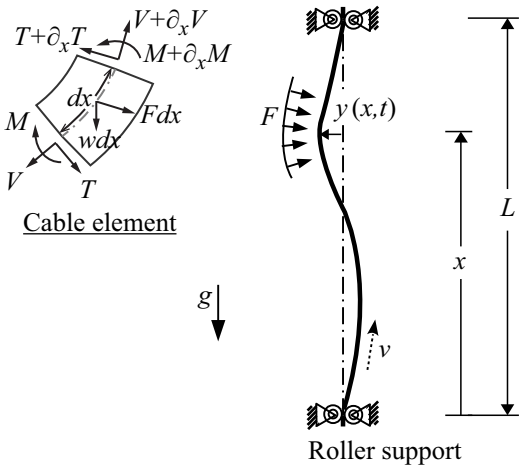

Figure 8.1: *Schematic of a traveling cable at time t and a free body diagram (top-left) of the cable element of length $ds \approx dx$ is shown. The deflections of the cable are exaggerated for clarity.*

of the cable causes its tension to vary along the cable's length:

$$T(x) = T(L) - w\,(L - x)\,, \tag{8.0.1}$$

where we assume that the tension $T(L)$ at $x = L$ is known.

A free body diagram of small cable-element is also shown in the Fig. 8.1. The tension T, shear force V and bending moment M on the element evolve over the element's length ds $(\approx dx)$ to $T + \partial_x T\mathrm{dx}$, $V + \partial_x V\mathrm{dx}$ and $M + \partial_x M\mathrm{dx}$, respectively. Here, we have employed the notation $\partial_x^n = (\partial^n/\partial x^n)$ and $\partial_t^n = (\partial^n/\partial t^n)$ for the n^{th} order partial derivatives with respect to x and t, respectively. The external forces $Fds \approx Fdx$ due to damping and $wds \approx wdx$ due to weight are also shown on the element.

8.1 Beam model

The bending moment M and the shear force V in the cable are related by, respectively, the bending-curvature equation [Timoshenko & Gere, 2009]

$$M = EI\ \partial_x^2 y,$$

and the angular momentum equation,

$$V = \partial_x(\rho I\ddot{y} - M).$$

Now, we balance the linear momenta and obtain the equations governing the transverse vibrations of the beam:

$$[EI\partial_x^4 - \partial_x\{T(x)\ \partial_x\}]y + \zeta\dot{y} + (\rho_0 A_c - \rho_0 I\partial_x^2)\ddot{y} = 0 \tag{8.1.1a}$$

where

$$\dot{y}(x,t) = \partial_t y + v\,\partial_x y$$

and

$$\ddot{y}(x,t) = \partial_t^2 y + 2v\,\partial_x\partial_t y + v^2\ \partial_x^2 y.$$

The small and well lubricated (smooth) roller supports offer a displacement-free and moment-free boundary conditions on the beam,

$$y(0,t) = y(L,t) = \partial_x^2 y(0,t) = \partial_x^2 y(L,t) = 0. \tag{8.1.1b}$$

In (8.1.1) the term $\partial_t y$ is called the *local* velocity, $v\,\partial_x y$ is the *convective* velocity of a material point, $\partial_t^2 y$ is the *local* acceleration, $2v\,\partial_x\partial_t y$ is a gyroscopic term and $v^2\ \partial_x^2 y$ is the convective acceleration. Furthermore, the term $EI\partial_x^4 y$ accounts for bending rigidity, while $\rho_0 I\partial_x^2\ddot{y}$ is the rotary inertia. When $T(x) = T(L)$, we recover transverse vibrations of a horizontally traveling Rayleigh beam, while the Euler-Bernoulli beam of Hagedorn & DasGupta [2007] is recovered when rotary inertia is also ignored.

8.2 Special case: string model

For a heavy cable which is highly flexible and has negligible shear and bending rigidity, a string model is arrived at by ignoring EI in (8.1.1):

$$[-\partial_x\{T(x)\,\partial_x\}]y + \zeta\dot{y} + \rho_0 A_c\ddot{y} = 0 \tag{8.2.1a}$$

with

$$y(0,t) = y(L,t) = 0. \tag{8.2.1b}$$

The equation for a horizontally traveling string considered in [Hagedorn & DasGupta, 2007] is retrieved from (8.2.1) by setting $T(x) = T(L)$.

8.3 Nondimensionalization

For further analysis, the dimensionless forms of the governing equation (8.1.1) are derived here. To this end, we introduce nondimensional quantities

$$\begin{gathered}\bar{x} = \frac{x}{L},\ \bar{y} = \frac{y}{L},\ \bar{t} = t\sqrt{\frac{EI}{\rho_0 A_c L^4}},\\ \bar{v} = v\sqrt{\frac{\rho_0 A_c L^2}{EI}},\ \mu = \sqrt{\frac{T(L)L^2}{EI}},\\ \rho = \frac{wL^3}{EI},\ \mathrm{S_R} = \sqrt{\frac{L^2 A_c}{I}} \text{ and } c = \frac{\zeta L^2}{\sqrt{EI\rho_0 A_c}}.\end{gathered} \tag{8.3.1}$$

Our definition of slenderness ratio $\mathrm{S_R}$ follows [Timoshenko & Gere, 2009, pg. 50] and should be contrasted with that of [Hagedorn & DasGupta, 2007, pg. 125], which is same as our $\mathrm{S_R^2}$. The dimensionless end tension μ will be employed as a control parameter to vary tension in the cable. With these (8.1.1) transforms to

$$\left[\bar{\partial}_x^4 - \bar{\partial}_x\left\{\bar{T}(\bar{x})\,\bar{\partial}_x\right\}\right]\bar{y} + c\dot{\bar{y}} + \left(1 - \mathrm{S_R}^{-2}\bar{\partial}_x^2\right)\ddot{\bar{y}} = 0 \tag{8.3.2a}$$

and

$$\bar{y}(0,\bar{t}) = \bar{y}(1,\bar{t}) = \bar{\partial}_x^2\bar{y}\,(0,\bar{t}) = \bar{\partial}_x^2\bar{y}\,(1,\bar{t}) = 0, \tag{8.3.2b}$$

where $\bar{\partial}_x = \partial/\partial\bar{x}$ and $\bar{\partial}_t = \partial/\partial\bar{t}$, and the nondimensional tension

$$\bar{T}(\bar{x}) = \mu^2 - \rho\,(1-\bar{x})\,. \tag{8.3.3}$$

For the string of Sec. 8.2 we employ the following nondimensionalization:

$$\bar{x} = \frac{x}{L},\ \bar{y} = \frac{y}{L},\ \bar{t} = t\sqrt{\frac{T(L)}{\rho_0 A_c L^2}},$$

$$\bar{v} = v\sqrt{\frac{\rho_0 A_c}{T(L)}},\ \bar{T}(\bar{x}) = \frac{T(x)}{T(L)},\ \mu = 1, \tag{8.3.4}$$
$$\rho = \frac{wL}{T(L)},\ \text{and}\ c = \frac{\zeta L}{\sqrt{T(L)\rho_0 A_c}}.$$

With these (8.2.1) becomes

$$\left[-\bar{\partial}_x \left\{\bar{T}(\bar{x})\ \bar{\partial}_x\right\}\right] \bar{y} + c\dot{\bar{y}} + \ddot{\bar{y}} = 0, \tag{8.3.5a}$$

and

$$\bar{y}(0,\bar{t}) = \bar{y}(1,\bar{t}) = 0. \tag{8.3.5b}$$

With an alternative nondimensionalization scheme we can avoid separate dimensionless parameters for the beam and the string equations, as in (8.3.1) *and* (8.3.4)*, and employ the bending rigidity as the control parameter instead of the end tension. This is discussed in the* Sec. 9.3.

Chapter 9

Numerical Solution

The governing equations, (8.1.1) and (8.2.1), or their dimensionless forms, (8.3.2) and (8.3.5), are not self-adjoint and cannot be solved exactly. Hence, we use the Galerkin method [Meirovitch & Hagedorn, 1994] for computing the eigenvalues and time response for the beam and string models. Towards this, we assume the expansion

$$\bar{y}_N(\bar{x},t) = \mathbf{s}^{\mathsf{T}}\mathbf{b}, \tag{9.0.1}$$

where $\mathbf{s}(\bar{x}) = [\sin(n\pi\bar{x})]^{\mathsf{T}}$, for $n = 1 \ldots N$, is an N-dimensional column vector of sine modes, and $\mathbf{b}(\bar{t}) = [b_1(\bar{t}), b_2(\bar{t}), \cdots b_N(\bar{t})]^{\mathsf{T}}$ is a column vector of time-varying unknown coefficients. The modes individually vanish at the boundaries, thereby satisfying the geometric boundary conditions. Then (8.3.2) evaluated at $\bar{y} = \bar{y}_N$ results in an error, called the *residue*. By setting the projections of the residue onto the N sine modes to zero yields a set of N differential algebraic equation, which may be cast in the following state-space form:

$$\frac{d\mathbf{q}}{d\bar{t}} = \mathbf{A}\mathbf{q}, \tag{9.0.2a}$$

where the state vector and the state matrix are, respectively,

$$\mathbf{q} = \begin{bmatrix} \dot{\mathbf{b}} \\ \mathbf{b} \end{bmatrix} \quad \text{and} \quad \mathbf{A} = \int_0^1 \begin{bmatrix} -\mathbf{M}^{-1}\mathbf{C} & \mathbf{1} \\ -\mathbf{M}^{-1}\mathbf{K} & \mathbf{0} \end{bmatrix} d\bar{x}, \tag{9.0.2b}$$

with $\mathbf{1}$ representing an $N\times N$ identity matrix and $\mathbf{0}$ being the $N\times N$ zero matrix, while

$$\begin{aligned} \mathbf{M} &= \left(\mathbf{s}\mathbf{s}^{\mathsf{T}}\right) + \mathsf{S}_{\mathsf{R}}^{-2}\left(\mathbf{s}'\mathbf{s}'^{\mathsf{T}}\right), \\ \mathbf{C} &= c\left(\mathbf{s}\mathbf{s}^{\mathsf{T}}\right) + 2\bar{v}\left(\mathbf{s}\mathbf{s}'^{\mathsf{T}} + \mathsf{S}_{\mathsf{R}}^{-2}\mathbf{s}'\mathbf{s}''^{\mathsf{T}}\right) \end{aligned} \tag{9.0.2c}$$

and

$$\begin{aligned} \mathbf{K} = \left(1 - \mathsf{S}_{\mathsf{R}}^{-2}\bar{v}^2\right)\left(\mathbf{s}''\mathbf{s}''^{\mathsf{T}}\right) - \left\{\bar{v}^2 - \bar{T}(\bar{x})\right\}\left(\mathbf{s}'\mathbf{s}'^{\mathsf{T}}\right) \\ + \frac{c\bar{v}}{2}\left(\mathbf{s}\mathbf{s}'^{\mathsf{T}} - \mathbf{s}'\mathbf{s}^{\mathsf{T}}\right) \end{aligned}$$

are the mass, damping and stiffness matrices, respectively, with $(\,)'$ denoting $d/d\bar{x}$. Note that the mass matrix $\mathbf{M}$ is symmetric, while the damping matrix $\mathbf{C}$ has a symmetric part $c(\mathbf{s}\mathbf{s}^{\mathsf{T}})$ and a skew-symmetric part $2\bar{v}(\mathbf{s}\mathbf{s}'^{\mathsf{T}} + \mathsf{S}_{\mathsf{R}}^{-2}\mathbf{s}'\mathbf{s}''^{\mathsf{T}})$ called the gyroscopic damping. From the stiffness matrix $\mathbf{K}$, after replacing for $\bar{T}$ from (8.3.3), we obtain four terms: the material stiffness $(1 - \mathsf{S}_{\mathsf{R}}^{-2}\bar{v}^2)\,(\mathbf{s}''\mathbf{s}''^{\mathsf{T}})$, the geometric stiffness $(\bar{v}^2 - \mu^2)\,(\mathbf{s}'\mathbf{s}'^{\mathsf{T}})$, the stiffness $\rho\,(1 - \bar{x})\,(\mathbf{s}'\mathbf{s}'^{\mathsf{T}})$ due to the cable's weight, and the stiffness $c\bar{v}\,(\mathbf{s}\mathbf{s}'^{\mathsf{T}} - \mathbf{s}'\mathbf{s}^{\mathsf{T}})/2$ due to damping. While the first three stiffness terms are symmetric, the last one is skew-symmetric. The state-space form for the string model (8.3.5) is obtained by setting $\mathsf{S}_{\mathsf{R}}^{-2} = 0$ and $\mu = 1$ in $\mathbf{M}$ and $\mathbf{K}$.

Equation (9.0.2) may be treated as an *eigenvalue* problem for *modal analysis*, or an initial value problem for *transient analysis*. In modal analysis, the cable's natural frequencies corresponding to the specified modes are extracted directly from (9.0.2). In a transient analysis, $\mathbf{b}(\bar{t})$ is calculated through direct time-integration of the state-space equation (9.0.2a) with given initial conditions $\mathbf{b}(0)$ and $\dot{\mathbf{b}}(0)$. The material displacements are then obtained from (9.0.1).

Finite element (FE) formulation: An alternate way to obtain the state-space form is through the *finite-element* (FE) method. Instead of assuming *global* sinusoidal shape functions of (9.0.1), the domain $\bar{x} = [0, 1]$ is discretized into N elements, following which the displacement $\bar{y}$ and the slope $\bar{y}'$ at each $N + 1$ nodes (locations) are approximated by a complete cubic (Hermite) polynomial and its derivative.

For a two-node element e with the first node at $\bar{x}_e$ and second node at $\bar{x}_e + h$, where h is the element's length, the Hermite polynomials [Bathe, 2006] for the first node are

$$p_e^{(1)}(\bar{x}) = 1 - 3\left(\frac{\bar{x} - \bar{x}_e}{h}\right)^2 + 2\left(\frac{\bar{x} - \bar{x}_e}{h}\right)^3$$

and

$$\varphi_e^{(1)}(\bar{x}) = -\,(\bar{x} - \bar{x}_e)\left(1 - \frac{\bar{x} - \bar{x}_e}{h}\right)^2,$$

and those at the second node are

$$p_e^{(2)}(\bar{x}) = 3\left(\frac{\bar{x} - \bar{x}_e}{h}\right)^2 - 2\left(\frac{\bar{x} - \bar{x}_e}{h}\right)^3$$

and

$$\varphi_e^{(2)}(\bar{x}) = -\,(\bar{x} - \bar{x}_e)\left\{\left(\frac{\bar{x} - \bar{x}_e}{h}\right)^2 - \frac{\bar{x} - \bar{x}_e}{h}\right\},$$

where $p_e(\bar{x})$ and $\varphi_e(\bar{x})$ are the interpolating functions for the displacement $\bar{y}(\bar{x})$ and slope $\bar{y}'(\bar{x})$, respectively. Further, for each element

$$\bar{y}_e = \mathbf{h}_e^{\mathsf{T}}\mathbf{b}_e,$$

where $\mathbf{b}_e$ is the nodal degree of freedom and

$$\mathbf{h}_e = \left[p_e^{(1)}, \varphi_e^{(1)}, p_e^{(2)}, \varphi_e^{(2)}\right]^{\mathsf{T}}.$$

Thus, the elemental state equation is $\dfrac{d\mathbf{q}_e}{d\bar{t}} = \mathbf{A}_e\mathbf{q}_e$, where the elemental state vector and the elemental state matrix are

$$\mathbf{q}_e = \begin{bmatrix} \dot{\mathbf{b}}_e \\ \mathbf{b}_e \end{bmatrix} \quad \text{and} \quad \mathbf{A}_e = \int_0^h \begin{bmatrix} -\mathbf{M}_e^{-1}\mathbf{C}_e & \mathbf{1}_e \\ -\mathbf{M}_e^{-1}\mathbf{K}_e & \mathbf{0}_e \end{bmatrix} d\bar{x},$$

while the definitions of $\mathbf{M}_e$, $\mathbf{C}_e$ and $\mathbf{K}_e$ are analog to those in (9.0.2c),

$$\mathbf{M}_e = \left(\mathbf{h}_e\mathbf{h}_e^{\mathsf{T}}\right) + \mathsf{S}_{\mathsf{R}}^{-2}\left(\mathbf{h}_e'\,\mathbf{h}_e'^{\mathsf{T}}\right),$$

$$\mathbf{C}_e = c\left(\mathbf{h}_e\mathbf{h}_e^{\mathsf{T}}\right) + 2\bar{v}\left(\mathbf{h}_e\mathbf{h}_e'^{\mathsf{T}} + \mathsf{S}_{\mathsf{R}}^{-2}\mathbf{h}_e'\,\mathbf{h}_e''^{\mathsf{T}}\right)$$

and

$$\mathbf{K}_e = \left(1 - \mathsf{S}_{\mathsf{R}}^{-2}\bar{v}^2\right)\left(\mathbf{h}_e''\,\mathbf{h}_e''^{\mathsf{T}}\right) - \left\{\bar{v}^2 - \bar{T}(\bar{x})\right\}\left(\mathbf{h}_e'\mathbf{h}_e'^{\mathsf{T}}\right) + \frac{c\bar{v}}{2}\left(\mathbf{h}_e\mathbf{h}_e'^{\mathsf{T}} - \mathbf{h}_e'\mathbf{h}_e^{\mathsf{T}}\right)$$

Finally, carrying out standard FE procedures [Bathe, 2006], the global state equation (9.0.2) is obtained by assembling all the elemental state equations, so that the global state matrix $\mathbf{A}$ is $2N \times 2N$ block diagonal matrix, where each block is the elemental state matrix $\mathbf{A}_e$, for $e = 1$ to N, and $\mathbf{q}$ is $2N \times 1$ global state vector.

We now discuss modal analysis in detail, followed by a brief discussion of energetics and transient analysis.

9.1 Modal Analysis

The state matrix $\mathbf{A}$ in (9.0.2b) is *not* symmetric in general, but it has N complex conjugate eigenvalues ω_n, for $n = 1$ to N. The eigenvalues depend upon the geometric and material parameters of the cable, *viz.* travel speed, prevailing tension, bending rigidity and the slenderness ratio of the cable.

The accuracy of modal analysis depends on the number of sine modes (Galerkin) or elements (FE) employed, and we discuss this in Sec. 9.4. With sufficient number of modes and elements both Galerkin with sine modes and FE give the same results. Thus, henceforth, we will report results utilizing the Galerkin method only.

Accordingly, the transverse displacement is

$$\bar{y}_N(\bar{x}, \bar{t}) = \mathsf{Re}\sum_{n=1}^{N} a_n \exp[\{\mathsf{Re}(\omega_n) \pm i\,\mathsf{Im}(\omega_n)\}\bar{t}]\sin(n\pi\bar{x}),$$

where a_n are the unknown amplitudes which are found from initial conditions, and the N sinusoidal modes collectively define the instantaneous shape of the cable, while the oscillatory part $\exp\{\pm i\ \mathrm{Im}(\omega_n)\bar{t}\}$ modulates the material point's vibration about its equilibrium state. The growth or decay of the amplitude of these vibrations is governed by $\exp\{\mathrm{Re}(\omega_n)\bar{t}\}$. The real part of the eigenvalue, thus, governs the solution's, and hence the cable's instability.

9.2 Stability

Onset of instability in operation corresponds to the emergence of positive real part of the first mode's eigenvalue. When this happens the displacements grow exponentially with time. This

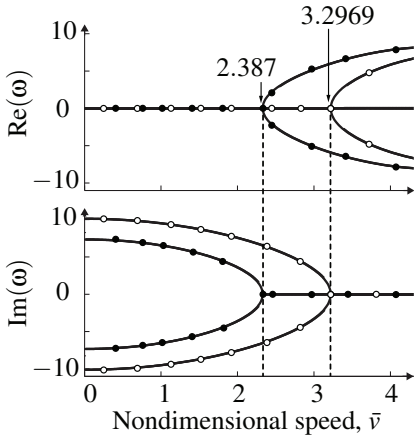

Figure 9.1: *Comparison of the first eigenvalues for cables modeled as Euler-Bernoulli beam: (—•—) represents the vertically traveling cable for which the parameter $\rho = 10$, while (—○—) represents the cable traveling horizontally for which $\rho = 0$. For both the cases, the other parameters $\mu = 1$, $S_R^{-2} = 0$ and $c = 0$.*

may result in failure and/or bring in nonlinear effects, hitherto ignored. The instability criterion identifies the *critical value* of the governing parameter at which the real part of the first mode's eigenvalue first becomes positive. Here, we explicitly define two dimensionless quantities that we will use frequently in this part of the thesis:

Critical speed $\bar{v}_{\mathrm{crit}}$ is defined as the nondimensional speed of the traveling cable at which the $\mathrm{Re}(\omega)$ of the first mode's eigenvalue ω first becomes positive. This point can be easily identified when $\mathrm{Re}(\omega)$ is plotted as a function of $\bar{v}$, such as in Fig. 9.1.

Bifurcation speed $\bar{v}_{\mathrm{bif}}$ is defined as the nondimensional speed of the traveling cable at which the already existing positive and negative parts of the $\mathrm{Im}(\omega)$ vanish, whereas the $\mathrm{Re}(\omega)$ splits or bifurcates into two parts.

For example, in Fig. 9.1, we identify nondimensional speeds $\bar{v} = 2.387$ and 3.2969 as the *critical* speeds for cables traveling vertically and horizontally, respectively. Beyond these speeds

the Re(ω) bifurcates and the Im(ω) vanishes. This implies that for the traveling cables modeled as an Euler-Bernoulli beam, the speeds $\bar{v}_{\text{crit}} = \bar{v}_{\text{bif}}$, i.e., the appearance of positive Re(ω) and the bifurcation of Re(ω) with vanishing of Im(ω) both occur at simultaneously. Moreover, as we will see later in this section, $\bar{v}_{\text{crit}}$ and $\bar{v}_{\text{bif}}$ are also same for the horizontally traveling Rayleigh beam, but different for the vertically traveling Rayleigh beam.

The critical/bifurcation speed shifts to the left when the Euler-Bernoulli beam (Fig. 9.1) travels vertically. This implies a *lowering* of the critical speed of operation due to the influence of gravity g on tension $T(x)$ in the cable leading to an earlier onset of instability compared to the case when the cable was considered traveling horizontally. The critical speed $\bar{v}_{\text{crit}} = 3.2969$ for the horizontally traveling beam agrees well with the value reported by Wickert & Mote [1990].

A higher tension in the cable stabilizes the system. This role of tension in enhancing stability is lowered by the action of gravity in vertically traveling cables as shown in Fig. 9.2. The resulting

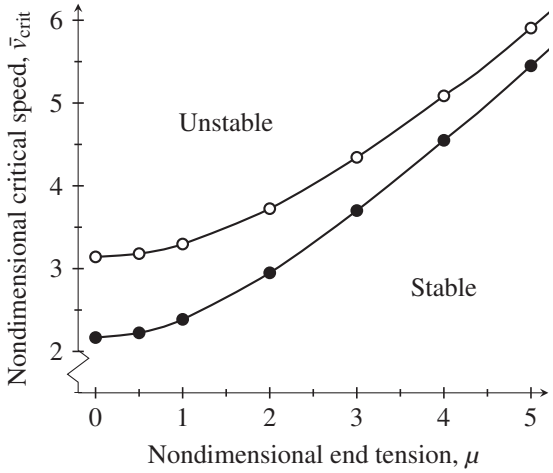

Figure 9.2: *Stability curves for Euler-Bernoulli beams traveling horizontally (–○–) and vertically (–●–) are obtained by plotting the nondimensional critical speed $\bar{v}_{\text{crit}}$ as a function of nondimensional end tension μ. The parameter $\rho = 0$ and 10 for the horizontally and vertically traveling beams, respectively, while the other parameters $c = 0$ and $S_R^{-2} = 0$.*

curve for each is the boundary separating regions of stable and unstable operations, which lie below and above the curve, respectively. Furthermore, we observe that, as expected, increasing the cable tension delays the onset of instability, thereby ensuring stable operation at relatively higher speeds. The critical speeds for both the horizontally and the vertically traveling beams converge as the end tension rises further; see Fig. 9.2. Thus, tension contributes to the stability.

Consider now a cable modeled as a Rayleigh beam wherein rotary inertia is retained. In a horizontally traveling Rayleigh beam the slenderness ratio S_R, defined in (8.3.1), improves the

stability for any nonzero end-tension μ and mass density ρ, as shown by the solid curve in Fig. 9.3. At higher S_R the rotary inertia term in (8.3.2) becomes small compared to the bending rigidity. Therefore, with increasing slenderness ratio, the stability boundary of the Rayleigh beam approaches that of a traveling Euler-Bernoulli beam (dashed line); the latter, of course, remains unaffected by S_R. Interestingly, we find that a vertically traveling Rayleigh beam is inherently

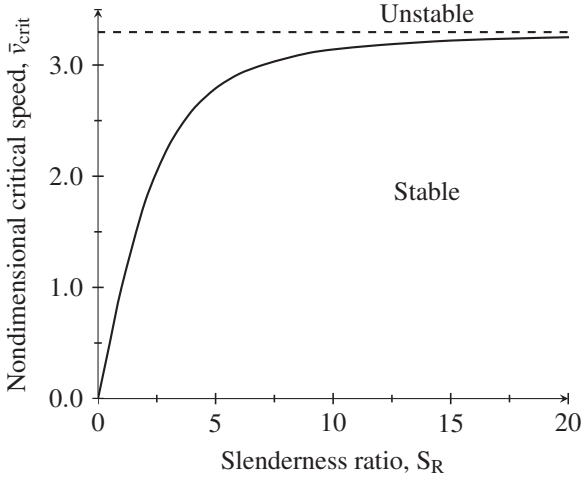

Figure 9.3: *Stability curves obtained by plotting nondimensional critical speed $\bar{v}_{crit}$ as a function of slenderness ratio S_R for horizontally traveling Rayleigh (—) and Euler-Bernoulli (- - -) beams. The other parameters $\rho = 0$, $\mu = 1$ and $c = 0$.*

*un*stable, i.e. at any S_R the real part Re(ω) of the first mode's eigenvalue ω is always positive, as shown in the inset of Fig. 9.4, implying that its critical speed $\bar{v}_{crit} = 0$. Moreover, unlike an Euler-Bernoulli beam (Fig. 9.1) or the horizontally traveling Rayleigh beam, the bifurcation speed $\bar{v}_{bif} = 2.36$ of vertically traveling Rayleigh beam (Fig. 9.4) is different than its $\bar{v}_{crit}$.

However, we observe that the inclusion of damping ($c > 0$) shifts the real part of the first eigenvalue below zero, thereby removing the inherent instability of a vertically traveling Rayleigh beam. The amount that Re(ω) shifts depends upon the amount of damping c introduced, as shown in Fig. 9.5. Also, introducing more damping shifts $\bar{v}_{crit}$ further to the right. This shift in critical speed due to damping maybe employed to provide a suitable range of speeds $\bar{v} < \bar{v}_{crit}$ for stable operation. Figure 9.6 plots $\bar{v}_{crit}$ as a function of c. We observe that the stability curve (solid line) grows steadily with c, after a steep initial rise (inset of Fig. 9.6) due to inclusion of damping, thereby confirming that damping enhances the stability. However, as shown in Fig. 9.5, the speed $\bar{v}_{bif}$ at which the first eigenvalue bifurcates is less than $\bar{v}_{crit}$ for the damped, vertically traveling, Rayleigh beam. This indicates the existence of complex eigenvalues at sub-bifurcation speeds, resulting in underdamped oscillations of the beam in its first mode during stable operation. In

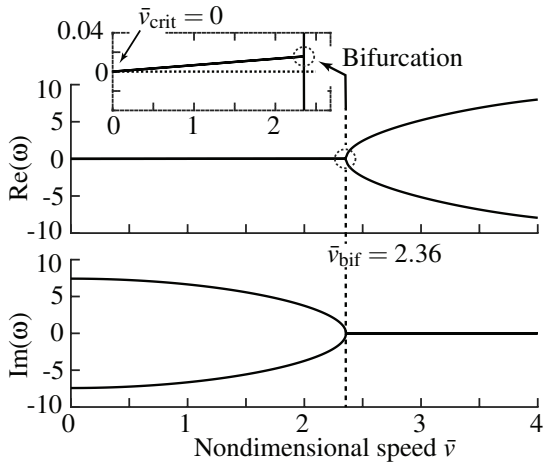

Figure 9.4: *Real and imaginary part of the smallest (first) eigenvalue of an undamped ($c = 0$), vertically traveling Rayleigh beam as functions of speed for $\rho = 10$, $\mu = 1$ and $S_R = 20$. The inset shows the existence of positive real part at all nondimensional speeds $\bar{v} > 0$, while the bifurcation (as in Fig. 9.1) happens much later when $\bar{v} = \bar{v}_{bif} = 2.36$.*

contrast to $\bar{v}_{\text{crit}}$, the bifurcation point in the damped beam shifts left, i.e. $\bar{v}_{\text{bif}}$ decreases with increase in damping. We note from this behaviour of $\bar{v}_{\text{bif}}$, that when c is increased enough, there will be a $\bar{v}$ at which $\text{Im}(\omega)$ of the first mode will cease to appear. When this happens, the higher modes (not shown) become significant and govern the beam's oscillations. Figure 9.6 also plots $\bar{v}_{\text{bif}}$ curve (broken line) which diminishes monotonically with increase in c. This indicates that the vertically traveling cable is stable due to damping and has underdamped oscillations when the speed is beneath the broken line in Fig. 9.6, while it is stable and undergoes *no* oscillations when the speed is between the solid and broken lines.

A damped Euler-Bernoulli beam shows a similar behaviour and is not discussed for brevity.

String model

For highly flexible cables (*negligible bending rigidity*), the end tension $T(L)$ in the cable and the influence of gravity on tension $T(x)$ govern stability. Figure 9.7 plots the dimensionless critical speed $\bar{v}_{\text{crit}}$ as a function of scaled end tension

$$\mu_s = \frac{T(L)|_{\text{vertical}}}{T(L)|_{\text{horizontal}}},$$

which is a ratio of end tension $T(L)$ in a vertically traveling string to the tension in a string that is traveling horizontally. The curves in Fig. 9.7 plot the stability curve for horizontally and vertically traveling strings. We again note that cables traveling vertically, against gravity, are more unstable, and the end tension enhances stability. However, unlike for beams, the tension does *not* affect the critical speed of horizontally traveling strings. In this case the dimensionless

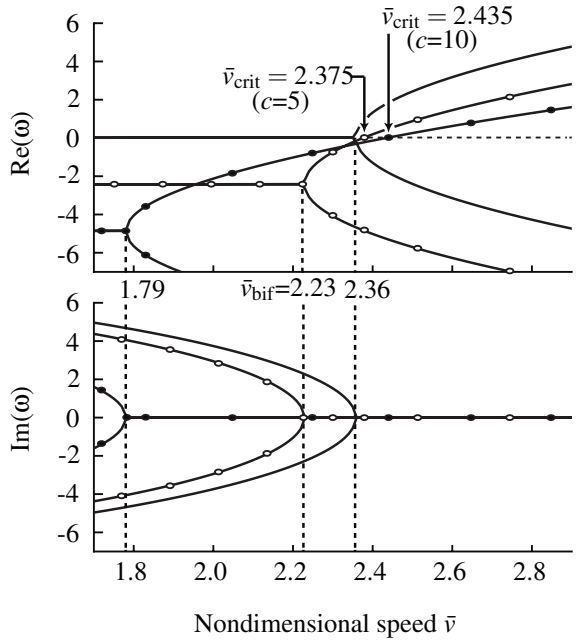

Figure 9.5: *Real and imaginary parts of the first mode's eigenvalue for a damped, vertically traveling, Rayleigh beam as function of nondimensional speed $\bar{v}$ for nondimensional viscosity $c = 0$ (—), 5 (–∘–) and 10 (–•–). The other parameters $\rho = 10$, $S_R = 20$ and $\mu = 1$. We observe that with damping the critical speed $\bar{v}_{crit}$ increases from 0 for $c = 0$ to 2.375 for $c = 5$, and 2.435 for $c = 10$. Also, Re(ω) bifurcates at speeds $\bar{v}_{bif} < \bar{v}_{crit}$ for $c = 5$ and 10, in contrast to when $c = 0$.*

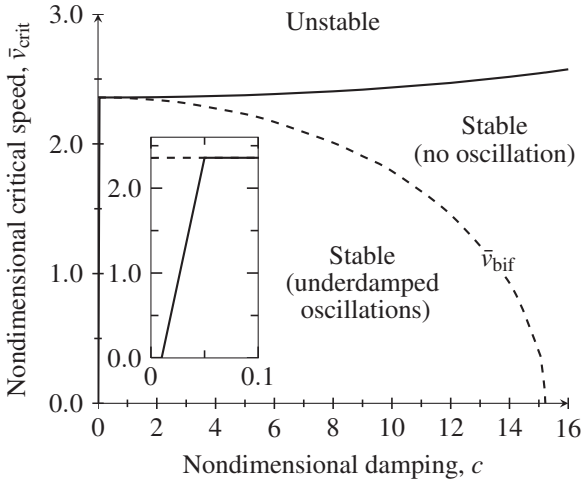

Figure 9.6: *Stability curve (—) obtained by plotting nondimensional critical speed $\bar{v}_{crit}$ as a function of nondimensional damping c for vertically traveling Rayleigh beam, while its bifurcation speed (- - -) vanishes monotonically with increase in c, thus, marking a boundary within the sub-critical (stable) region inside which the cable undergoes underdamped oscillations. The inset shows the steep initial rise in the stability curve due to the inclusion of damping. The other parameters $\rho = 10$, $S_R = 20$ and $\mu = 1$.*

critical speed $\bar{v}_{crit}$ is 1, matching the analytic solution in [Hagedorn & DasGupta, 2007]. Also, it is important to note that in contrast to beams (Fig. 9.2), the stability curve of vertically traveling string in Fig. 9.7 is concave and it converges to the critical speed of a horizontally traveling string

at high end-tensions.

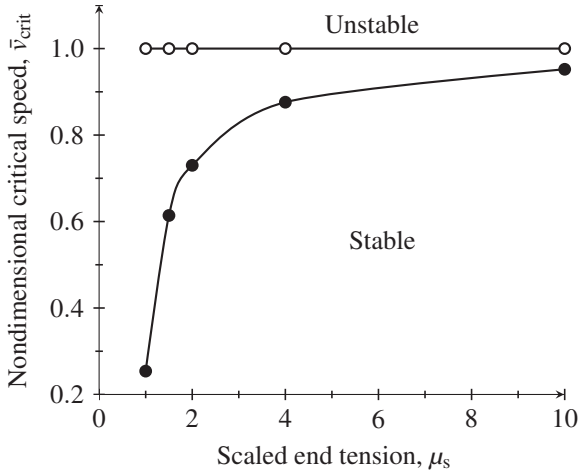

Figure 9.7: *Nondimensional critical speed $\bar{v}_{crit}$ as a function of scaled end tension μ_s for horizontally (—○—) and vertically (—●—) traveling strings. The parameter $\rho = 0$ and 10 for the horizontally and vertically traveling strings, respectively, while the paramater $c = 0$.*

9.3 Alternative nondimensionalization scheme

An alternative nondimensionalization of governing equation (8.1.1), as suggested by an anonymous reviewer of our paper [Dehadrai et al., 2018], is given here employing the following dimensionless quantities:

$$\begin{gathered}\bar{x} = \frac{x}{L},\ \bar{y} = \frac{y}{L},\ \bar{t} = t\sqrt{\frac{T(L)}{L^2\rho_0 A_c}},\\ \bar{v} = v\sqrt{\frac{\rho_0 A_c}{T(L)}},\ \theta = \frac{EI}{L^2 T(L)},\\ \rho = \frac{wL}{T(L)},\ \mathsf{S_R} = \sqrt{\frac{I}{L^2 A_c}} \text{ and } c = \frac{\zeta L}{\sqrt{\rho_0 A_c T(L)}},\end{gathered} \tag{9.3.1}$$

where the slenderness ratio $\mathsf{S_R}$ is reciprocal of the quantity defined in (8.3.1), while the dimensionless bending rigidity θ is the ratio of bending rigidity and the end tension. With these (8.1.1) becomes

$$\left[\theta\,\bar{\partial}_x^4 - \bar{\partial}_x\left\{\bar{T}(\bar{x})\,\bar{\partial}_x\right\}\right]\bar{y} + c\,\dot{\bar{y}} + \left(1 - \mathsf{S}_\mathsf{R}^2\,\bar{\partial}_x^2\right)\ddot{\bar{y}} = 0 \tag{9.3.2a}$$

and

$$\bar{y}(0,\bar{t}) = \bar{y}(1,\bar{t}) = \bar{\partial}_x^2\bar{y}\,(0,\bar{t}) = \bar{\partial}_x^2\bar{y}\,(1,\bar{t}) = 0, \tag{9.3.2b}$$

while the nondimensional tension

$$\bar{T}(\bar{x}) = \frac{T(x)}{T(L)} = 1 - \rho\,(1-\bar{x})\,. \tag{9.3.3}$$

The nondimensional equation of the string is obtained from (9.3.2) by setting $\theta = 0$ and $S_R = 0$,

$$\left[-\bar{\partial}_x \left\{\bar{T}(\bar{x})\, \bar{\partial}_x\right\}\right] \bar{y} + c\,\dot{\bar{y}} + \ddot{\bar{y}} = 0, \tag{9.3.4a}$$

and

$$\bar{y}(0,\bar{t}) = \bar{y}(1,\bar{t}) = 0. \tag{9.3.4b}$$

In this scheme, the dimensionless bending rigidity θ is employed as the control parameter in contrast to dimensionless end tension μ in Sec.8.3. The stability curves for the horizontally and the vertically traveling beams for varying θ are shown in Fig. 9.8. We observe that as we increase

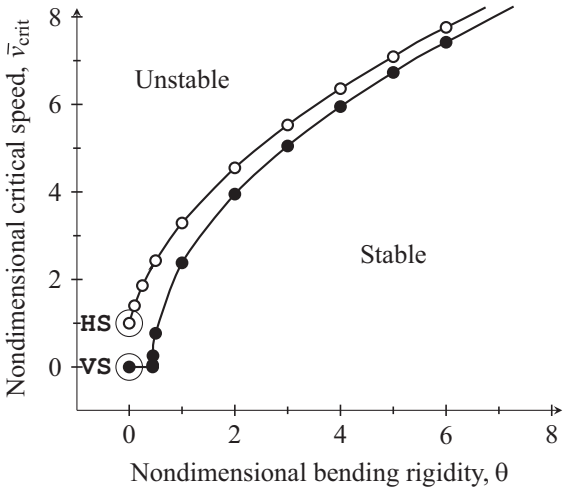

Figure 9.8: *Stability curves for Euler-Bernoulli beams traveling horizontally (–○–) and vertically (–●–) are obtained by plotting the nondimensional critical speed $\bar{v}_{crit}$ as a function of nondimensional bending rigidity θ. The parameter $\rho = 0$ and 10 for the horizontally and vertically traveling beams, respectively, while the other parameters $c = 0$ and $S_R = 0$. At $\theta = 0$, the critical points* HS *($\bar{v}_{crit} = 1$) and* VS *($\bar{v}_{crit} = 0$) are the critical speeds of horizontally and vertically traveling strings, respectively.*

the bending rigidity the traveling cable becomes more stable. Also, the cable is more stable while traveling horizontally than traveling vertically due to the effect of gravity. However, with further increase in θ the stability curves of the vertically and the horizontally traveling cables come closer, and the stabilizing effect of bending rigidity dominates the destabilizing effect of gravity.

The critical speeds HS ($\bar{v} = 1$) and VS ($\bar{v} = 0$) at zero bending rigidity ($\theta = 0$) correspond to the horizontally and the vertically traveling strings, respectively. Note that, for the string we obtain only one point through this scheme in Fig. 9.8, in contrast to a complete stability curve in Fig. 9.7.

9.4 Convergence of solution

The converged values of critical speed for horizontally and vertically traveling beams are found by progressively increasing the number N of sine functions until the relative error between

two successive computations becomes lower than 0.001%. For the horizontally traveling cable, the computed values of critical speed from beam and string models are compared with those obtained by employing Green's functions in [Wickert & Mote, 1990]. Additionally, we solved (9.0.2) numerically utilizing 2-node Hermitian finite elements (FE). The converged solution from this procedure is in excellent agreement with that found through Galerkin projection with sine modes. Figure 9.9(a) plots the relative error

$$\varepsilon^{v}_{\text{crit}} = \left| 1 - \frac{\bar{v}^{N}_{\text{crit}}}{\bar{v}^{\text{ref}}_{\text{crit}}} \right| \cdot 100$$

in calculating the critical speed $\bar{v}^{N}_{\text{crit}}$ for an Euler-Bernoulli beam using N number of modes (Galerkin) or elements (FE), where we consider the reference critical speed $v^{\text{ref}}_{\text{crit}} = 10.48$, which is the closed form result by Wickert & Mote [1990] for the horizontally traveling cable, while $\bar{v}^{\text{ref}}_{\text{crit}} = \bar{v}^{(N=399)}_{\text{crit}} = 10.23$ for the vertically traveling cable. Similarly, Fig. 9.9(b) plots the relative error

$$\varepsilon^{\omega}_{\text{sub}} = \left| 1 - \frac{\omega^{N}}{\omega^{\text{ref}}} \right| \cdot 100$$

in calculation of the first mode's eigenvalue ω^{N} using N number of modes (Galerkin) or elements (FE) at an arbitrarily chosen sub-critical speed $\bar{v}^{\text{ref}}_{\text{sub}} = 5$, where the reference eigenvalue ω^{ref} is calculated at $N = 399$. For horizontally traveling beams the closed form results of Wickert & Mote [1990] are taken as reference. We conclude that when $N \geq 9$ both FE solution and Galerkin projection with sine modes are accurate, and match with each other.

9.5 Energetics

Further insight into the system is provided by investigating the manner in which energy flows into and away from a traveling cable. In this section we examine the flow of energy in traveling Euler-Bernoulli beams below and above the critical speed.

The total mechanical energy per unit length of the beam

$$\bar{E}(\bar{x}, \bar{t}) = \bar{E}_K(\bar{x}, \bar{t}) + \bar{E}_P(\bar{x}, \bar{t}),$$

where the kinetic energy density

$$\bar{E}_K(\bar{x}, \bar{t}) = \frac{1}{2}(\bar{v}^2 + \dot{\bar{y}}^2)$$

and the potential energy density

$$\bar{E}_P(\bar{x}, \bar{t}) = \frac{1}{2}(\bar{\partial_x}^2 \bar{y})^2 + \frac{\bar{T}(\bar{x})}{2}(\bar{\partial_x} \bar{y})^2 + \rho \bar{x}.$$

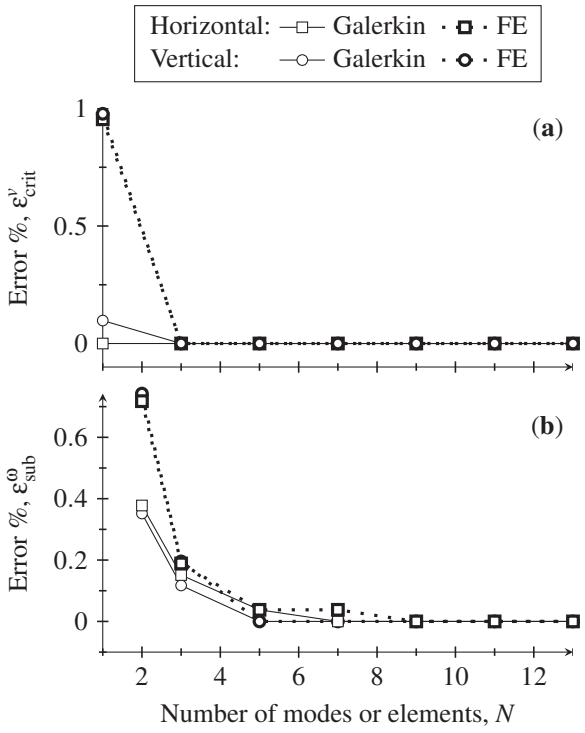

Figure 9.9: *Plot (**a**) compares the errors in critical speed v^N_{crit} obtained from the N-term Galerkin projection and the N-element FE solution for horizontally ($\rho = 0$) and vertically ($\rho = 10$) traveling cables. In each case $\mu = 10$, $c = 0$ and $S_R^{-2} = 0$. For horizontally traveling cable the critical speed $v^{ref}_{crit} = 10.48$, as found by Wickert & Mote [1990]. For vertically traveling cable, the critical velocity calculated using $N = 399$ terms is taken as the reference. Plot (**b**) compares errors in the calculation of the first mode's eigenvalue ω at sub-critical speed $v^{ref}_{sub} = 5$.*

The total rate of change of mechanical energy is

$$\begin{aligned}\dot{\bar{E}}(\bar{t}) &= \int_0^1 \left(\bar{\partial}_{\bar{t}}\bar{E} + \bar{v}\,\bar{\partial}_{\bar{x}}\bar{E}\right) d\bar{x} \\ &= \left| \left\{\bar{T}(\bar{x})\,\bar{\partial}_{\bar{x}}\bar{y} - \bar{\partial}^3_{\bar{x}}\bar{y}\right\}\left(\bar{v}\,\bar{\partial}_{\bar{x}}\bar{y}\right) \right|_0^1 + \int_0^1 \rho\bar{v}\left(\bar{\partial}_{\bar{x}}\bar{y}\right)^2 d\bar{x}, \end{aligned} \tag{9.5.1}$$

where $\bar{\partial}_{\bar{x}}\bar{y}$ is the slope of the cable at $\bar{x}$, and so $\bar{T}(\bar{x})\,\bar{\partial}_{\bar{x}}\bar{y}$ and $\bar{v}\,\bar{\partial}_{\bar{x}}\bar{y}$ are the transverse ($\bar{y}$-directional) component of the nondimensional tension and the convective velocity, respectively, while $\bar{\partial}^3_{\bar{x}}\bar{y}$ is the dimensionless shear force in the cable at $\bar{x}$. Therefore, the first term in (9.5.1), which is evaluated at the ends ($\bar{x} = 0$ and 1), is the power supplied to the cable across the end supports by the action of the transverse component of tension and the shear force. This term estimates the inflow and outflow of energy from the boundaries due to the presence of non-zero convective velocity $\bar{v}\,\bar{\partial}_{\bar{x}}\bar{y}$ there; note that the local velocity $\bar{\partial}_{\bar{t}}\bar{y}$ vanishes at the supports. The second term in (9.5.1) is the contribution of the cable's self-weight, as it travels vertically against gravity, and which vanishes ($\rho = 0$) for a horizontally traveling cable.

The time rate of change of energy, (9.5.1), is zero in a non-traveling ($\bar{v} = 0$) cable, but not if the cable is traveling. In this the traveling cable exhibits a *non-conservative* behaviour. This behaviour, however, doesn't necessarily indicate instability of the traveling cable. Indeed, through modal analysis (Sec. 9.1) we identified a range of travel speeds and other system parameters for stable operations. Therefore, in the following, we study the stability of horizontally and vertically traveling cable by monitoring the evolution of the total mechanical energy and the transverse displacement of a material particle passing through the mid-span ($x = L/2$ or $\bar{x} = 0.5$) of the cable.

Transverse displacement and the rate of change of energy

A standard explicit (Runge-Kutta) numerical time-integration of the state space equation (9.0.2) is performed to obtain the temporal coefficients $\mathbf{b}(t)$. The traveling cable is assumed to be released from a displaced configuration corresponding to the first sine mode. Accordingly, the initial conditions are: $\mathbf{b}(0) = [0.01, 0, 0, \dots]^{\mathsf{T}}$ and $\dot{\mathbf{b}}(0) = [0, 0, 0, \dots]^{\mathsf{T}}$. The transverse displacement at $\bar{x} = 0.5$ is then calculated from (9.0.1), and the rate of change of total energy $\dot{\bar{E}}$ is obtained from (9.5.1).

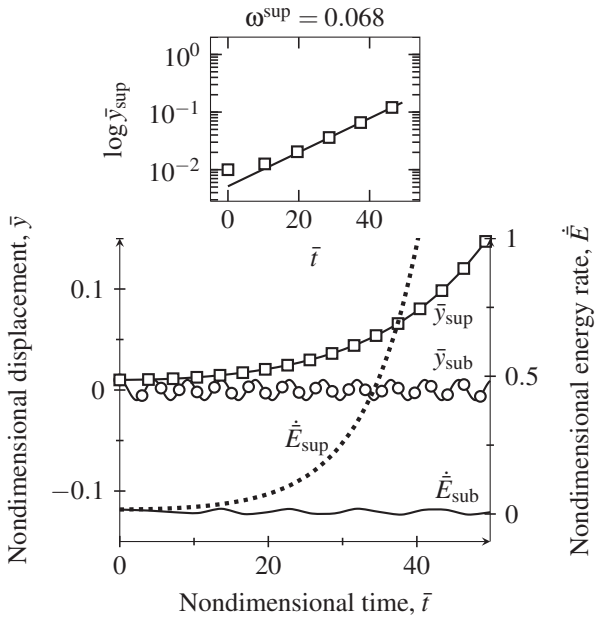

Figure 9.10: *Temporal evolution of the transverse nondimensional displacement of the horizontally traveling cable at $\bar{x} = 0.5$ ($x = L/2$) and the rate of change of total mechanical energy (nondimensional). The sub-critical and super-critical nondimensional speeds are $\bar{v}_{sub} = 3.26$ and $\bar{v}_{sup} = 3.297$, respectively, while the parameters $\rho = 0$, $\mu = 1$, $c = 0$ and $S_R^{-2} = 0$. The inset semi-log plot shows that $\bar{y}_{sup}$ (□) grows modestly for some time following which the growth is exponential (—) at a rate $\exp(\omega^{sup}\bar{t}) = \exp\{Re(\omega^{sup})\,\bar{t}\}$, with $\omega^{sup} = 0.068$.*

Figures 9.10 and 9.11 show the evolution of transverse displacement and $\dot{\bar{E}}$ for a horizontally and vertically traveling Euler-Bernoulli beam, respectively. The results at sub-critical ($\bar{v} < \bar{v}_{\text{crit}}$) and super-critical ($\bar{v} > \bar{v}_{\text{crit}}$) operations are compared, keeping the critical speed corresponding to $\mu = 1$ and $\rho = 10$ from Fig. 9.2 as reference. The displacement $\bar{y}_{\text{sub}}$ and rate of change of energy $\dot{\bar{E}}_{\text{sub}}$ correspond to operation at a sub-critical speed $\bar{v}_{\text{sub}} < \bar{v}_{\text{crit}}$, while $\bar{y}_{\text{sup}}$ and $\dot{\bar{E}}_{\text{sup}}$ are calculated at a super-critical speed $\bar{v}_{\text{sup}} > \bar{v}_{\text{crit}}$.

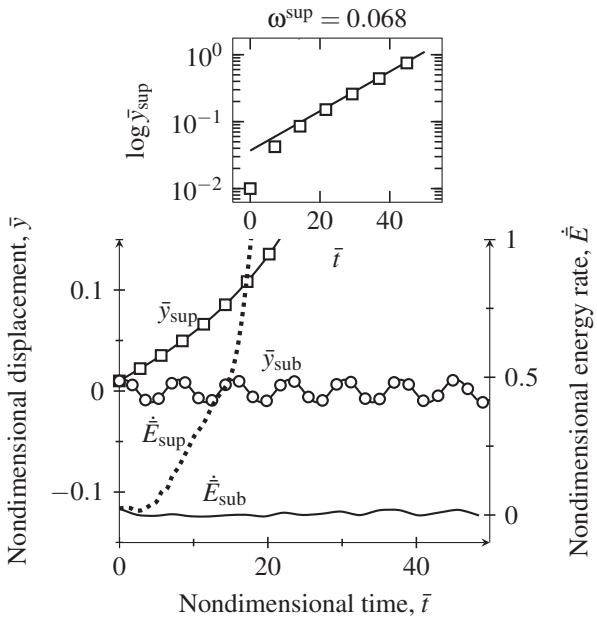

Figure 9.11: *Temporal evolution of the transverse nondimensional displacement of the vertically traveling cable at $\bar{x} = 0.5$ ($x = L/2$) and the rate of change of total mechanical energy (nondimensional). The sub-critical and super-critical nondimensional speeds are $\bar{v}_{sub} = 2.37$ and $\bar{v}_{sup} = 2.38723$, respectively, while the parameters $\rho = 10$, $\mu = 1$, $c = 0$ and $S_R^{-2} = 0$. The inset semi-log plot shows that $\bar{y}_{sup}$ ($\square$) grows exponentially, at a rate $\exp(\omega^{sup}\bar{t}) = \exp\{Re(\omega^{sup})\,\bar{t}\}$ with $\omega^{sup} = 0.068$, after a rapid initial rise in its amplitude.*

The sub-critical $\dot{\bar{E}}_{\text{sub}}$ and $\bar{y}_{\text{sub}}$ are oscillatory and bounded over an extended period of time (see Fig. 9.10). This is in agreement with Fig. 9.1, in which, at speeds lower than critical speed the real part of the first eigenvalue is zero. However, at super-critical speed $\bar{v}_{\text{sup}}$, both the energy rate and displacement amplitude show rapid growth. At this speed, as shown in Fig. 9.1, $\text{Re}(\omega^{\text{sup}})$ is positive and $\text{Im}(\omega^{\text{sup}})$ vanishes, so that the displacement $\bar{y}_{\text{sup}}$ grows exponentially with time at the rate $\omega^{\text{sup}} = \text{Re}(\omega^{\text{sup}}) = 0.068$, as shown in the inset of Fig. 9.10. We note that the growth is linear and small for a while before growing exponentially. With further increase in speed this exponent becomes larger and the growth in amplitude is even faster.

Traveling against gravity, as discussed previously, only worsens the stability, as shown in Fig. 9.11. Indeed, we observe from the inset in Fig. 9.11 that, in contrast to the inset of Fig. 9.10,

during vertical travel the initial growth in displacement $\bar{y}_{\text{sup}}$ for super-critical speed is fairly rapid before it settles into exponential growth at the same rate as in Fig. 9.10. Furthermore, this growth appears earlier in time as compared to the horizontally traveling cable. Thus, the exponential growth of $\dot{\bar{E}}$ in energetics and $\bar{y}_{\text{sup}}$ transient analysis support the existence of positive Re(ω) found from modal analysis. However, the initial growth in $\bar{y}_{\text{sup}}$, discussed above, is probably due to the choice of initial conditions, $\mathbf{b}(0)$ and $\dot{\mathbf{b}}(0)$, used during the numerical integration of the state space equation. This dependence on initial conditions makes the transient and energy analyses insufficient in determining the instability, in contrast to the modal analysis.

The super-critical energy rate $\dot{\bar{E}}_{\text{sup}}$ grows monotonically for a horizontally traveling cable (Fig. 9.10), whereas the growth has an initial dip in case of vertically traveling cable (Fig. 9.11). We surmise that this dip is due to the second term in (9.5.1), which is a contribution of the cable's weight to cable tension that is absent during horizontal travel.

Chapter **10**

Conclusions and future work

In this part of the thesis, we studied the vibration analysis of a tensioned, heavy cable traveling vertically, against gravity, at a constant speed. The cable was modeled as a beam incorporating rotary inertia. Employing both the Galerkin method with sine modes and the finite element method, a modal analysis was performed for a beam with (Rayleigh) and without rotary inertia (Euler-Bernoulli). The instability in the modal analysis was identified with the critical value of the parameter at which the real part of the first mode's eigenvalue first becomes positive. We computed the critical values of the parameters at which instability occurs; namely speed of travel, end-tension, slenderness ratio, and bending rigidity. Stability curves, or boundaries, are obtained in the space of these parameters. Direct numerical integration and energy analysis on the Euler-Bernoulli model are used to verify these boundaries. As a particular case, highly flexible cables with zero bending rigidity are also studied by modeling them as strings.

The major findings in our study are as follows:

(1) For the Euler-Bernoulli beam, the critical speed $\bar{v}_{\text{crit}}$ coincides with the speed $\bar{v}_{\text{bif}}$ corresponding to the bifurcation of the real part of eigenvalue and simultaneous vanishing of the associated imaginary part. In contrast, $\bar{v}_{\text{crit}}$ and $\bar{v}_{\text{bif}}$ are different for a vertically traveling Rayleigh beam.

(2) The applied end-tension enhances the stability of a traveling cable system, while the action of a component of gravity along the vertical cable lowers it. This observation is regardless of whether the traveling cable is modeled as a beam or as a string.

(3) Slenderness ratio improves the stability of the system. However, the sensitivity of the response to slenderness ratio is more clearly observed when a traveling cable is modeled as a Rayleigh beam rather than as an Euler-Bernoulli beam. When slenderness ratios are high, both the models give close results.

(4) A vertically traveling Rayleigh beam shows instability for all travel speeds, i.e. $\bar{v}_{\text{crit}} = 0$ and $\bar{v}_{\text{bif}} > \bar{v}_{\text{crit}}$. However, this inherent instability can be removed by inclusion of damping. When damping is included, $\bar{v}_{\text{bif}} < \bar{v}_{\text{crit}}$ and the Rayleigh beam undergoes underdamped oscillations at sub-bifurcation travel speeds. In Euler-Bernoulli beams the damping further enhances the stability.

(5) The time rate of change of energy $\dot{\bar{E}}$ of the traveling cable is not constant, exhibiting a non-conservative behaviour. This behaviour does not necessarily imply instability at all speeds of travel. At sub-critical speeds, $\dot{\bar{E}}_{\text{sub}}$ is oscillatory, but remains bounded for extended period of time. Whereas, at super-critical speeds $\dot{\bar{E}}_{\text{sup}}$ grows monotonically for horizontally traveling cables and non-monotonically for vertically traveling cables. Both $\dot{\bar{E}}_{\text{sup}}$ and $\bar{y}_{\text{sup}}$ grow more rapidly when cable travels vertically, thereby confirming the destabilizing effect caused by traveling against gravity. However, the results of the transient and energy analyses are dependent on the choice of initial conditions, in contrast to those of the modal analysis.

We conclude that pre-tension, bending rigidity, damping, and slenderness ratio enhance the stability of traveling cables. However, traveling vertically against gravity adversely affects stability, and this has significant design implications. Finally, by sufficiently increasing the pre-tension we can minimize the destabilizing effect of gravity. For an already operating system of a vertically traveling cable, the most practical way to enhance the stability is by tuning the end-tension offered by the mechanism (motor) that drives the cable. With the parametric analysis presented here, we may avoid unstable operating situations in the first place by making an informed choice of the material and cross-sectional features of the cable, and by utilizing the damping offered by the surrounding fluid, if any.

Future research

For the vertically traveling cables, the cable oscillations about the equilibrium (vertical axis) could be considered small up to the leading order. The present study focused on determining the critical values of system parameters at the onset of instability.

However, after the onset of instability, or when external loads are large, nonlinearities may set in due to large displacements. Also, when cables travel inclined to gravity, the equilibrium shape of the cable has to be considered when investigating vibrations of such cables. Indeed, in light of the geometrically exact (GE) beam theory discussed in Problem A, which incorporates large deflections and rotations, there is a scope of performing the stability analysis about a three-

dimensionally deformed state. The GE beam model will allow us to investigate the contribution of bending, torsion, stretching and shear in the stability of traveling cables. This study of flexible cables that are generally not restricted to operate in a 2D plane will be more realistic.

Furthermore, with the growing attention towards cable-ways as a mode of transport in hilly regions, similar stability analyses can be done by augmenting the present cable model with intermediate hanging rigid bodies, and then extend it to the nonlinear regime. Such a study may give interesting insights into designing these engineering applications.

Finally, problems related to lengthening cables in above applications is another exciting avenue where the research presented in Problem A and Problem B of the thesis have a shared scope of future research, as mentioned in Chap.6. The 2D model for longitudinally extending GE beams was developed by Vu-Quoc & Li [1995]. Its application to the aerostat deployment problem in two-dimensional linear [Mukherjee et al., 2018] and nonlinear [Mukherjee, 2016] regimes, and extension to three dimensions [Singh, 2018] has recently received attention, but there remains much scope for further work.

References

Abramowitz, M., Stegun, I. A., et al. (1964). *Handbook of mathematical functions: with formulas, graphs, and mathematical tables*, volume 55. Dover publications New York. See also http://people.math.sfu.ca/~cbm/aands/frameindex.htm. 5.2.3

Antman, S. (2013). *Nonlinear Problems of Elasticity*. Applied Mathematical Sciences. Springer New York. 1.3, 2

Banichuk, N., Jeronen, J., Neittaanmäki, P., Saksa, T., & Tuovinen, T. (2013). *Mechanics of Moving Materials*. Solid Mechanics and Its Applications. Springer International Publishing. 7

Barakat, R. (1968). Transverse vibrations of a moving thin rod. *J. Acoust. Soc. Am.*, *43*(3), 533–539. 7

Bathe, K. J. (2006). *Finite Element Procedures*. Prentice Hall. 1.3, 4, 4.6, 4.6.1, 9

Beatty, M. (2013). *Principles of Engineering Mechanics: Kinematics — The Geometry of Motion*. Mathematical Concepts and Methods in Science and Engineering. Springer US. 2.b.2

Betsch, P. & Steinmann, P. (2002). Frame-indifferent beam finite elements based upon the geometrically exact beam theory. *Int. J. Numer. Meth. Eng.*, *54*(12), 1775–1788. 2

Bisgaard, M., Bendtsen, J. D., & Cour-Harbo, A. L. (2009). Modeling of generic slung load system. *J. Guid. Control Dynam.*, *32*(2), 573–585. 1.1, 1.6

Budynas, R., Young, W., & Sadegh, A. (2011). *Roark's Formulas for Stress and Strain*, volume 8. McGraw-Hill Education. 2.4

Cicolani, L. S. & Kanning, G. (1992). Equations of motion of slung-load systems, including multilift systems. Technical report, NASA Ames Research. 1.1

Cox, R. (1996). Axisymmetric translation of a slender torus along a circular tube. *Chem. Eng. Commun.*, *148*(1), 565–592. 3

Dehadrai, A. R., Sharma, I., & Gupta, S. S. (2018). Stability of vertically traveling, pre-tensioned, heavy cables. *J. Comput. Nonlin. Dyn.*, *13*(8), 081003–081003–9. 7, 9.3

Den Hartog, J. (2013). *Mechanical Vibrations*. Dover Civil and Mechanical Engineering. Dover Publications. 2.6.2

Etkin, B. (1998). Stability of a towed body. *J. Aircraft*, *35*(2), 197–205. 1.1, 1.4

Farokhi, H., Ghayesh, M., & Amabili, M. (2013a). In-plane and out-of-plane nonlinear dynamics of an axially moving beam. *Chaos Soliton Fract.*, *54*, 101–121. 7

Farokhi, H., Ghayesh, M., & Amabili, M. (2013b). Nonlinear dynamics of a geometrically imperfect microbeam based on the modified couple stress theory. *Int. J. Eng. Sci.*, *68*, 11–23. 7

Farokhi, H., Ghayesh, M. H., & Hussain, S. (2016). Three-dimensional nonlinear global dynamics of axially moving viscoelastic beams. *J. Vib. Acoust.*, *138*(1), 011007. 7

Feaster, L., Poli, C., & Kirchhoff, R. (1977). Dynamics of a slung load. *J. Aircraft*, *14*(2), 115–121. 1.1, 1.3

Ghayesh, M., Amabili, M., & Farokhi, H. (2013a). Three-dimensional nonlinear size-dependent behaviour of timoshenko microbeams. *Int. J. Eng. Sci.*, *71*, 1–14. 7

Ghayesh, M., Amabili, M., & Farokhi, H. (2013b). Two-dimensional nonlinear dynamics of an axially moving viscoelastic beam with time-dependent axial speed. *Chaos Soliton Fract.*, *52*, 8–29. 7

Ghayesh, M. & Farokhi, H. (2015). Thermo-mechanical dynamics of three-dimensional axially moving beams. *Nonlinear Dynam.*, *80*(3), 1643–1660. 7

Ghayesh, M., Farokhi, H., & Amabili, M. (2013). Nonlinear dynamics of a microscale beam based on the modified couple stress theory. *Compos. Part B-Eng.*, *50*, 318–324. 7

Glauert, H. (1930). The stability of a body towed by a light wire. *ARC R&M*, *1312*. 1.1, 1.2, 1.3, 5.1.5

Glauert, H. (1934). Heavy flexible cable for towing a heavy body below an aeroplane. *ARC R&M*, *1592*. 1.1

Greenwood, D. (1988). *Principles of Dynamics*. Prentice-Hall International. 1.3, 3

Hagedorn, P. & DasGupta, A. (2007). *Vibrations and Waves in Continuous Mechanical Systems*. Wiley. 7, 8.1, 8.2, 8.3, 9.2

Hall, B. (2015). *Lie groups, Lie algebras, and representations: an elementary introduction*, volume 222. Springer. 2.b

Hilber, H. M., Hughes, T. J., & Taylor, R. L. (1977). Improved numerical dissipation for time integration algorithms in structural dynamics. *Earthq. Eng. Struct. D.*, *5*(3), 283–292. 4.6.1

Hoerner, S. F. (1992). Fluid dynamic drag. 1965. *Bricktown, NJ: Published by the author*. 1.1, 1.3, 2.6.2, 2.6.2, 3

Ibrahimbegović, A. (1995). On finite element implementation of geometrically nonlinear reissner's beam theory: three-dimensional curved beam elements. *Comput. Method Appl. M.*, *122*(1-2), 11–26. 1.3, 2, 2.4, 4

Ibrahimbegović, A. & Mikdad, M. A. (1998). Finite rotations in dynamics of beams and implicit time-stepping schemes. *Int. J. Numer. Meth. Eng.*, *41*(5), 781–814. 1.3

Lahiri, S., Chattopadhyay, J., & Bhattacharya, S. (2012). Design methodology for under-slung store structure of air-borne time domain electromagnetic (tdem) system. *Aerosp. Sci. Technol.*, *23*(1), 120–131. 1.2, 1.7, 5.3, 1

Mäkinen, J. (2008). Rotation manifold so (3) and its tangential vectors. *Comput. Mech.*, *42*(6), 907. 4.6.1

McLeod, A. (1918). Action of wind on flexible cables, with applications to cables towed below aeroplanes and balloon cables. *ARC R&M*, *554 (10)*. 1.1

Meier, C., Popp, A., & Wall, W. A. (2017). Geometrically exact finite element formulations for slender beams: Kirchhoff–love theory versus simo–reissner theory. *Arch. Comput. Method E.*, 1–81. 2

Meirovitch, L. & Hagedorn, P. (1994). A new approach to the modelling of distributed non-self-adjoint systems. *J. Sound Vib.*, *178*(2), 227–241. 9

Miranker, W. L. (1960). The wave equation in a medium in motion. *IBM J. Res. Dev.*, *4*(1), 36–42. 7

Mockensturm, E. M. & Guo, J. (2005). Nonlinear vibration of parametrically excited, viscoelastic, axially moving strings. *J. Appl. Mech.*, *72*(3), 374–380. 7

Mote, C. D. (1965). A study of band saw vibrations. *J. Frankl. Inst.*, *279*(6), 430–444. 7

Mote, C. D. (1966). On the nonlinear oscillation of an axially moving string. *J. Appl. Mech.*, *33*(2), 463–464. 7

Mukherjee, D. (2016). Dynamics and stability of axially lengthening and shortening heavy cables with end mass. Mtech thesis, IIT Kanpur, India. 6.1, 10

Mukherjee, D., Sharma, I., & Gupta, S. S. (in press 2018). Dynamics and stability of variable-length, vertically traveling cables, with application to tethered aerostats. *J. Aircraft*. 10

Newmark, N. M. (1959). A method of computation for structural dynamics. *J. Eng. Mech. Div. - ASCE*, *85*(3), 67–94; See also http://opensees.berkeley.edu/wiki/index.php/Newmark_Method. 4.6.1

Öz, H., Pakdemirli, M., & Boyacı, H. (2001). Non-linear vibrations and stability of an axially moving beam with time-dependent velocity. *Int. J. Nonlin. Mech.*, *36*(1), 107–115. 7

Païdoussis, M. P., Price, S. J., & De Langre, E. (2010). *Fluid-structure interactions: cross-flow-induced instabilities*. Cambridge University Press. 1.3, 2.6.2, 3

Pakdemirli, M. & Ulsoy, A. (1997). Stability analysis of an axially accelerating string. *J. Sound Vib.*, *203*(5), 815–832. 7

Poll, C. & Cromack, D. (1973). Dynamics of slung bodies using a single-point suspension system. *J. Aircraft*, *10*(2), 80–86. 1.1, 1.3

Reissner, E. (1981). On finite deformations of space-curved beams. *Z. Angew. Math. Phys. - ZAMP*, *32*(6), 734–744. 2

Rogge, T. R. (1972). Equations of motion for flexible cables. *J. Aircraft*, *9*(11), 799–800. 7

Sack, R. A. (1954). Transverse oscillations in travelling strings. *Brit. J. Appl. Phys.*, *5*(6), 224. 7

Shabana, A. A. (1997). Flexible multibody dynamics: review of past and recent developments. *Multibody Syst. Dyn.*, *1*(2), 189–222. 2

Simo, J. & Vu-Quoc, L. (1986a). On the dynamics of flexible beams under large overall motions—the plane case: Part ii. *J. Appl. Mech.*, *53*(4), 855–863. 2.b, 5.1.2, 5.2, 5.1.3

Simo, J. C. (1985). A finite strain beam formulation. the three-dimensional dynamic problem. part i. *Comput. Method Appl. M.*, *49*(1), 55–70. 2, 2.4

Simo, J. C. & Vu-Quoc, L. (1986b). A three-dimensional finite-strain rod model. part ii: Computational aspects. *Comput. Method Appl. M.*, *58*(1), 79–116. 1.3, 2, 2.4, 4, 4.6.1, 5.1.1

Simo, J. C. & Vu-Quoc, L. (1988). On the dynamics in space of rods undergoing large motions—a geometrically exact approach. *Comput. Method Appl. M.*, *66*(2), 125–161. 1.3, 2, 2.4, 4.6.1, 5.1.4

Singh, N. (2018). Dynamics of axially shortening and lengthening geometrically exact beams in 3-dimensions. Mtech thesis, IIT Kanpur, India. 10

Spencer, A. (2012). *Continuum Mechanics*. Dover Books on Physics. Dover Publications. 2.b.2

Stuckey, R. A. (2001). Mathematical modelling of helicopter slung-load systems. Technical report, Air Operations Division Aeronautical and Maritime Research Laboratory, DSTO Victoria, Australia. 1.5, 1.1, 1.1

Swope, R. D. & Ames, W. F. (1963). Vibrations of a moving threadline. *J. Frankl. Inst.*, *275*(1), 36–55. 7

Thaokar, R. M., Schiessel, H., & Kulic, I. M. (2007). Hydrodynamics of a rotating torus. *Eur. Phys. J. B.*, *60*(3), 325–336. 3

Thurman, A. L. & Mote, C. D. (1969). Free, periodic, nonlinear oscillation of an axially moving strip. *J. Appl. Mech.*, *36*(1), 83–91. 7

Timoshenko, S. P. & Gere, J. M. (2009). *Theory of Elastic Stability* (2 ed.). Dover Publications. 8.1, 8.3

Udwadia, F. E. & Kalaba, R. E. (1992). A new perspective on constrained motion. *Proc. R. Soc. Lond. A.*, *439*(1906), 407–410. 1.1

Venkatesan, C. (2014). *Fundamentals of helicopter dynamics*. CRC Press. 5.3

Vu-Quoc, L. & Li, S. (1995). Dynamics of sliding geometrically-exact beams: large angle maneuver and parametric resonance. *Comput. Method Appl. M.*, *120*(1-2), 65–118. 10

Wickert, J. A. (1992). Non-linear vibration of a traveling tensioned beam. *Int. J. Nonlin. Mech.*, *27*(3), 503–517. 7

Wickert, J. A. & Mote, C. D. (1990). Classical vibration analysis of axially moving continua. *J. Appl. Mech.*, *57*(3), 738–744. 7, 9.2, 9.4, 9.9

Wickert, J. A. & Mote Jr, C. D. (1989). On the energetics of axially moving continua. *J. Acoust. Soc. Am.*, *85*(3), 1365–1368. 7

Ziegler, H. (2013). *Principles of structural stability*, volume 35. Birkhäuser. 7